

**PROCESSING AND ANALYSIS OF SEISMIC REFLECTION AND TRANSIENT  
ELECTROMAGNETIC DATA FOR KIMBERLITE EXPLORATION IN THE  
MACKENZIE VALLEY, NT**

by

David Anton Moore

B.A.Sc., The University of British Columbia, 2005

A THESIS SUBMITTED IN PARTIAL FULFILLMENT OF  
THE REQUIREMENTS FOR THE DEGREE OF

MASTER OF APPLIED SCIENCE

in

THE FACULTY OF GRADUATE STUDIES  
(Geophysics)

THE UNIVERSITY OF BRITISH COLUMBIA  
(Vancouver)

February 2009

© David Anton Moore, 2009

## Abstract

The Lena West property near Lac des Bois, NT, held by Diamondex Resources Ltd., is an area of interest for exploration for kimberlitic features. In 2005, Frontier Geosciences Inc. was contracted to carry out seismic reflection and time-domain transient electromagnetic (TEM) surveys to investigate the possibility of kimberlite pipes being the cause of total magnetic intensity (TMI) anomalies previously identified on the property. One small part of the property, Area 1915, was surveyed with two perpendicular seismic reflection lines 1550 m and 1790 m long and three TEM lines consisting of six or seven individual soundings each with a 200 m transmitter loop. The results generated by Frontier Geosciences did not indicate any obvious vertical features that correlated with the TMI anomaly.

The purpose of this study is to reprocess the seismic reflection data using different approaches than those of Frontier Geosciences and to invert the TEM data using a 1-D inversion code, EM1DTM recently developed by the UBC Geophysical Inversion Facility, to improve upon previous results and enhance the interpretation. A secondary objective is to test the robustness of EM1DTM when applied to observed TEM data, since prior to this study it had only been applied to synthetic data. Selective bandpass filtering, refraction and residual statics and  $f$ - $x$  deconvolution procedures contributed to improved seismic images to the recorded two-way traveltime of 511.5 ms (approximately 1100 m depth). The TEM data were successfully inverted and converted to pseudo 2-D recovered resistivity sections that showed similar results to those from Frontier Geosciences. On the final seismic reflection sections, several strong reflectors are identified and the base of the overlying sedimentary layers is interpreted at a depth of  $\sim$ 600 m. The TEM results show consistent vertical structure with minimum horizontal variation across all lines to a valid depth of  $\sim$ 150 m. However, neither TEM nor seismic reflection results

provide any information that correlates well with the observed TMI anomaly.

## Table of Contents

<b>Abstract</b> . . . . .	ii
<b>Table of Contents</b> . . . . .	iv
<b>List of Tables</b> . . . . .	vii
<b>List of Figures</b> . . . . .	viii
<b>Acknowledgements</b> . . . . .	x
<b>Dedication</b> . . . . .	xi
<b>1 INTRODUCTION</b> . . . . .	1
1.1 Objectives . . . . .	7
1.2 Thesis Outline . . . . .	8
<b>2 BACKGROUND</b> . . . . .	11
2.1 Kimberlite Pipes . . . . .	12
2.2 Geology . . . . .	13
2.2.1 Borehole Data . . . . .	14
2.3 The Seismic Reflection Survey . . . . .	16
2.3.1 Geometry and Data Acquisition . . . . .	16
2.3.2 Frontier Geosciences' Processing and Results . . . . .	17
2.4 The Transient Electromagnetic Survey . . . . .	20
2.4.1 Geometry and Data Acquisition . . . . .	21
2.4.2 Frontier Geosciences' Inversion and Results . . . . .	22
<b>3 METHODOLOGY</b> . . . . .	26
3.1 Seismic Reflection . . . . .	26
3.1.1 Processing . . . . .	27

3.2	Transient Electromagnetic . . . . .	31
3.2.1	Inversion Theory . . . . .	31
3.2.2	Inversion Process . . . . .	33
<b>4</b>	<b>SEISMIC REFLECTION RESULTS . . . . .</b>	<b>38</b>
4.1	Seismic Reflection Line 1 . . . . .	38
4.1.1	Individual Shot Gathers . . . . .	39
4.1.2	Stacked Images . . . . .	39
4.2	Seismic Reflection Line 2 . . . . .	45
4.2.1	Individual Shot Gathers . . . . .	45
4.2.2	Stacked Images . . . . .	48
<b>5</b>	<b>TRANSIENT ELECTROMAGNETIC RESULTS . . . . .</b>	<b>53</b>
5.1	Transient Electromagnetic Line 0300S . . . . .	54
5.2	Transient Electromagnetic Line 0100S . . . . .	60
5.3	Transient Electromagnetic Line 0100N . . . . .	63
<b>6</b>	<b>DISCUSSION . . . . .</b>	<b>66</b>
6.1	Seismic Reflection Results . . . . .	66
6.1.1	Comparison with Frontier Geosciences' Results . . . . .	66
6.1.2	Seismic Interpretation . . . . .	70
6.2	Transient Electromagnetic Results . . . . .	74
6.2.1	Comparison with Frontier Geosciences' Results . . . . .	74
6.2.2	TEM Interpretation . . . . .	79
6.3	Interpretation . . . . .	80
<b>7</b>	<b>CONCLUSION . . . . .</b>	<b>84</b>
7.1	Conclusions . . . . .	84
7.1.1	Seismic Reflection . . . . .	84
7.1.2	Transient Electromagnetic . . . . .	85

7.2 Future Work . . . . .	86
<b>Bibliography . . . . .</b>	<b>88</b>
<b>Appendices . . . . .</b>	<b>90</b>
<b>A A Sample Input File . . . . .</b>	<b>90</b>
<b>B A Sample Starting Model . . . . .</b>	<b>91</b>
<b>C A Sample Observation File . . . . .</b>	<b>92</b>

## List of Tables

6.1	Depth-conversion velocity model from results of GLI-3D refraction analyses for SL-1 and SL-2. . . . .	69
-----	--	----

## List of Figures

1.1	Terrane map showing the Lena West property location . . . . .	3
1.2	Plan of the Lena West property . . . . .	4
1.3	Plan of Area 1915 of the Lena West property . . . . .	6
2.1	Kimberlite pipe geometry . . . . .	13
2.2	Kimberlite pipe in seismic reflection section . . . . .	14
2.3	Surface geology of the Lena West property . . . . .	15
2.4	Previous stacked images for Seismic Lines 1 and 2 in Area 1915 . . . . .	19
2.5	General TEM survey geometry . . . . .	21
2.6	Previous 2-D apparent resistivity image for TEM Line 0100N in Area 1915 . . . . .	23
2.7	Previous 2-D apparent resistivity image for TEM Line 0100S in Area 1915 . . . . .	24
2.8	Previous 2-D apparent resistivity image for TEM Line 0300S in Area 1915 . . . . .	25
3.1	Split-spread geometry diagram . . . . .	27
3.2	Processing flow applied to seismic reflection data . . . . .	28
4.1	Shot gathers 1030, 1160 and 1246 from Seismic Line 1 . . . . .	40
4.2	Brute stack for Seismic Line 1 . . . . .	41
4.3	Intermediate stack for Seismic Line 1 . . . . .	43
4.4	Final stack for Seismic Line 1 . . . . .	44
4.5	Shot gathers 2045, 2132 and 2135 from Seismic Line 2 . . . . .	46
4.6	“Mirroring” anomaly in shot gathers 2049 and 2059 of Seismic Line 2 . . . . .	47
4.7	Brute stack for Seismic Line 2 . . . . .	49

4.8	Intermediate stack for Seismic Line 2 . . . . .	50
4.9	Final stack for Seismic Line 2 . . . . .	52
5.1	EM1DTM output for TEM Line 0300S; one receiver, 0.005 S/m reference model	55
5.2	EM1DTM output for TEM Line 0300S; three receivers, 0.005 S/m reference model . . . . .	56
5.3	EM1DTM output for TEM Line 0300S; one receiver, 0.2 S/m reference model	58
5.4	Smooth output for TEM Line 0300S . . . . .	59
5.5	EM1DTM output for TEM Line 0100S; one receiver, 0.005 S/m reference model	61
5.6	Smooth output for TEM Line 0100S . . . . .	62
5.7	EM1DTM output for TEM Line 0100N; one receiver, 0.005 S/m reference model	63
5.8	Smooth output for TEM Line 0100N . . . . .	65
6.1	A comparison of results for Seismic Line 1 . . . . .	67
6.2	A comparison of results for Seismic Line 2 . . . . .	68
6.3	A plot of interpreted results for Seismic Line 1 . . . . .	71
6.4	A plot of interpreted results for Seismic Line 2 . . . . .	72
6.5	A comparison of results for TEM Line 0100N . . . . .	76
6.6	A comparison of results for TEM Line 0100S . . . . .	77
6.7	A comparison of results for TEM Line 0300S . . . . .	78
6.8	A 2.5-D plot of TEM results . . . . .	79
6.9	A vertical log comparison of results from SL-1, SL-2, TEM Line 0100S, TEM Line 0100N and LW04-001 . . . . .	82

## **Acknowledgements**

First and foremost, I would like to thank Dr. Ron Clowes and Dr. Phil Hammer for the invaluable expertise they made available to me. I would also like to thank Dr. Colin Faruharson, Dr. Doug Oldenburg and Robert Eso for their assistance with the implementation of the EM1DTM algorithm. Finally, I would like to thank Dr. Ron Clowes, Dr. Doug Oldenburg and Dr. Erik Eberhardt for comprising my supervisory committee.

To Diamondex Resources Ltd. for making the Lac des Bois seismic reflection and TEM data available and allowing the project at the Lena West property, NT, to be the focus of this thesis.

## **Dedication**

*To my family*

## **Chapter 1**

### **INTRODUCTION**

During the past decade, Canada has become the third largest producer of diamonds in the world. This development followed the discovery of the first diamondiferous kimberlite pipe in the Archean Slave Province of the Northwest Territories by Charles Fipke and Stuart Blusson and their BHP Billiton partners in 1991 (Pell, 1997). The discovery led to the greatest staking rush in Canadian history. Subsequently, many kimberlite pipes were discovered throughout the Slave Province, although only a few are economically viable for diamond production.

The regional discovery led to the creation of the Ekati diamond mine, the first in Canada, which officially opened on 14 October, 1998. Since the opening of the Ekati diamond mine, several other diamond deposits have been discovered and three more mines have opened (Figure 1.1): the Diavik diamond mine, in 2003; the Jericho diamond mine located almost 200 km north in Nunavut in 2006; and the Snap Lake diamond mine, located about 150 km south of Ekati, Canada's first underground-only diamond mine and the only one where a kimberlite dyke rather than a pipe is the source, in 2007.

Following the Fipke-Blusson discovery, exploration for diamonds expanded to other areas of Canada where ancient cratons are known to exist. Kimberlite pipes have been identified in the Western Canada Sedimentary Basin (WCSB), where it is floored by Paleoproterozoic rocks in northwest Alberta; in central Saskatchewan where they are underlain by the recently discovered Archean Sask craton (i.e., Hajnal et al. (2005)); and in the Archean Superior Province of Ontario. Such successes have led many companies to look for diamonds in many areas of Canada.

In 2002, Diamondex Resources Ltd. applied for prospecting permits to explore the 6.15

million acre Lena West property for diamond and kimberlite indicator minerals (see Figures 1.1 and 1.2). The Lena West property is located in the District of Mackenzie, Northwest Territories, ~300 km northwest of Norman Wells and ~200 km southeast of Inuvik. Exploration began in 2003 with fluvial samples being collected to establish a regional baseline of indicator minerals; pyrope garnet and microilmenite were discovered in “encouraging concentrations” (McLean and Clarke, 2005).

Based on the indicator mineral concentrations discovered during the fluvial sampling in 2003, an airborne magnetic survey was conducted in 2004. Several magnetic anomalies were detected in the southern portion of the Lena West property during the airborne survey, prompting further investigation with a ground magnetic survey. Five magnetic anomalies were surveyed in the outlying portion of the property south of Lac des Bois. These anomalies consist of significant contrasts in magnetic intensity with the surrounding material and strong variations within the anomalies of approximately 2000 nT. Given the near-circular shape and strong magnetic intensity contrast, the anomalies could be caused by near-surface kimberlite pipes.

Thus far, only Archean kimberlites and lamproites are economically viable as production mines (LeCheminant and Kjarsgaard, 1996). A prominent diamond exploration consultant to Diamond Resources and Chief Research Geologist of the Russian Diamond Company, Dr. Nikolai Pokhilenko, has hypothesized that the Paleozoic and Mesozoic bedrock at the Lena West property is underlain by stable Archean crust, analagous to the Slave craton (McLean and Clarke, 2005). If this is true, then kimberlites in the Lena West property may be diamondiferous and therefore economically viable. Thus, further investigation was justified.

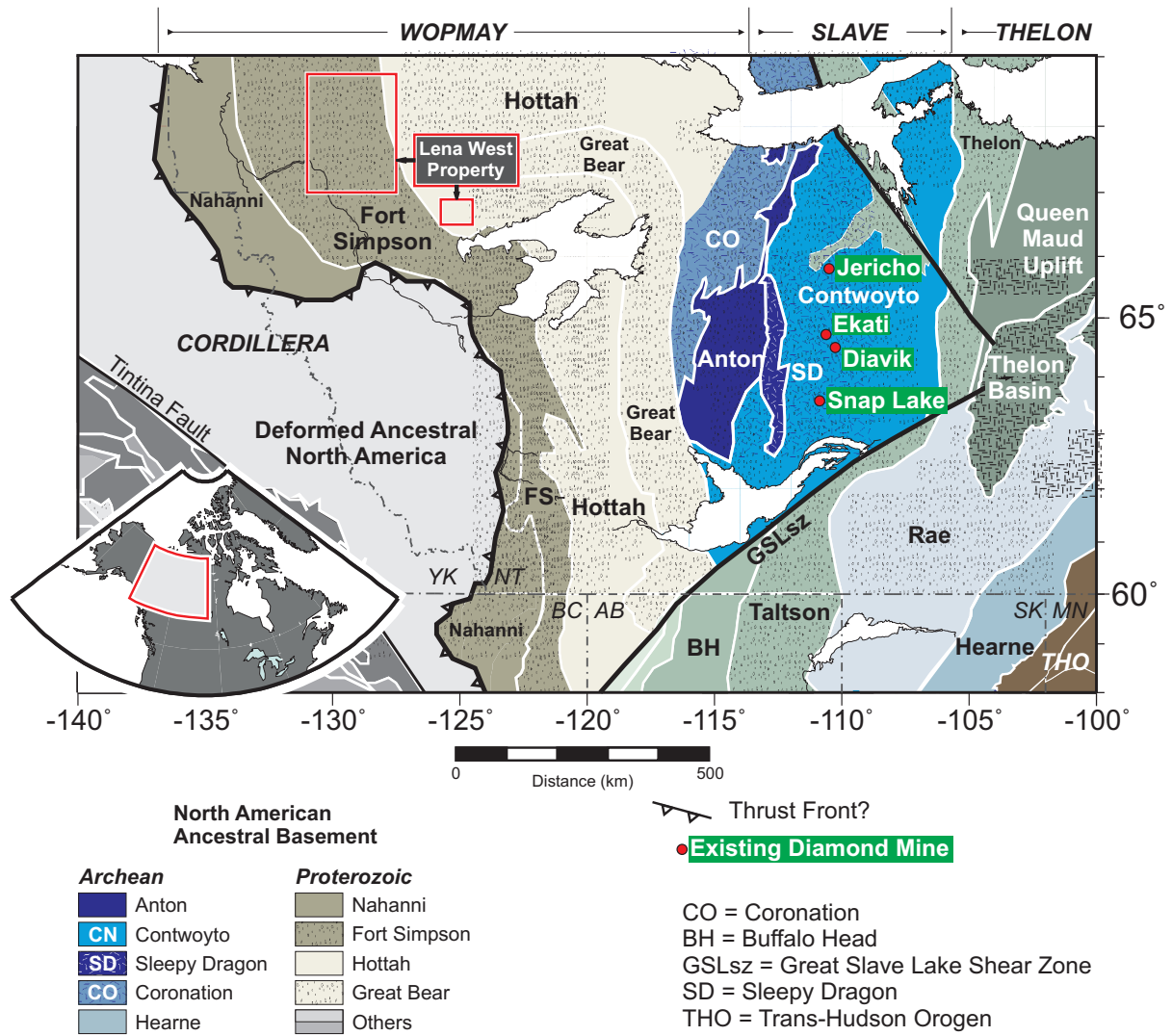


Figure 1.1: A terrane map showing the location of the Lena West property within the Fort Simpson and Hottah terranes in Canada's Northwest Territories. The Ekati, Diavik, Snap Lake and Jericho diamond mines are labelled with red circles.

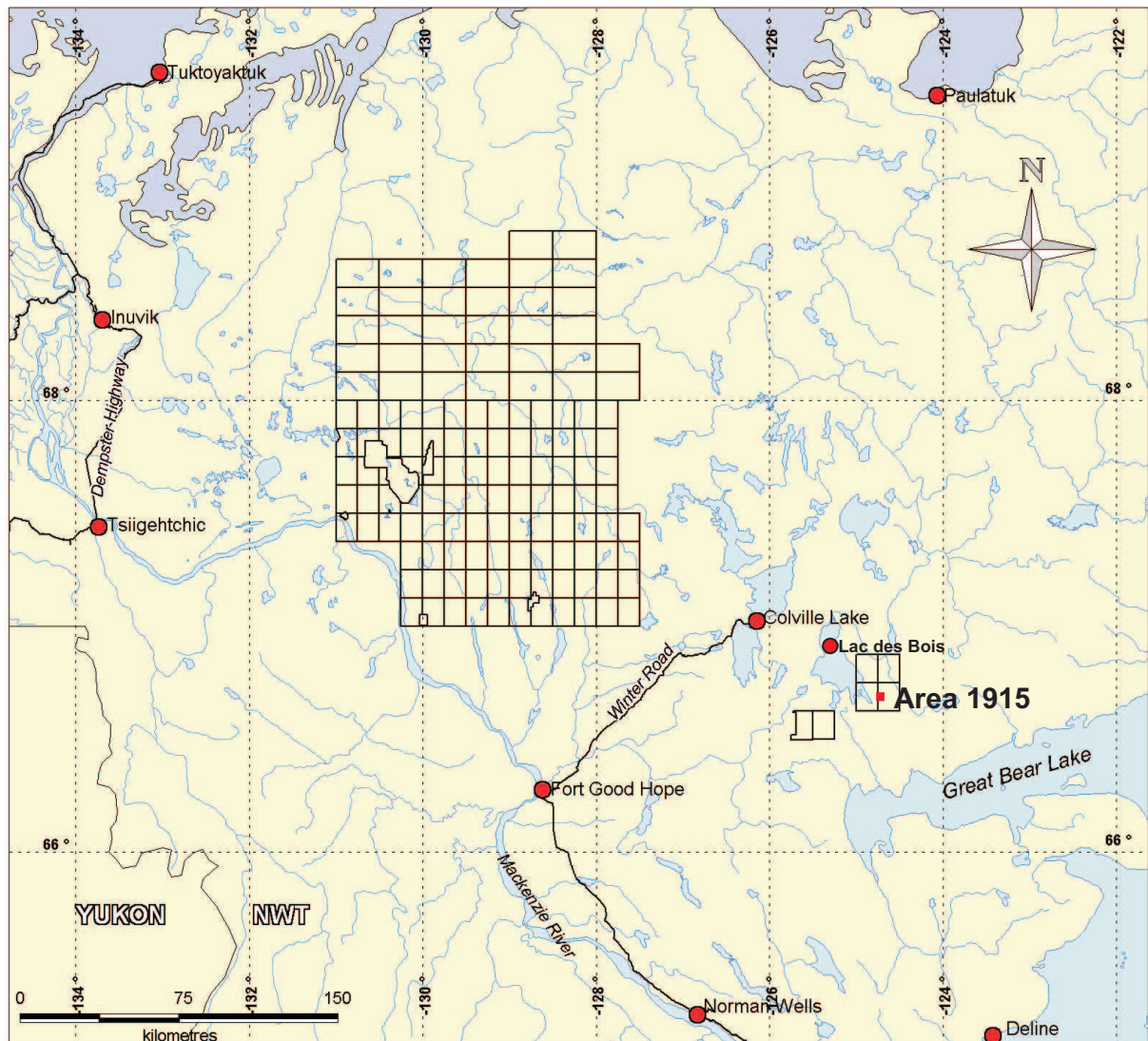


Figure 1.2: Plan view of the Lena West property, NT. Area 1915 near the south end of Lac des Bois is the focus of this study and is highlighted by the small red square. The black grid represents the prospecting permits that comprise the Lena West property. (Figure modified from McLean and Clarke, 2005)

In April 2005, Frontier Geosciences Inc. carried out a two-part geophysical study in the Lena West property on behalf of Diamondex Resources Ltd. in an attempt to gather more information on the subsurface materials where anomalies were detected during airborne and ground

magnetic surveys in 2004. The study consisted of nine seismic reflection lines and eleven time-domain transient electromagnetic (TEM) lines within four areas, each containing one or two magnetic anomalies. The seismic reflection method was chosen for its ability to determine approximate depths to strong reflectors and delineate horizontal reflector discontinuities. Lines of one-dimensional (1-D) TEM soundings were used to provide supplemental information regarding horizontal and vertical conductivity variations. The seismic lines intersected in the centre of each anomaly, while the TEM lines covered the area around and including the anomalies. Figure 1.3 shows the exploration layout for Area 1915, one of the four areas examined. Initial processing and interpretation of the seismic reflection and TEM data were carried out by Frontier Geosciences in 2005 and are described in Chapter 2. These were the survey results presented by the contractor to Diamondex Resources.

The UBC Geophysics group under Dr. Ron Clowes has a history of working with Diamondex Resources on other studies. Most importantly, they ran a unique seismic reflection experiment over the diamondiferous Snap Lake kimberlite dyke, a project that had excellent results (Hammer et al., 2004a; 2004b). In addition and following consultations with Diamondex Resources representatives, they recommended the field surveys for the Lena West property that were subsequently carried out by Frontier Geosciences. Through further discussions with Diamondex Resources following submission of the contractors report, the Geophysics group inquired whether the reflection and electromagnetic data sets could be made available for further processing and analysis since the contractor had used industry-standard procedures.

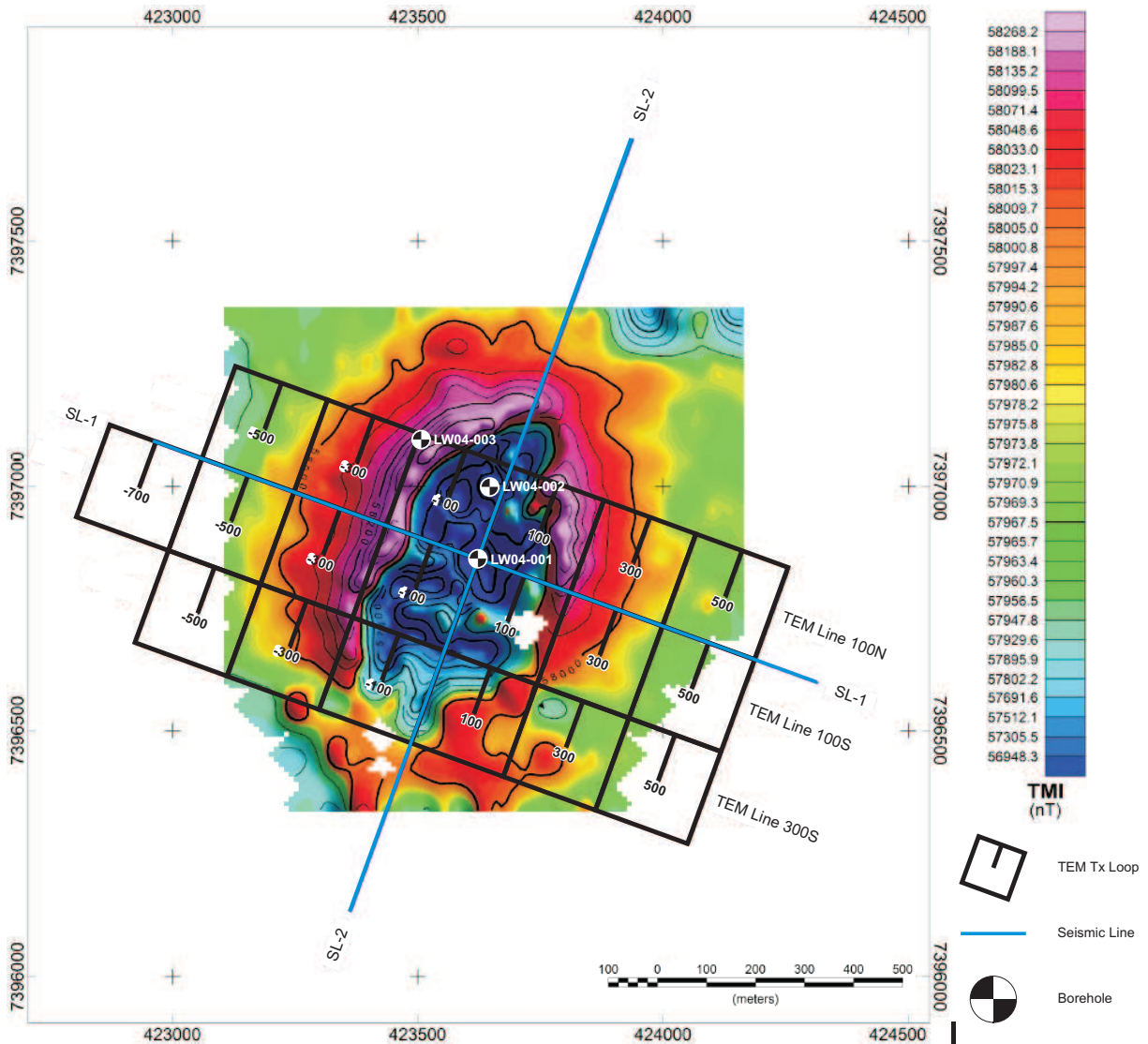


Figure 1.3: Plan view of Area 1915 showing two perpendicular seismic lines (SL-1 and SL-2) and three parallel TEM lines (0100N, 0100S and 0300S). The image includes the grid for NAD 83/UTM zone 10N with the survey details overlain on a plot of the local total magnetic intensity. Casino chips represent the locations of boreholes LW04-001, LW04-002 and LW04-003. (Figure modified from Payne and Candy, 2005)

The request was formulated on two bases. Firstly, the UBC Geophysical Inversion Facility (UBC-GIF; <http://www.eos.ubc.ca/ubcgif/>) had recently completed development of a new 1-D inversion algorithm (EM1DTM) that involved a different approach to analyzing TEM data

but had not yet been applied to field data. The expectation is that a more objective and better resolved resistivity cross-section than was achieved by the contractor could be generated using this new algorithm. Secondly, the UBC reflection seismology group has an industry-standard seismic processing software package (GLOBE *Claritas*; <http://www.globeclaritas.com/>) with additional capabilities based on the needs for research studies. With this package and more time to test different processing parameters with a variety of approaches, the expectation is that an improved seismic reflection image could be generated. As a minimum contribution, the image and results produced by the contractor processing would be verified.

Finally, the conduct of the reprocessing and analysis provides an opportunity for the author to learn about two very different procedures for analyzing two different types of geophysical data. Thus, the educational component of the study is high and relevant to employment opportunities in the geophysical exploration industry.

## 1.1 Objectives

The main technical objective of this investigation is to reprocess the seismic reflection data and invert the TEM data collected in Area 1915 near Lac des Bois in 2005 for the purpose of improving upon the previous processing and inversion results, thereby enabling a more comprehensive interpretation of the data. The main scientific objective is to compare the new processing and inversion results with the previous results to detect complementary or contradictory information, and also to compare the new results from seismic reflection and TEM inversions with each other and known geology from borehole data to generate a geological interpretation. The secondary scientific objective is to test the robustness of the 1-D, time-domain, electromagnetic inversion code EM1DTM when applied to real (non-synthetic) data, as such a test has yet to be made and published.

This study is divided into two main components. The first part consists of processing seismic

reflection data; the second part focuses on inverting the TEM data. The seismic reflection results are presented as detailed seismic images and yield information regarding sub-horizontal layering to depths of approximately 1100 m. The results of the 1-D TEM survey give information on vertical variations in conductivity, offering a rough outline of material variation. When all 1-D TEM results for one line are plotted together they yield a pseudo-2-D conductivity model. TEM surveys cannot penetrate as deeply as a seismic reflection survey, but for this survey yield useable results to depths of  $\sim 150$  m.

Determining the accurate structure of the subsurface through drilling only is uneconomical due to the vast amount of drilling that would be required. Using seismic reflection and TEM surveys, significant lateral variations or disruptions may be located much more efficiently. The results of this study may be used to guide and maximize any future drilling in Area 1915, or they may be used to dispel the need for any further exploration, given a strong lack of indication of a kimberlite pipe. They also could form the basis for re-processing and inversion of the reflection and TEM data from other areas, if such an undertaking were deemed beneficial by Diamondex Resources. Academically, this study offers an excellent opportunity to work with observed data from two different geophysical surveys and cross-interpret the results with one another as well as with known geology and previous results.

## **1.2 Thesis Outline**

The Lena West seismic reflection and TEM surveys near Lac des Bois and their respective interpretations were completed successfully by Frontier Geosciences. However, several seismic reflection pre-stack and post-stack processing steps were not taken in the initial study. Also, the EM1DTM code for inverting 1-D TEM data is a recent development, not generally available to industry, including Frontier Geosciences. This thesis examines the testing of many pre- and post-stack seismic processing steps. This thesis also investigates the results generated by

inverting the observed TEM data using the EM1DTM algorithm, developed by UBC-GIF.

The second chapter begins with a brief background on the geology near Lac des Bois. A summary of the seismic reflection survey is given, including survey geometry, data acquisition and the seismic reflection results attained by Frontier Geosciences Ltd. Finally, a summary of the TEM survey is given, including the details of the TEM survey geometry, data acquisition and inversion results generated by Frontier Geosciences Ltd.

Chapter Three describes the methods used in this study. The first section consists of a brief description of seismic reflection theory, followed by a thorough description of the processing work done. Relevant details from each step in the seismic processing sequence are defined and explained. The second section gives a brief description of TEM theory, followed by a comprehensive list of steps followed to carry out the inversion process. Programs used in this study include a seismic reflection processing package (GLOBE *Claritas*) and a 1-D time-domain electromagnetic inversion code (EM1DTM).

The fourth chapter completely describes the results of the seismic reflection processing of Line 1 and Line 2 for this project. Individual shot gathers and the various stacked images from both lines are shown and described.

Chapter Five describes the results of the TEM inversions of Lines 0300S, 0100S and 0100N from Area 1915. All steps and testing carried out on a specific line are described in this chapter. Results are shown as both 1-D plots and smoothed 1-D (pseudo-2-D) plots.

The penultimate chapter discusses the seismic reflection processing results and the TEM inversion results for Area 1915. Both seismic reflection and TEM results are compared with the results of Frontier Geosciences' 2005 study. A comparison between the seismic reflection and TEM results is made to try to correlate the results of different geophysical techniques used for a complementary understanding of a single site. Finally, the available borehole geology is incorporated into the interpretation to cross-check both geophysical results with known subsurface materials.

The final chapter states the interpretations of the seismic reflection and TEM results, along with the final interpretation of the subsurface structure, using all results with given geology. With respect to the technical objective, conclusions are made regarding the effectiveness and complementary nature of the two geophysical techniques used. Finally, a brief section is included to list and discuss any future work which may improve this study.

## **Chapter 2**

### **BACKGROUND**

The Lena West property is located in the Mackenzie Lowlands and covers 6.14 million acres of the Northwest Territories (Figure 1.2). A description of the exploration conducted in the Lena West property is given by McLean and Clarke (2005); a brief summary is given here. Fluvial sampling began in 2003 to establish a regional baseline of indicator minerals. Further fluvial sampling was carried out in 2004 to supply information in areas with low sample-density. In Spring 2004, an airborne gradiometer aeromagnetic survey was carried out by Fugro Air borne Surveys Quebec Ltd. and identified several magnetic anomalies within the southern portion of the Lena West property. Eighteen of the magnetic anomalies were investigated further in Summer 2004 with a ground magnetic survey conducted by Aurora Geoscience Ltd. A drilling program consisting of auger drilling and diamond drilling was only carried out within the outlying portion of the Lena West property, south of Lac des Bois, in 2004; no kimberlitic materials were observed. Five magnetic anomalies within four areas in the Lac des Bois portion of the Lena West property were prominent from the airborne and ground magnetic surveys, prompting a more thorough investigation (Payne and Candy, 2005).

In order to gain information regarding the subsurface structure, and on the recommendation of Dr. Ron Clowes and Dr. Phil Hammer of UBC Earth and Ocean Sciences, two different geophysical surveys were carried out in April, 2005 by Frontier Geosciences Inc. on behalf of Diamondex Resources Ltd. at the Lena West property near Lac des Bois: a seismic reflection survey and a time-domain transient electromagnetic (TEM) survey. The two surveys were carried out in four areas labelled 1906, 1907, 1915 and 1722. Area 1906 contains two magnetic

anomalies, while the other three areas each contain one. Nine seismic lines were surveyed with two seismic lines intersecting perpendicularly over each anomaly. Each anomaly had two or three TEM lines covering it, except the one in Area 1907, where no TEM survey was conducted. The seismic reflection and TEM data sets were processed and inverted, respectively, by Frontier Geosciences using industry standard geophysical data processing packages.

This subsurface exploration was carried out over the specific magnetic anomalies within the four areas of the Lac des Bois region of the Lena West property to help determine whether the strong lateral variations in total magnetic intensity (TMI) were caused by kimberlite pipes. Due to the high cost of drilling, the goal was to correlate the geophysical interpretations from both surveys to develop an efficient exploration drilling program.

## 2.1 Kimberlite Pipes

Kimberlite pipes are near-vertical volcanic intrusions initiating in the upper mantle that ascend to the surface very rapidly. During their ascent, kimberlite pipes can accumulate materials including diamonds from these great depths and bring them near the surface where their extraction becomes economically feasible. An idealized model of a Southern African kimberlite pipe is shown in Figure 2.1 (Pell, 1997). This vertical carrot-shaped geometry commonly generates a near-circular magnetic anomaly at the surface and does not need to be exposed at the surface to do so.

Several kimberlite pipes have been detected on petroleum industry seismic reflection data in the Buffalo Head Hills kimberlite field (Atkinson and Pryde, 2006). One example is shown in Figure 2.2. Interpreted pipe boundaries are shown as the light blue near-vertical lines, while interpreted diffractions from the sides of the pipe are highlighted with angled red lines. Strong lateral continuity in several reflection horizons is visible to either side of the interpreted pipe, while reflections between the pipe boundaries are clearly disrupted.

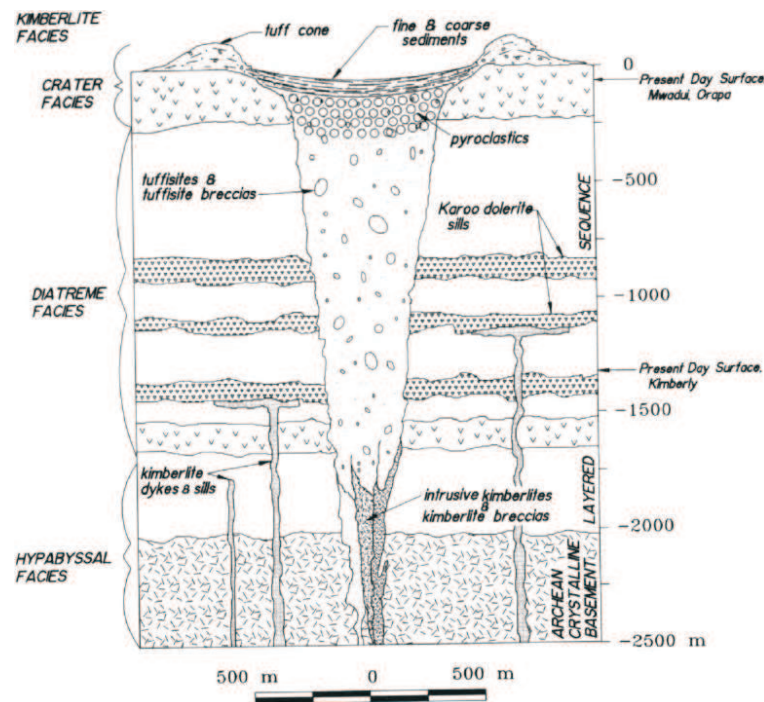


Figure 2.1: Idealized model of a Southern African kimberlite pipe. Figure from Pell et al. (1997)

## 2.2 Geology

The Lena West property is located in the District of Mackenzie approximately 200 km southeast of Inuvik and 300 km northwest of Norman Wells (McLean and Clarke, 2005), with a small portion of property near the south end of Lac des Bois (Figure 1.2). The surface topography and geology within each area near Lac des Bois is quite consistent, given the location and small size (i.e.,  $\sim 2.4 \text{ km}^2$  for Area 1915) of each survey area. The maximum known elevation change along either seismic reflection line in Area 1915 is 3.2 m over a surface distance of 520 m.

A complete description of the surface geology of the Lena West property is given by McLean and Clarke (2005); a summary of the geology near Area 1915 is given here. Figure 2.3 shows the surface geology of the entire Lena West property. Within Area 1915 of the Lena West property the Cretaceous-Bentonite formation dominates the surface geology. Near the southwest corner

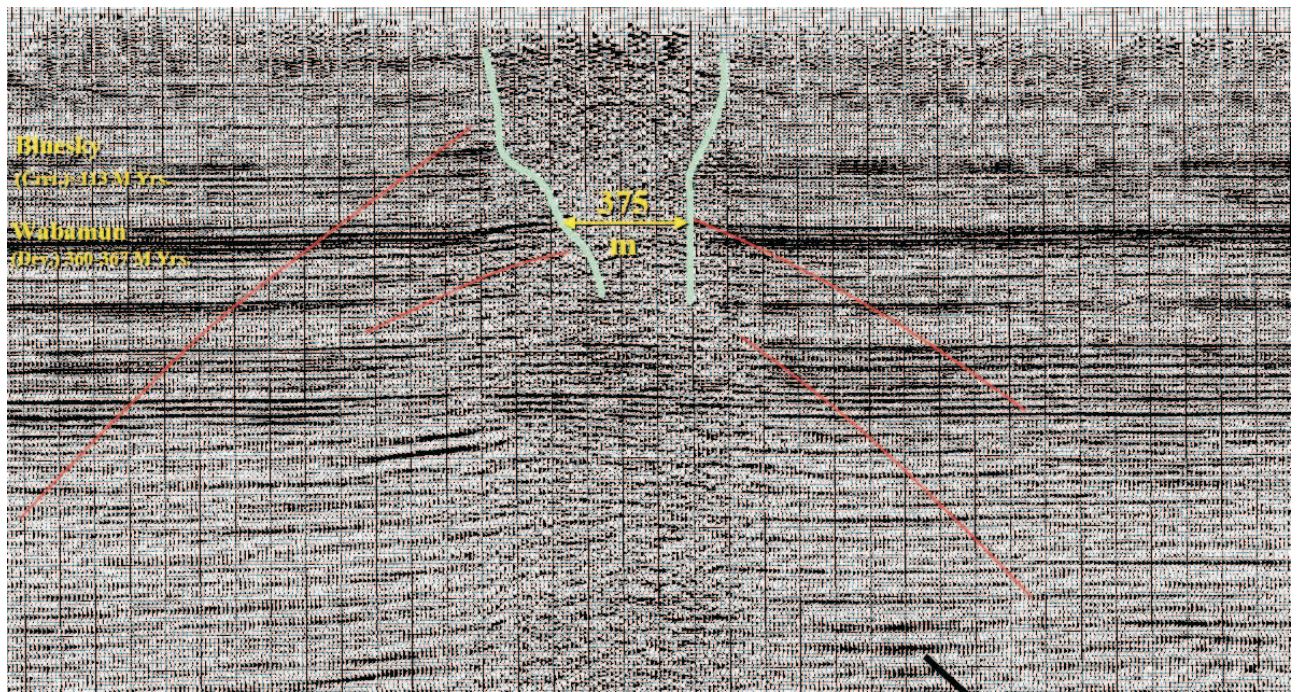


Figure 2.2: Seismic reflection results for K296 from Buffalo Head Hills kimberlite field with kimberlite pipe outlined in light blue. Red lines highlight diffractions from the side of the pipe. Figure from Atkinson and Pryde (2006)

of Area 1915, a transition to Cretaceous rocks occurs in the surface geology.

### 2.2.1 Borehole Data

Three drill logs from Area 1915 were made available for this study: LW04-001, LW04-002 and LW04-003 (locations shown in Figure 1.3). Crystalline basement was not encountered in any of the three drill holes. LW04-001 was located at the intersection of seismic line 1 (SL-1) and seismic line 2 (SL-2), and was terminated 212 m below surface. The overburden layer observed in LW04-001 is 32.77 m thick and is underlain by thin layers of limestone/dolomite, shale, limestone and mudstone to a depth of 43.35 m. Below 43.35 m, a dark grey/black mudstone extends to the end of the hole.

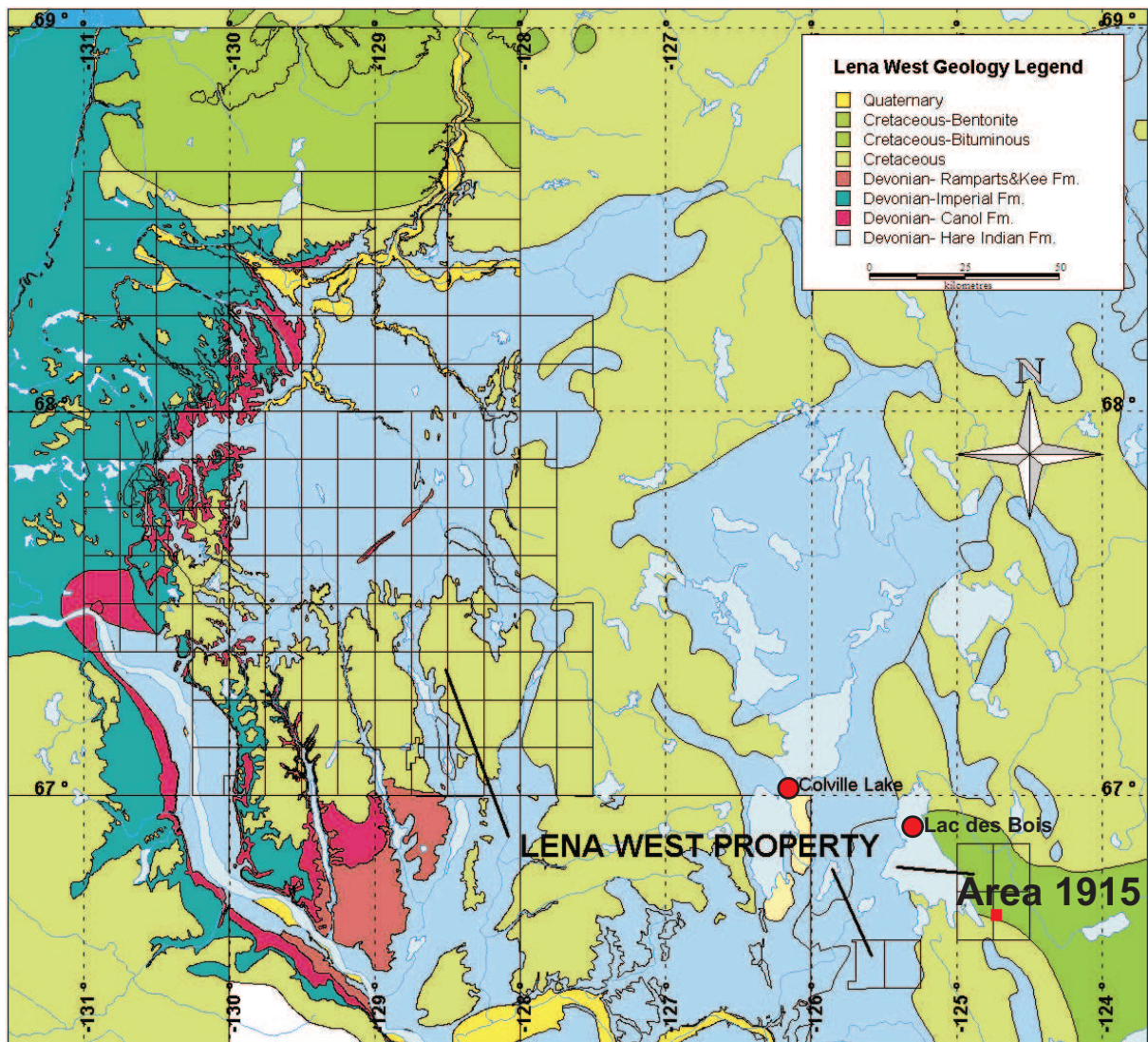


Figure 2.3: Plan view of the surface geology of the Lena West property, NT. Area 1915 near the south end of Lac des Bois is the focus of this study and is highlighted by the small red square. The black grid represents the prospecting permits that comprise the Lena West property. (Figure modified from McLean and Clarke, 2005)

LW04-002 is 160.6 m deep and is located approximately 150 m north of the intersection of SL-1 and SL-2, and 27 m away from SL-2. Overburden in this hole is 30.48 m thick and is underlain by 13.63 m of mudstone, shale and limestone. At 44.11 m below the surface a similar grey/black mudstone to LW04-001 begins and continues to 160.6 m. The mudstone layer is

interrupted by sand layers less than 2 m thick and one 6.28 m thick limestone layer.

LW04-003 is located approximately 276 m northwest of the intersection of SL-1 and SL-2, and was terminated within the overburden layer 65.53 m below the surface. Therefore, LW04-003 does not offer much information regarding the subsurface materials, other than that the overburden is more than 65.53 m thick.

The materials discovered in the aforementioned boreholes are consistent with strata ranging from Middle Devonian (Hare Indian Formation) to Lower Cretaceous (“Bentonite Zone”) in age. The overburden is considered a till blanket, which varies in thickness between the three boreholes, a common characteristic of areas exposed to significant glaciation.

### **2.3 The Seismic Reflection Survey**

The seismic survey, as designed by Frontier Geosciences and Diamondex Resources, consisted of nine seismic reflection lines throughout survey areas 1906, 1907, 1915 and 1722. Each area contained two perpendicular seismic lines, except for Area 1906, which contained three seismic lines (two parallel lines and one perpendicular line that intersected both parallel lines) due to the presence of two magnetic anomalies. The seismic lines intersected directly over the magnetic anomalies in order to offer information regarding the thickness of overlying sediments. Since kimberlite pipes cut through horizontal layers, the seismic reflection survey was also expected to highlight broken reflectors at depth, indicating a possible kimberlite pipe boundary.

#### **2.3.1 Geometry and Data Acquisition**

The seismic reflection survey utilized a split-spread geometry with 48 seismometers (geophones or receivers) recording at a sampling interval of 0.5 ms. The receiver spacing was 5 m, yielding 235 m-wide shot gathers, and the shots were always located in-line directly between receivers 24 and 25 (i.e., 2.5 m from either shot). The source was moved in 5 m increments, yielding

24-fold redundancy, where fold is the number of times a single subsurface point is illuminated by the energy from different shots.

A small dynamite charge was used as the source for each shot gather. For each shot in this type of survey, a near-surface hole is drilled into the ground to provide as good coupling as possible between the source and the intact subsurface material. The process of drilling a hole and ensuring strong coupling between the source and surrounding material is important in maximizing the amount of acoustic energy that is transmitted into the subsurface. Some of this input energy reflects or refracts and returns to the surface and is recorded by the survey receivers.

Three Geometrics Geode signal enhancement seismographs and Mark Products Ltd. 14 Hz seismometers were used to record the data. Each receiver is typically pushed or hammered into the ground in accordance with the survey geometry. As with the source, it is important that the receivers be well-coupled with the ground to ensure the maximum amount of energy is transferred to and recorded by the receiver.

The only area considered in this study is Area 1915. Therefore, the only results shown or referred to from Frontier Geosciences are those from Area 1915, which consist of two seismic lines and three TEM lines (see Figure 1.3). Seismic line 1 is 1550 m in length, consisting of 264 shots, and is oriented North 70° West. Seismic line 2 consists of 312 shots, covering 1790 metres along the surface, and is oriented perpendicular to SL-1 at North 20° East.

### **2.3.2 Frontier Geosciences' Processing and Results**

The complete report including the seismic reflection processing is presented in Payne and Candy (2005); a summary of the processing steps taken is given here. Frontier Geosciences carried out a standard industry seismic reflection processing sequence, using WinSeis (<http://www.kgs.ku.edu/software/winseis/winseis.html>) and Seismic Unix (SU; <http://www.cwp.mines.edu/cwpcodes/>) to process the data. The data were recorded as 750 millisecond seismograms in SEG2 format

and converted into floating point SU format. Noisy traces, which would have deleterious effects on subsequent processing, were removed from the shot gathers and the data were sorted into common mid-point (CMP) gathers. Next, a first break analysis was carried out in order to apply refraction statics that removed the effect of a near-surface low velocity layer. The first breaks were then muted to prevent this energy from reducing the signal-to-noise ratio. A velocity analysis of the CMP gathers was carried out in order to build a velocity model for each line. A band-pass filter was applied to limit the frequency range of the CMP gathers and a 70 ms automatic gain control (AGC) was used to balance trace amplitudes. Next, a normal moveout correction was applied using the velocity model previously developed. Finally, the CMP gathers were stacked together and the stack was converted into SEG-Y format for input into the Seismic Micro Technologies (SMT) 2-D/3-D seismic interpretation package. This package was used to interpret horizons within the final stacked image.

Using the SMT interpretation package, the final results of SL-1 and SL-2 were interpreted to contain two main horizontal reflections at approximately 320 m and 390 m depth. The stacked seismic sections are shown for SL-1 and SL-2 in Figure 2.4. Compressional wave velocities were determined from a (limited) refraction analysis to range between 2500 m/s and 4000 m/s in the upper 40 m of the section.

The final stacked image for SL-1 generated by Frontier Geosciences shows some minor undulations in portions of the strata from -600E to -200E and from 0E to 400E between depths of 250 m and 350 m. Below the first interpreted horizontal reflector ( $\sim 320$  m) the underlying reflections appear to be broken across the image. The second interpreted reflection horizon seems to be a connection of several laterally broken reflections, leading to a more jagged and less realistic continuous reflector interpretation. SL-2 intersects SL-1 at station 0E.

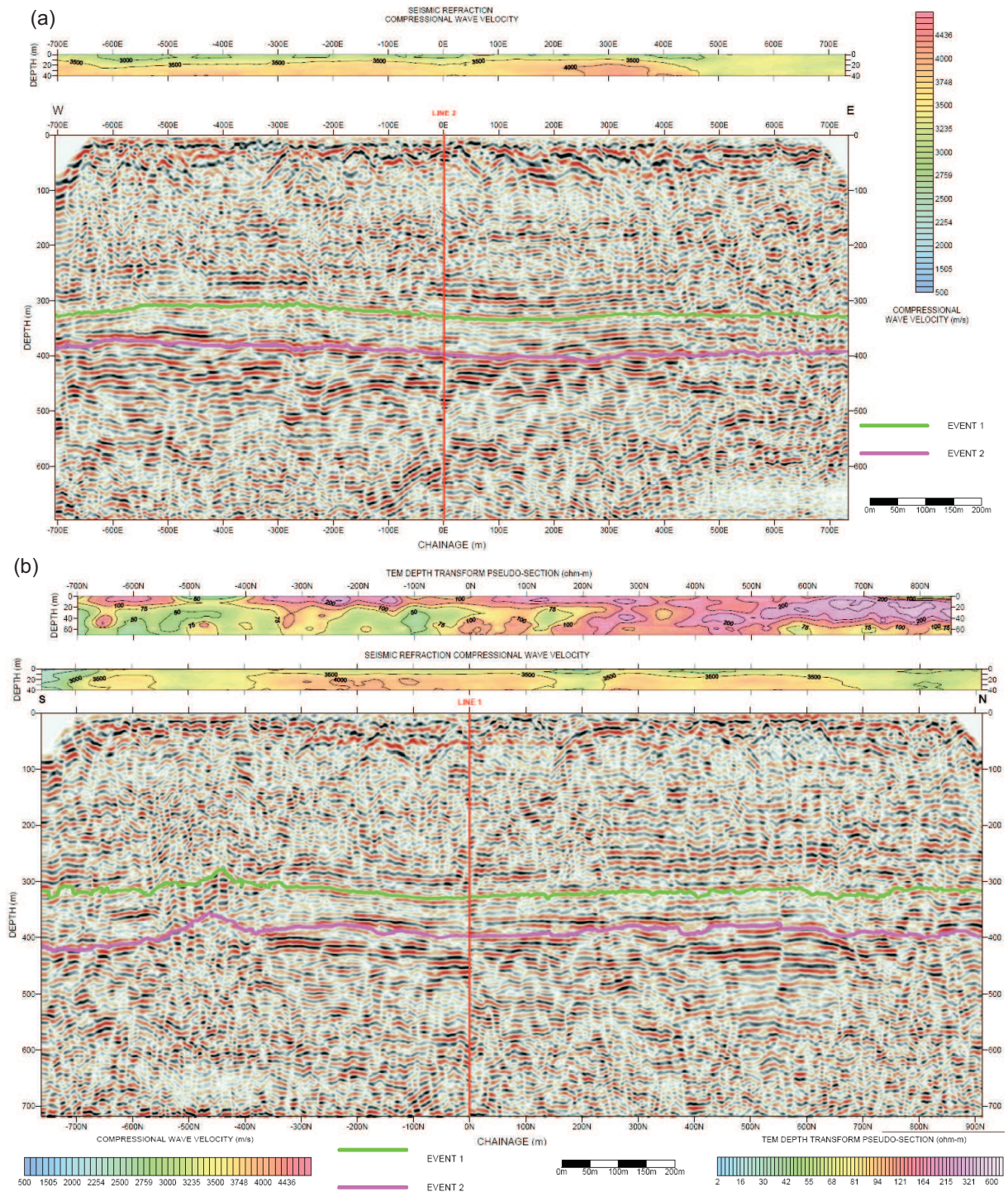


Figure 2.4: Stacked seismic reflection images from Frontier Geosciences for SL-1 and SL-2 in Area 1915 (Payne and Candy, 2005). The stacked images extend from the ground surface to ~700 m. The processed line lengths for SL-1 and SL-2 are 1430 m and 1690 m, respectively. Two interpretations on each line (events 1 and 2) were generated using the SMT interpretation package. Red lines represent where SL-1 and SL-2 intersect. Velocities from the seismic refraction analyses are shown for the upper 40 m for both lines. An apparent resistivity pseudo-section for the upper 60 m is shown for SL-2.

Frontier Geosciences' final stacked image for SL-2 exhibits better lateral continuity than that of SL-1. Slightly undulating horizontal reflections are nearly continuous from -800N to -600N and from -400N to 650N between depths of 250 m and 300 m. The reflections underlying the first interpreted horizontal reflector are less laterally continuous; however they are more continuous than reflections at similar depths in SL-1. Both interpreted horizontal reflectors seem to form a peak between -500N and -400N, even though this area does not exhibit strong continuity. Also, neither of the two interpreted horizontal reflectors align with stronger nearby reflection horizons. SL-1 intersects SL-2 at station 0N.

Based on the seismic reflection results from Frontier Geosciences, SL-1 and SL-2 both exhibit broken horizontal reflection continuity across their final images, neither line actually containing a continuous reflection from one end to the other. Both lines illustrate similar structure in the form of some undulating horizontal reflections between 250 m and 350 m depth with less continuous reflections visible below to a depth of  $\sim 500$  m. All interpreted horizontal reflectors are jagged and do not always follow strong reflections, indicating a less realistic interpretation of where vertical changes occur.

#### **2.4 The Transient Electromagnetic Survey**

Frontier Geosciences carried out TEM surveys in areas 1915, 1906 and 1722, totalling 11 lines. Areas 1906 and 1722 contain six and two TEM lines, respectively, based on the size and number of anomalies in either area. Area 1915 is centred at 7396900/423600 in UTM zone 10N and contains three TEM lines. The TEM survey was designed such that the TEM lines extend beyond the magnetic anomalies and cover some of the surrounding area in order to offer information on resistivity variations across and beyond each anomaly.

### 2.4.1 Geometry and Data Acquisition

Each TEM line consisted of between three and seven 200 m by 200 m transmitter loops, with receiver loops located inside and outside the transmitter loop, as illustrated in Figure 2.5. Typically, one sounding would be carried out for both x- and z- receiver orientations and with the receiver both inside and outside the transmitter loop, effectively generating four receivers for each sounding. The data recorded from these four receivers can be inverted together to increase the signal-to-noise ratio; however, any data not consistent with a 1-D subsurface structure will lead to conflict when using a 1-D inversion algorithm.

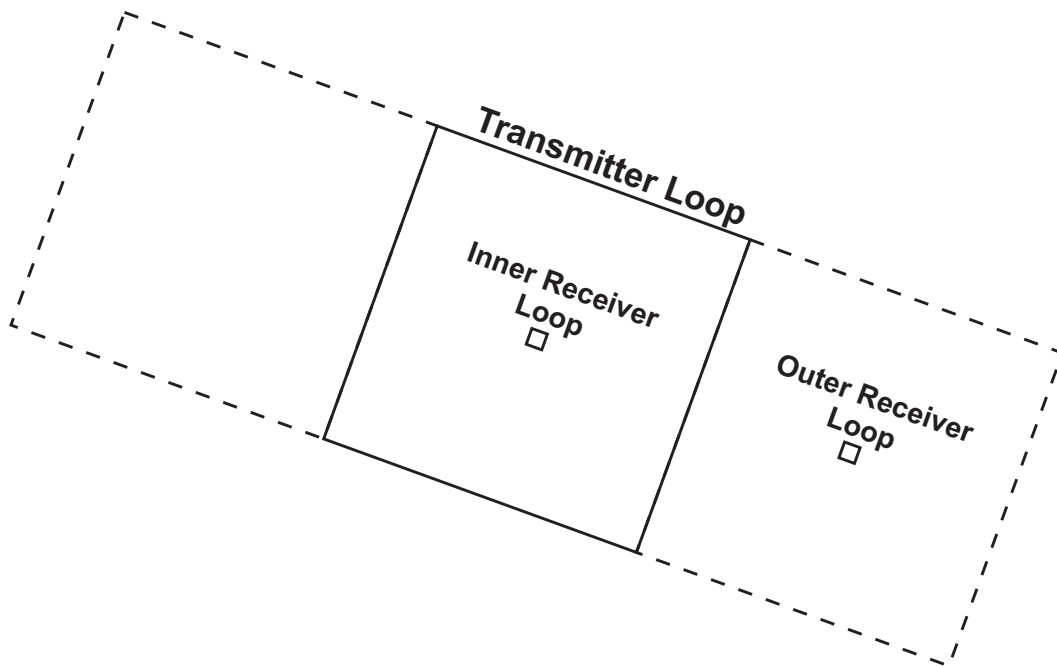


Figure 2.5: TEM survey geometry for a typical sounding in Area 1915. Adjacent transmitter loops are illustrated as dashed boxes. The receiver loop locations for the solid transmitter loop are shown in the centre of the transmitter loop and 200 m down the line.

The Geonics Ltd. Protem Transient EM system was used to carry out this survey. Two sources were used in order to examine different depths by using different frequencies. The TEM-37 was used for lower frequencies of 3 Hz, 7.5 Hz and 30 Hz which are effective to depths

greater than 1000 m, while the TEM-47 was used for high frequencies of 75 Hz and 285 Hz for shallow depth information. The waveform produced by the transmitters was a bipolar rectangular current with a step-off. The TEM-37 and TEM-47 transmitters used a 100  $\mu\text{s}$  and 18  $\mu\text{s}$  turn off time, respectively.

Protem receivers were used during the TEM survey. Two different receiver loop sizes were used, depending on the transmitter being used. A 100 m<sup>2</sup> receiver loop was used in conjunction with the TEM-37 transmitter, while a 31.4 m<sup>2</sup> receiver loop was used with the TEM-47 transmitter. Each receiver repeatedly recorded 20 channels over a 30 second period, stacking the data continuously to improve the signal-to-noise ratio. The observed data were stored in gain-uncorrected millivolts until processing began.

As stated before, Area 1915 is the only area examined in this study. The three parallel TEM lines surveyed in Area 1915 are: 0100N, 0100S and 0300S (see Figure 1.3). Line 0100S consists of seven transmitter locations, while Lines 0100N and 0300S consist of six transmitter locations. Each transmitter loop was placed adjoining the next loop in the line and each line was adjoining the next line. The TEM lines in Area 1915 were oriented parallel to SL-1 at North 70° West.

#### **2.4.2 Frontier Geosciences' Inversion and Results**

The complete report including all steps taken in the TEM survey and inversion, and appropriate interpretations, are included in Payne and Candy (2005); a brief summary of the inversion steps taken is given here. Frontier Geosciences first normalised the observed data from gain-uncorrected millivolts to units of time derivative of the magnetic field (nanovolts/m<sup>2</sup>). Next, the data were converted to apparent resistivity and plotted against time in log-log format. The data were finally modelled using the inversion code TEMIXGL to produce a 2-D section of apparent resistivities.

Frontier Geosciences' 2-D section of apparent resistivities for Line 0100N is shown in Figure 2.6. In this figure, the depth ranges from surface (0 m) to 400 m below the surface, while the lateral distance varies from -500E to +500E. The image shows a moderate resistivity ( $\sim 200 \Omega\text{m}$ ) near-surface layer from the surface to a depth of  $\sim 100$  m, underlain by a low resistivity ( $10\text{-}30 \Omega\text{m}$ ) layer to a depth of  $\sim 280$  m. The low resistivity layer is above a transition layer which changes from  $\sim 30 \Omega\text{m}$  to  $\sim 2100 \Omega\text{m}$  within  $\sim 70$  m. Below this transition layer is a high resistivity ( $\geq 2000 \Omega\text{m}$ ) layer continuing to the bottom of the section. The image shows a slight increase in thickness of the low resistivity layer toward the right (eastern) end of the line, but otherwise exhibits minimal lateral variation. Frontier Geosciences provides no geological interpretation of their apparent resistivity sections.

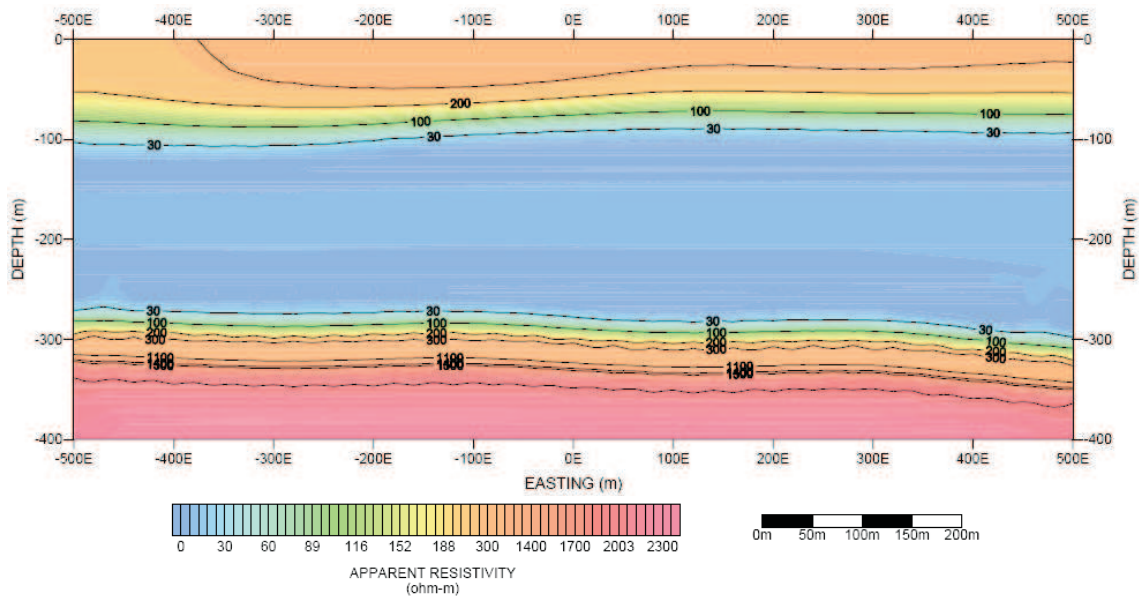


Figure 2.6: Frontier Geosciences' output from TEMIXGL for TEM Line 0300S in Area 1915 (Payne and Candy, 2005). The apparent resistivity section is 400 m deep and 1000 m wide.

Figure 2.7 shows the 2-D section of apparent resistivities for Line 0100S vertically between the surface and 400 m below the surface, and laterally from -700E to +500E. The TEM results

for Line 0100S show a similar resistivity pattern with only slight thickness variations. The average thicknesses are the same as those in Line 0100N, but there are some undulations along the contacts between each main resistivity layer, making this line less laterally consistent. No major lateral discontinuity is discernible in this section.

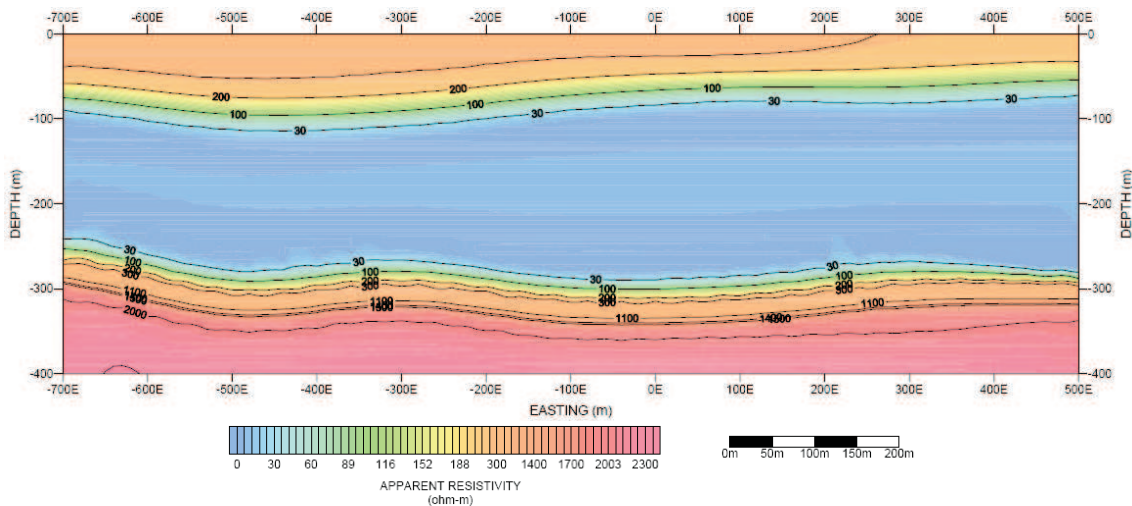


Figure 2.7: Frontier Geosciences' output from TEMIXGL for TEM Line 0100S in Area 1915 (Payne and Candy, 2005). The apparent resistivity section is 400 m deep and 1200 m wide.

The 2-D section of apparent resistivities for Line 0300S is shown in Figure 2.8. The image extends vertically from the ground to 400 m below ground surface and laterally from -500E to +500E. The TEM results for Line 0300S are very similar to those of Line 0100N in terms of conductivity structure and lateral continuity, except at the eastern end. The sounding centred at +500E contains a thinner and slightly shallower low resistivity layer than the other five soundings, causing a slope between  $\sim 270$  m and  $\sim 200$  m depth at the eastern end of the line.

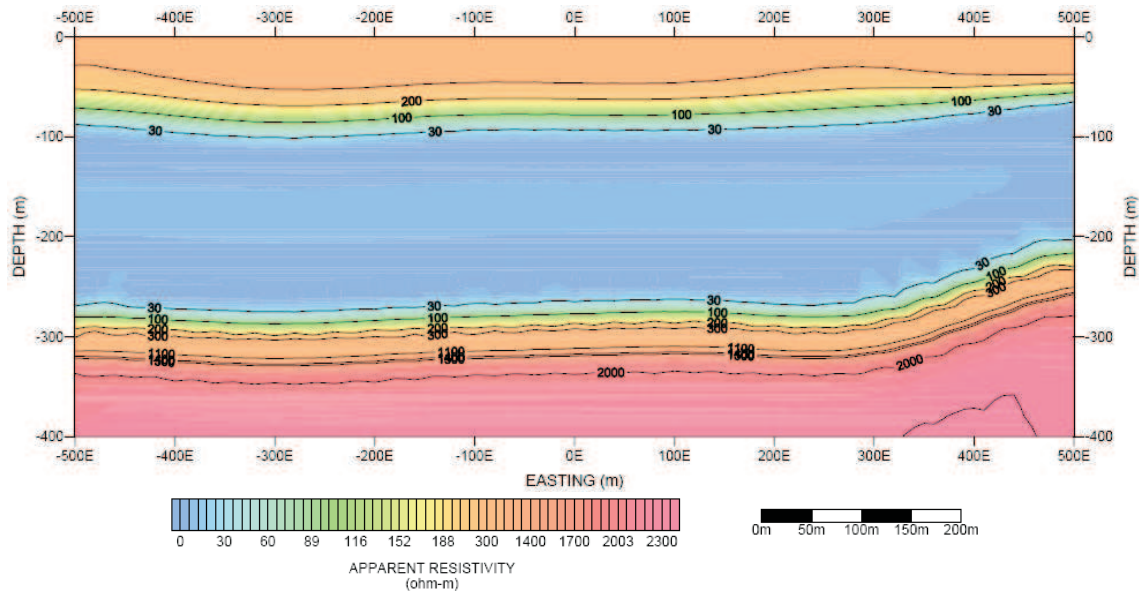


Figure 2.8: Frontier Geosciences' output from TEMIXGL for TEM Line 0300S in Area 1915 (Payne and Candy, 2005). The apparent resistivity section is 400 m deep and 1000 m wide.

All three TEM lines surveyed and inverted in Area 1915 exhibit the same general resistivity-depth structure: moderate resistivity for ~100 m, low resistivity for ~150 m, moderate resistivity for 50 m finally becoming high resistivity to the bottom of the 2-D section. Frontier Geosciences concluded that the low-to-high resistivity boundary coincides with the reflection horizon identified at ~320 m in the seismic reflection sections.

## **Chapter 3**

### **METHODOLOGY**

Exploration seismology involves the controlled use of a sound source, typically explosives or vibroseis on land, and the recording of the subsequent ground motion at predetermined surface positions. Transient electromagnetic (TEM) surveys consist of passing electric current through a wire loop of known dimensions, inducing currents, and subsequently secondary magnetic fields, in nearby magnetic bodies. A receiver loop is used to measure the exponential decay of these secondary magnetic fields. Both types of data can be processed or inverted to generate a 2-dimensional depth section, offering information on vertical and horizontal structural variations. This chapter focuses on describing the processing sequences that were carried out by the author on both types of data to achieve a final result. The results from the seismic reflection and TEM processing sequences are presented in Chapters 4 and 5, respectively, and discussed in Chapter 6.

#### **3.1 Seismic Reflection**

Following the explosion of a source located near the surface, acoustic waves travel through the earth, refracting through subsurface layers and reflecting from layer interfaces with high impedance contrasts. Explosive sources are used because they offer a very sharp input pulse, from which reflections become more easily discernible than if a broad input pulse were used. Other sources such as vibroseis, which involves the use of heavy trucks vibrating across a specified range of frequencies, are available for use in exploration seismology, but are not relevant to this survey and are therefore not discussed further.

The 2005 seismic reflection experiment included two lines in Area 1915. Both seismic lines consisted of shot gathers being collected at specific locations. Each shot gather utilized a symmetric split-spread geometry, standard for regions of unknown subsurface geology, consisting of a line of receivers with the source located at the centre (Figure 3.1), and recorded data for 511.5 ms. With a source and receiver spacing of 5 m, reflectors are illuminated every 2.5 m along the line. With an average compressional velocity of 4400 m/s, the maximum depth of the stacked sections is  $\sim 1120$  m.

ref

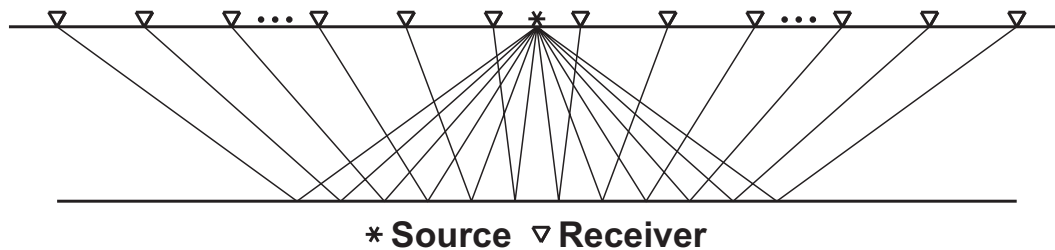


Figure 3.1: A diagram of split-spread geometry. Receiver spacing is constant, with the source located between the centre-most receivers. Split-spread geometry was used exclusively to survey SL-1 and SL-2 in Area 1915.

### 3.1.1 Processing

All seismic reflection data were processed using *GLOBE Claritas*, a package that allows the user to create individual modules to carry out specific processing steps. These modules were designed to be used in a specific order to complete the processing flow. The processing sequence applied to SL-1 and SL-2 is described below and illustrated in Figure 3.2.

The observed seismic reflection data were received from Diamondex Resources Ltd. in SEG2 format; therefore the first step was to convert these data into SEG-Y format for input into *GLOBE Claritas*. The geometry for both lines was straight and, because the processing yields a vertical 2-D plane in any orientation, could therefore be modelled as east-west or north-south.

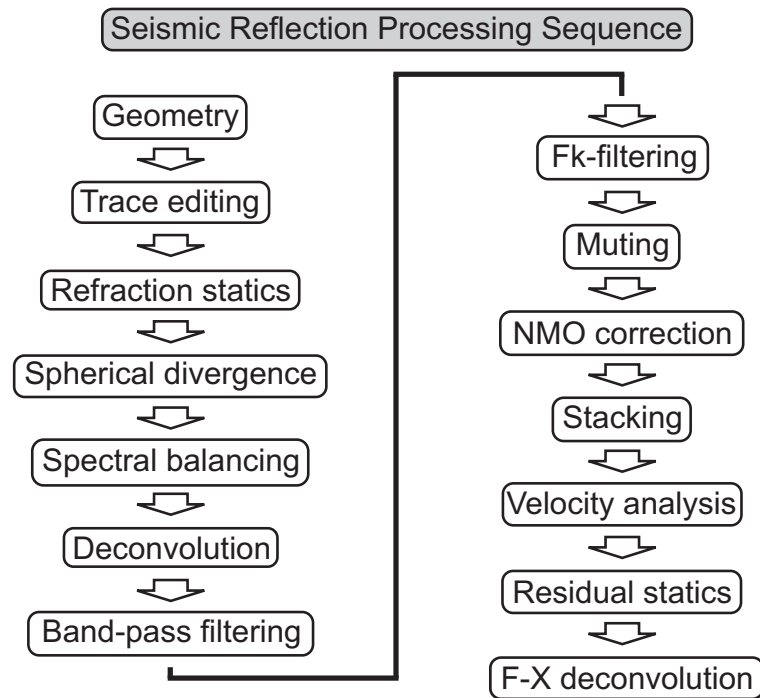


Figure 3.2: The processing flow applied to SL-1 and SL-2 from Area 1915.

Elevation information was supplied for both lines from a local gravity survey, however information at the ends of each line were unavailable. For all points where elevation information was unavailable, a value equal to the closest known value was assumed, making the elevation flat where data were not provided. In order to remove any erroneous data, Seismic Quality Control (SQC), a tool within GLOBE *Claritas*, was used to examine the data and pick out each dead trace. The first processing module created using GLOBE *Claritas* read in the SEG-Y data file, incorporated the geometry information into the shot gathers and applied mutes to eliminate all previously determined dead traces.

Once the survey geometry information was added to the shot gather headers, first-break picking could be carried out. This step involved selecting a point on each trace, for every shot, where the first arrival occurred, and was also done using SQC. First-break picks were used to complete the refraction static analyses. Three different refraction static analyses were carried

out for this study: refstat, the built-in refraction static tool within GLOBE *Claritas*; the generalized linear inversion method within the GLI-3D package of Hampson-Russell Software Services Ltd.; and the tomographic method, also within the GLI-3D package. The data were all datumed to 313 m above sea level, a point slightly higher than the highest elevation of either line.

Trace editing was once again done using SQC to determine and flip any polarity-reversed traces, and to design mutes to remove refracted arrivals and a mute that, when included in the processing flow, would effectively allow only far-offset traces to be stacked. The latter mute consisted of a rectangular mute removing traces 16 through 33, inclusive, thus only allowing offsets of 47.5 m or greater to continue in the processing sequence. This mute was designed and tested. However, the benefits were not significant so this step was omitted from the processing sequence.

Yilmaz (1987) describes the basic processing procedures for seismic reflection data. In this study, all pre-stack processing steps were included in one module. These steps included spherical divergence, spectral balancing, deconvolution, band-pass filtering,  $f-k$  filtering, and muting. Spherical divergence is used to compensate for the dissipation of wave energy as it expands away from the source, thus increasing amplitudes representing reflectors at greater distances from the source. High frequencies are commonly overshadowed by low frequencies, particularly in areas affected by groundroll or air waves. Spectral balancing is applied to increase the amplitudes of the more attenuated frequencies (high frequencies) relative to the low frequencies that have higher amplitudes prior to the balancing. Deconvolution compresses the basic wavelet in the recorded seismogram, attenuates reverberations and short-period multiples and increases temporal resolution, and is therefore an important processing step. Filtering is commonly used to remove desired frequencies in observed data. Band-pass filtering was used in this study to remove frequencies below 80 Hz, which were responsible for many noisy reverberations, and above 160 Hz, which were mainly extraneous noise. Frequency-wavenumber,  $f-k$ , filtering was

used to remove energy which had a clear and constant slope in the shot gathers that was significantly different from any reflectors, such as ground roll and refracted arrivals. Previously designed mutes were applied in this module.

After the pre-stack processing steps are applied, the data must be sorted into constant depth point (CDP) gathers. A CDP gather is the group of individual traces that have reflected from the same subsurface point. These traces are organized together in relation to their spatial offset, and therefore any reflectors will form a hyperbolic curve. In order to change these hyperbolic curves into horizontal lines, we apply a normal moveout (NMO), which is a velocity correction applied to a CDP. Once the static corrections and NMO corrections are applied correctly, the reflector should be one horizontal waveform and is ready to be stacked. Stacking is the summing of each trace in a CDP gather in order to cancel out noise and enhance any reflected signals due to destructive and constructive interference, respectively. The stacks produced at this point in the processing sequence are referred to as intermediate stacks, and are plotted with automatic gain control (AGC) applied to make all reflections as visible as possible.

Once the shot gathers have been stacked using guessed velocity values for an initial NMO correction, a velocity analysis was conducted using the constant velocity analysis (CVA) tool within GLOBE *Claritas* to create a detailed velocity model across the section. Constant velocity gathers were examined across each line wherever a reflector was clear. The resulting velocity information was then applied as a new NMO correction to all subsequent stacks for each respective line.

Post-stack processing involved two main steps: residual statics and  $f$ - $x$  deconvolution filtering. Residual statics were applied to fine-tune any vertical variations previously missed or caused by applying the NMO correction. This step improved the lateral continuity of horizontal reflectors, and enhanced some reflectors which were previously hidden.  $F$ - $x$  deconvolution filtering was used to remove incoherent random noise in the final stacked image. The FXDECON

processor within GLOBE *Claritas* was applied to the residual static-corrected stack, greatly increasing the signal-to-noise ratio. *F-x* deconvolution filtering was the last processing step applied to the data. The final stack was plotted with AGC applied to emphasize all reflections within the section.

## 3.2 Transient Electromagnetic

Electric current passing through a loop of wire creates an induced primary magnetic field surrounding the wire. This induced magnetic field generates secondary electric currents in conductive bodies within the magnetic field. Consequently, these secondary electric currents generate secondary magnetic fields, which can be measured at the surface. An electromagnetic survey consists of carrying out this procedure over a designated area, and yields information regarding the resistivity of electrical conductivity properties of the subsurface.

Frontier Geosciences' 2005 survey consisted of three TEM lines in Area 1915. The two outer lines consisted of six transmitter loops, while the centre line consisted of seven loops. Collecting data for each transmitter location involved recording with a receiver loop at two orientations in two locations (see Figure 2.5). All four sets of data for each transmitter loop were recorded and continuously stacked over 30 seconds. The data were originally inverted using TEMIXGL to generate 2-D depth sections of apparent resistivity.

### 3.2.1 Inversion Theory

The complete theoretical background for EM1DTM is given by Farquharson (2006); a brief description of the inverse problem is given here. The mathematical representation, or model, of the subsurface is given as a series of layers with fixed thicknesses and constant conductivities within each layer. During the inversion, the linear approximation of the non-linear problem is solved iteratively. At each iteration the conductivities within each layer are allowed to change,

while the thicknesses remain fixed. Therefore, many layers are necessary to allow for many possible models to be created. The EM1DTM algorithm aims to generate the simplest model (i.e., one with minimum-structure) that adequately reproduces the data. This is accomplished by minimizing the objective function,  $\Phi$ , by trading off between more accurately reproducing the data (low data misfit) and maintaining a minimum-structure model (low model norm). The general form of the objective function is defined as:

$$\Phi = \phi_d + \beta\phi_m, \quad (3.1)$$

where  $\beta$  is the regularization, or trade-off, parameter between minimizing data misfit and model structure,  $\phi_d$  is the data misfit and  $\phi_m$  is the model-structure component. The regularization parameter is chosen such that  $\phi_d \approx \phi_d^*$ , the expected misfit, where  $\phi_d^* = N \pm \sqrt{2N}$ , the number of data plus or minus the variance. The data misfit is defined as:

$$\phi_d = M_d(\underline{\mathbf{W}}_d(\mathbf{d} - \mathbf{d}^{obs})), \quad (3.2)$$

where  $M_d$  is Huber's M-measure of the data misfit,  $\underline{\mathbf{W}}_d$  is the weighting matrix applied to the data,  $\mathbf{d}$  is the vector of predicted data, from  $\mathbf{m}$ , and  $\mathbf{d}^{obs}$  is the vector of observed data. The model-structure component is defined as:

$$\phi_m = \alpha_s M_m^s(\underline{\mathbf{W}}_s(\mathbf{m} - \mathbf{m}_s^{ref})) + \alpha_z M_m^z(\underline{\mathbf{W}}_z(\mathbf{m} - \mathbf{m}_z^{ref})), \quad (3.3)$$

where  $\alpha_s$  and  $\alpha_z$  dictate the relative importance of the two terms,  $M_m^s$  and  $M_m^z$  are the Ekblom measures of the model norm,  $\underline{\mathbf{W}}_s$  and  $\underline{\mathbf{W}}_z$  are weighting matrices,  $\mathbf{m}$  is the model vector, and  $\mathbf{m}_s^{ref}$  and  $\mathbf{m}_z^{ref}$  are the reference models. The two terms of  $\phi_m$  with  $s$  and  $z$  subscripts correspond to the “smallest” and “flattest” components, respectively.

Two general measures are used within EM1DTM to determine the “length” of a vector. Huber's M-measure is used as a measure of the data misfit, and is defined as:

$$M_d(x) = \sum_{i=1}^N \rho_H(x_i), \quad (3.4)$$

where

$$\rho_H(x) = \begin{cases} x^2 & |x| \leq c, \\ 2cx - c^2 & |x| > c. \end{cases} \quad (3.5)$$

The parameter  $c$  in Equation 3.5 is defined explicitly by the user within EM1DTM.  $M_d$  will act as a robust measure of misfit when  $c$  is roughly a factor of 2 greater than the average data value.

Eklblom's measure is used to measure the model structure, and is defined as:

$$M_m(x) = \sum_{j=1}^M \rho_E(x_j), \quad (3.6)$$

where

$$\rho_E(x) = (x^2 + \varepsilon^2)^{p/2}. \quad (3.7)$$

The parameters  $p$  and  $\varepsilon$  are defined explicitly within EM1DTM by the user. When a value of  $p = 2$  is assigned, the Eklblom measure behaves like a sum-of-squares measure, producing a fuzzy appearance. If  $p = 1$ , the measure produces a blocky model. The parameter  $\varepsilon$  is a number considerably smaller than the average value within the vector, and is only supplied to prevent numerical difficulties that occur for zero-valued elements when  $p < 2$ . Both  $p$  and  $\varepsilon$  can be specified separately for the smallest and the flattest components of the model structure,  $\phi_m$ . Variables of the previously described equations that are specified by the user are discussed below.

### 3.2.2 Inversion Process

Recently, the time domain electromagnetic 1-D inversion algorithm EM1DTM was developed by UBC Geophysical Inversion Facility (UBC-GIF). The code requires several input files, including a starting model consisting of many more layers than the number of data being inverted, each with a separate conductivity value. This starting model depth-structure is held constant through to the final model, but the conductivity values within each layer are changed to represent the data as the inversion progresses.

The observed TEM data were supplied by Diamondex Resources as \*.RED files that were organized by date, with line number and loop number given in each file (i.e., “14 4 300S 0501W”). However, no information was given on which survey area the data were from; therefore communication with the survey contractor, Frontier Geosciences, was necessary to acquire the survey notes. Some lines of data were recorded more than once, so only the most recently recorded data were considered during this project. The relevant data were reduced to units of  $\mu\text{V}/\text{Am}^2$  for use with EM1DTM.

All TEM inversions were carried out using the EM1DTM algorithm, which requires the input files to be in specific formats. Therefore, the next step was to organize the observed data into the appropriate format. The four required files are the input file, the observation file, the starting model file and the transmitter current waveform (tcw) file.

Many inversion parameters are defined in the main input file, em1dtm.in. This file is responsible for calling the starting conductivity model and the observations, then defining the necessary parameters required to carry out the inversion. These parameters include: the reference conductivity model, the model weights, the Huber and Eklom parameters, the model-structure component coefficients, the inversion type, the trade-off parameter values, the maximum number of iterations, the convergence criterion, the number of Hankel and Fourier kernel evaluations, and the type of output to be given. The reference conductivity model is provided as a single value for the inversions carried out in this study and is set to 0.005 S/m representing a resistive homogeneous half-space, based on Frontier Geosciences' results. The weights were set to “none” because there is no desire to bias the results toward either the smoothest or flattest model. The parameter  $c$  of Huber's M-measure (see Equations 3.4 and 3.5) is kept at 1000 for all inversions. When the value of this parameter is greater than the data, the Huber measure behaves like a sum-of-squares measure, and when  $c$  is less than the data it behaves like a linear measure. In order to avoid generating blocky 1-D models, the Eklom measure (see Equations 3.6 and 3.7) is set to behave like a sum-of-squares measure. This requires setting the parameter

$p = 2$ , while  $\varepsilon = 0.0001$ , for both the smallest and flattest models. Typical values dictating the relative importance for the model-structure components are used for all inversions. The coefficient values are 0.001 and 1, for  $\alpha_s$  and  $\alpha_z$ , respectively. The regularization parameter ( $\beta$ ) is always set to a constant value of 50. This value was chosen because during the inversion it led to the data misfit ( $\phi_d$ ) being less than or equal to the number of data being inverted. The maximum number of iterations allowed during the inversion is set to 20; all soundings converged before reaching this maximum. The default program setting of 0.0001 was kept for the convergence criterion. The default number of Hankel and Fourier kernel evaluations were used because these values are only changed when there are concerns about the accuracy of the Hankel and Fourier transform computations (Farquharson, 2005). Appendix A shows the em1dtm.in file from 1915 0300S.

A file defining the starting conductivity model must be supplied. In this file the user defines the number of layers that make up the model, the individual layer thicknesses and the starting conductivity value for each layer. Prior to creating this model, the user must have some idea of the maximum practical depth to assign to the model. The skin depth is the depth at which the magnetic field reaches  $1/e$  of its original value, and is defined as:

$$\text{skin depth} = 500 \sqrt{\frac{\rho}{f}} \quad (3.8)$$

where  $\rho$  is resistivity and  $f$  is the base frequency. Assuming a constant resistivity value of 50  $\Omega\text{m}$  and the base frequency used in all soundings, 30 Hz, Equation 3.8 yields a skin depth value of 645 m. If a lower resistivity layer exists below the surface, the magnetic field will decay to  $1/e$  at a depth shallower than 645 m (e.g., with a constant resistivity of 5  $\Omega\text{m}$  and a base frequency of 30 Hz, the skin depth value would be only 204 m). Since the layer thicknesses are not varied during the inversion, it is best to have a model with many layers, thus allowing the algorithm to converge on various possible conductivity models that adequately represent the data. The starting model for the final inversions consists of 85 layers with a layer thickness of 0.1

m at the surface, increasing by 0.1 m with each successive layer. The total depth of the starting model is 365 m, a value less than the skin depth, but still comparable with Frontier Geosciences' results. Equal conductivity values (0.02 S/m) are assigned to each layer in the starting model, making the starting model a homogeneous half-space. A portion of a start.layers file is included in Appendix B.

All information relating to the transmitter and receiver loop geometry, several survey parameters and flags, and observed data are included in an observation file. Each sounding has the same format. First, the UTM coordinates and elevation of the transmitter loop centre are defined, along with any notes the user may wish to include. Next, the number of sides for the transmitter loop is specified, and the vertices of the loop are defined in local coordinates, relative to the loop centre. The dipole moment, which is simply a scaling factor in this algorithm, and the receiver geometry are specified on the last line before the data-specifying lines. The recording time, sweep number, observed datum and error are all specified on a single line for each datum of each receiver. Further explanation and an example are provided in Appendix C.

A separate file containing the transmitter current waveform (tcw) is called from the observation file. The turn-off type is the only parameter specified in this file; in this case "step" is used for all soundings.

Once all four input files were complete, the inversions were executed for all soundings of each line. The maximum amount of time required for any inversion was less than 5 minutes, making parameter testing feasible. Testing was carried out to determine the appropriate dipole moment values and error function to apply to the data. A value of 1 was used for the dipole moment, as the data were previously reduced to account for the survey geometry and transmitter current. An error value of 10% was observed to maintain a sufficiently small data misfit without allowing error bars to become very large. For data smaller than  $0.01 \mu\text{V}/\text{Am}^2$ , the minimum error of  $0.001 \mu\text{V}/\text{Am}^2$  was applied in order to prevent the inversion algorithm from overfitting these small data. Once these values were set the data were inverted using EM1DTM as

previously described to generate the final results. These results are presented and discussed in Chapter 5.

## Chapter 4

### SEISMIC REFLECTION RESULTS

The main objective of the seismic reflection portion of this project was to improve upon the final stacked image generated by Frontier Geosciences Inc. by testing various pre-stack and post-stack processing steps on the same observed data. Diamondex Resources Ltd. supplied the observed seismic data for the Lena West property near Lac des Bois. The data were processed entirely using GLOBE *Claritas* with a focus on emphasizing horizontal continuity, or the lack thereof, in the final stacked images.

Seismic line 1 (SL-1) and seismic line 2 (SL-2) were surveyed perpendicular to one another in Area 1915 of the Lena West property (Figure 1.3). Section 3.1.1 described the processing sequence that was applied to the data for both seismic lines. An ensemble of shot gathers and three stacked seismic images are presented and described for each line. Any anomalies within the data and their influence on the processing sequence are also discussed in this chapter, while interpretations are made in Chapter 6.

#### 4.1 Seismic Reflection Line 1

Seismic reflection line 1 (SL-1) consisted of 264 shot gathers, each with 48 traces, covering 1550 m along the ground. The length of the final stack is 1432.5 m, given the split-spread survey geometry (Figure 3.1).

### 4.1.1 Individual Shot Gathers

Most reflections visible in the shot gathers of SL-1 were between 200 ms and 350 ms, and varied from poor to good quality (Figure 4.1). No visible reflections are present in shot gather 1030 (Figure 4.1a), while several reflections are visible in shot gather 1160 between 200 ms and 400 ms (Figure 4.1b). Shot gather 1246 (Figure 4.1c) is taken from the eastern end of the line and illustrates the low frequency energy that dominates the data in shot gathers 1199 through 1264.

### 4.1.2 Stacked Images

The stacked seismic images include all 264 shot gathers being processed in accordance with the processing sequence outlined in Figure 3.2 and described in Section 3.1.1. The stacked images of SL-1 are composed of data from 574 CDPs.

After applying only survey geometry and an initial guessed velocity model for NMO correction, the observed data for SL-1 were stacked in order to produce a brute stack (Figure 4.2). The guessed velocity model consists of velocity values increasing between 400 m/s at the surface and 3000 m/s at the bottom of the section. This stack does not involve any pre-stack or post-stack processing (i.e., filtering, deconvolution, etc.), refraction statics or residual statics. The purposes of generating a brute stack are to ensure the data are where they should be and to get a general idea of where any major features (reflections) exist within the section.

One undulating horizontal reflection is visible near 275 ms across the majority of the stacked image in Figure 4.2. No other significant reflections are clearly visible. The eastern end of the section (CDPs 563 to 673) is dominated by low-frequency noise, possibly caused by low velocity material near the surface or poor receiver-ground coupling along that portion of the line.

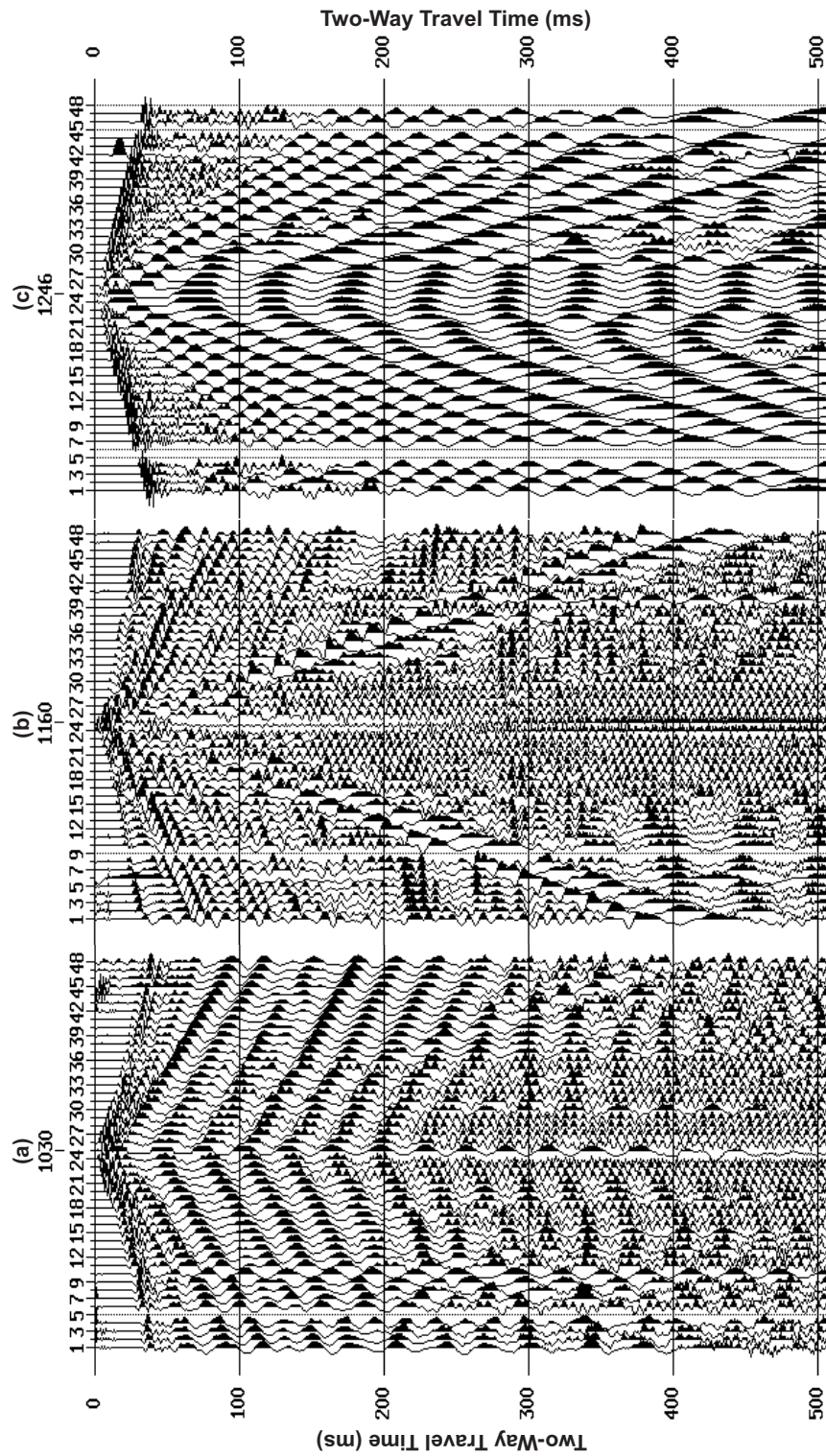


Figure 4.1: Shot gathers 1030, 1160 and 1246 from SL-1 showing: (a) poor reflection visibility, (b) good reflection visibility, (c) low frequency domination. Dead traces were removed prior to including the survey geometry.

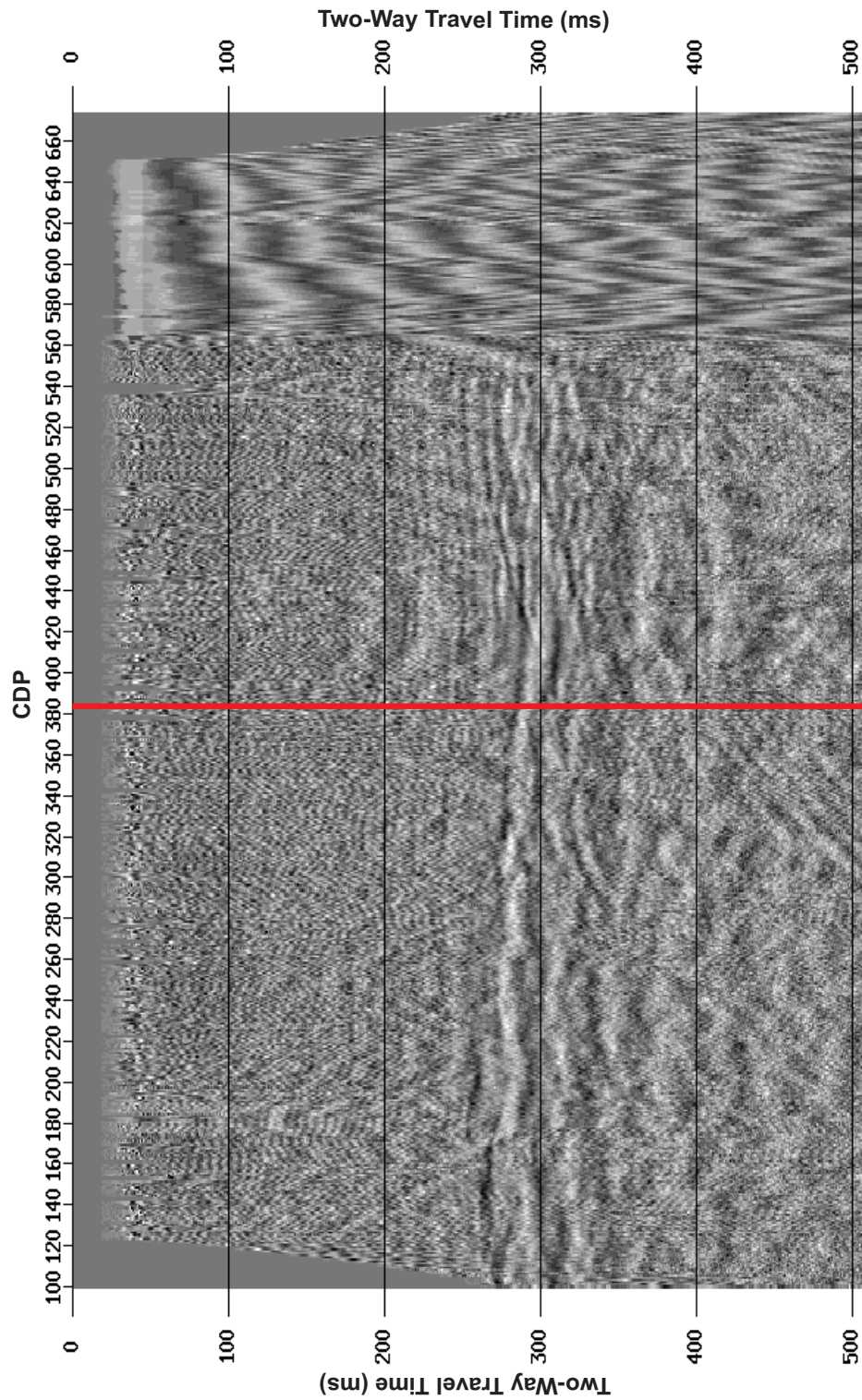


Figure 4.2: A brute stack of observed data for SL-1. Data were stacked without applying any refraction or residual statics, or pre- and post-stack processing and used a guessed NMO correction. Low frequency noise dominates all CDPs greater than 563. The red line shows the location of the intersection with SL-2.

With the application of all pre-stack processing steps including refraction statics, band-pass and  $f-k$  filtering, deconvolution and muting, and a more accurate NMO file designed from a detailed velocity analysis, an intermediate stack was generated and is shown in Figure 4.3. The intermediate stack represents more processing than the final stack generated by Frontier Geosciences.

The main difference between the brute and intermediate stacks for SL-1 is the lack of low frequency dominance in the latter. As a direct result, one continuous reflection becomes clear near 200 ms, while broken reflections become more visible between 250 ms and 330 ms. Band-pass filtering offered the most significant improvement in the stacked image by removing low frequencies that obscured the majority of the previous stacked section, particularly CDPs greater than 563 (see Figure 4.2). However reflections in this CDP range are still unclear in the intermediate stack. The improved NMO correction helped to align reflections, leading to a more laterally continuous stacked image.

Post-stack processing involved residual statics and  $f-x$  deconvolution. These steps significantly improved the stacked image by increasing lateral continuity and removing random noise, respectively. The final stacked image is the result after these processing steps were applied, and is presented in Figure 4.4. The plot above the stacked section is the upper 35 m of the velocity model generated by the refraction statics analysis.

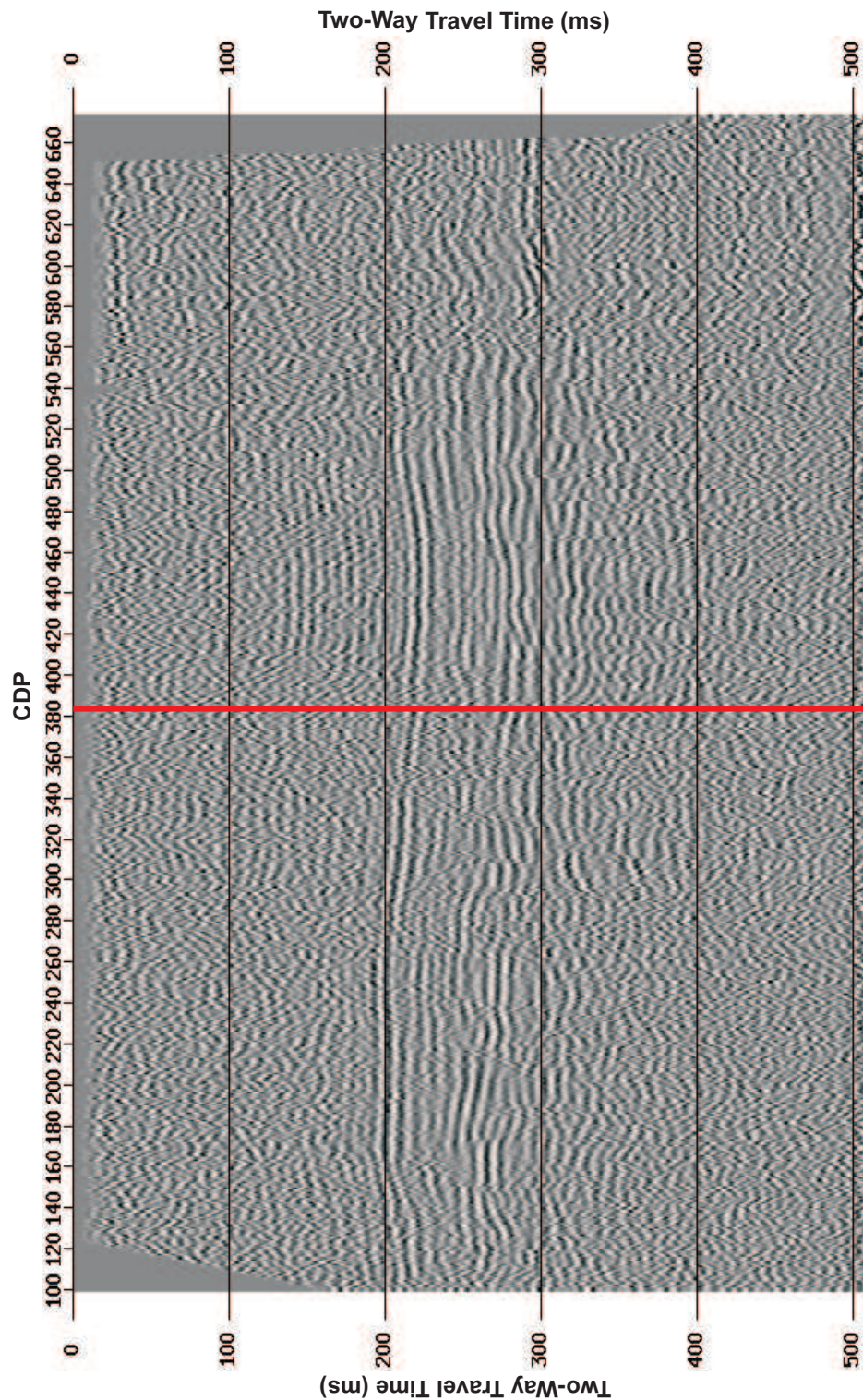


Figure 4.3: An intermediate stack of observed data for SL-1. Data are stacked after the application of refraction statics and all pre-stack processing steps. The NMO correction has been refined by a velocity analysis. The dominance of low frequency noise has been greatly reduced and the main reflections are enhanced. CDPs greater than 563 remain unclear. The red line shows the location of the intersection with SL-2.

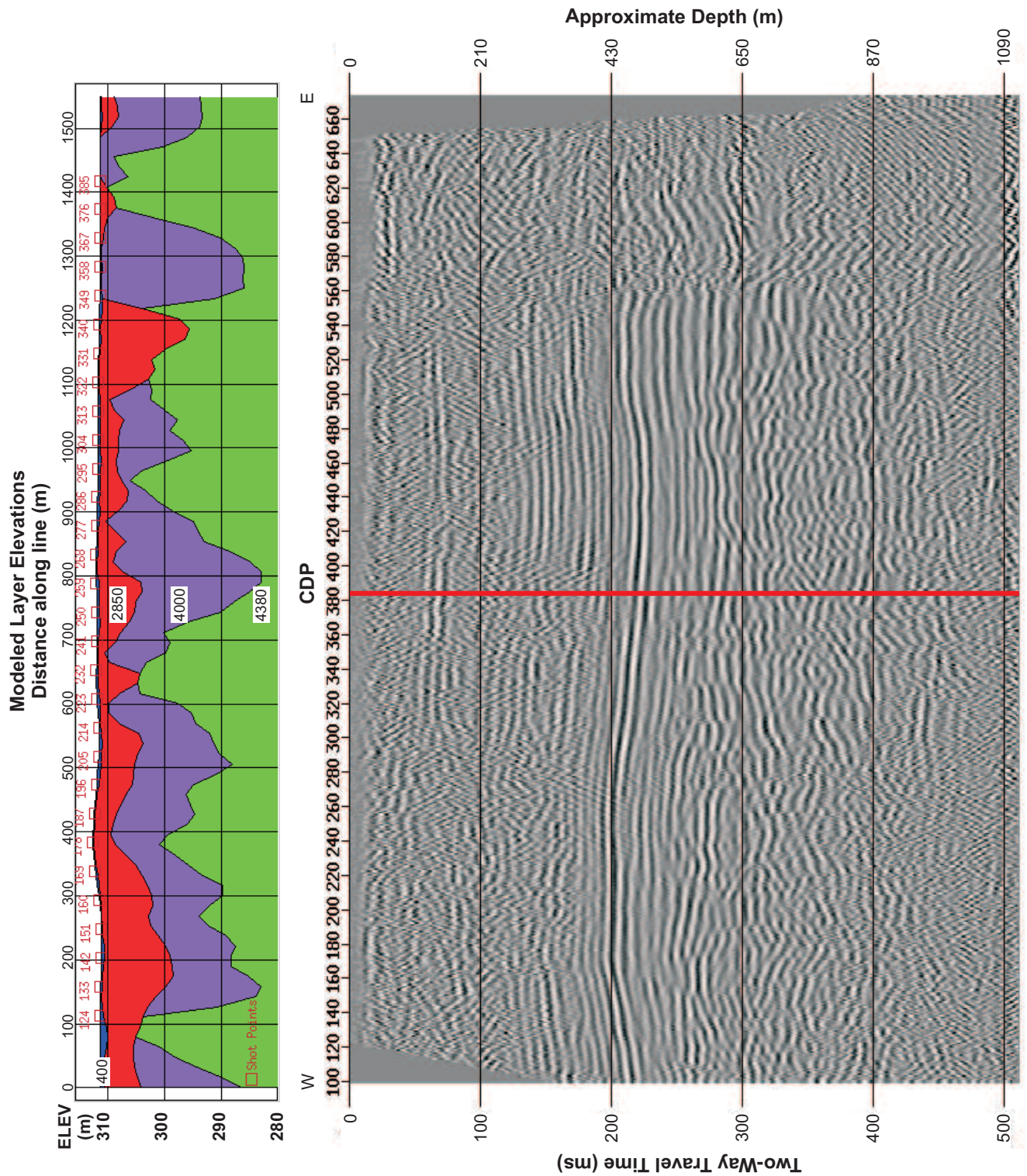


Figure 4.4: The final stack for SL-1. Post-stack processing included residual statics and  $f-x$  deconvolution. The red line shows the location of the intersection with SL-2. Above the main stack is a plot of the refraction statics final velocity model of the upper 35 m. The model includes a thin low velocity layer at the surface, underlain by three layers of increasing velocity. Average velocities for each layer are shown.

The post-stack processing applied to SL-1 greatly enhanced lateral continuity and increased the signal-to-noise ratio of the stacked image, shown in Figure 4.4, over that of the intermediate stack in Figure 4.3. Reflections between 200 ms and 350 ms are clear across the image, barring CDPs greater than 563. The continuous reflection near 200 ms is estimated to have an average depth of  $\sim 440$  m.

## 4.2 Seismic Reflection Line 2

Seismic reflection line 2 (SL-2) was processed in the same manner as SL-1, as described in Section 3.1.1. Seismic line 2 consists of 312 shot gathers, also with 48 receivers each, yielding a 1790 m line length along the surface.

### 4.2.1 Individual Shot Gathers

As with SL-1, most reflections visible in the shot gathers of SL-2 are between 200 ms and 350 ms, and reflections cannot be seen in every shot gather. Figure 4.5 shows three shot gathers illustrating different amounts of reflection clarity: 2045, 2132 and 2135. Shot gather 2045 contains a region between traces 13 and 41 with strong low frequency energy, similar to the eastern end of SL-1. No reflections are visible in shot gather 2045. At least four reflections can be seen in shot gather 2132 between 200 ms and 400 ms, while nothing other than refracted arrivals and ground roll is discernible from the noise in shot gather 2135.

Twenty-four shot gathers (2049 to 2072) contain what appear to be traces on the left mirroring those on the right (Figure 4.6). The point about which the mirroring takes place starts in the centre of shot gather 2049 (between traces 24 and 25) and moves one receiver spacing to the left in each successive shot gather. This effect is shown for shots 2049 and 2059 in Figure 4.6b and 4.6c, and is gone after trace 2072. Shot gather 2048 is also shown in Figure 4.6a to compare a normal gather with the anomalous gathers. The cause of this anomaly is not known;

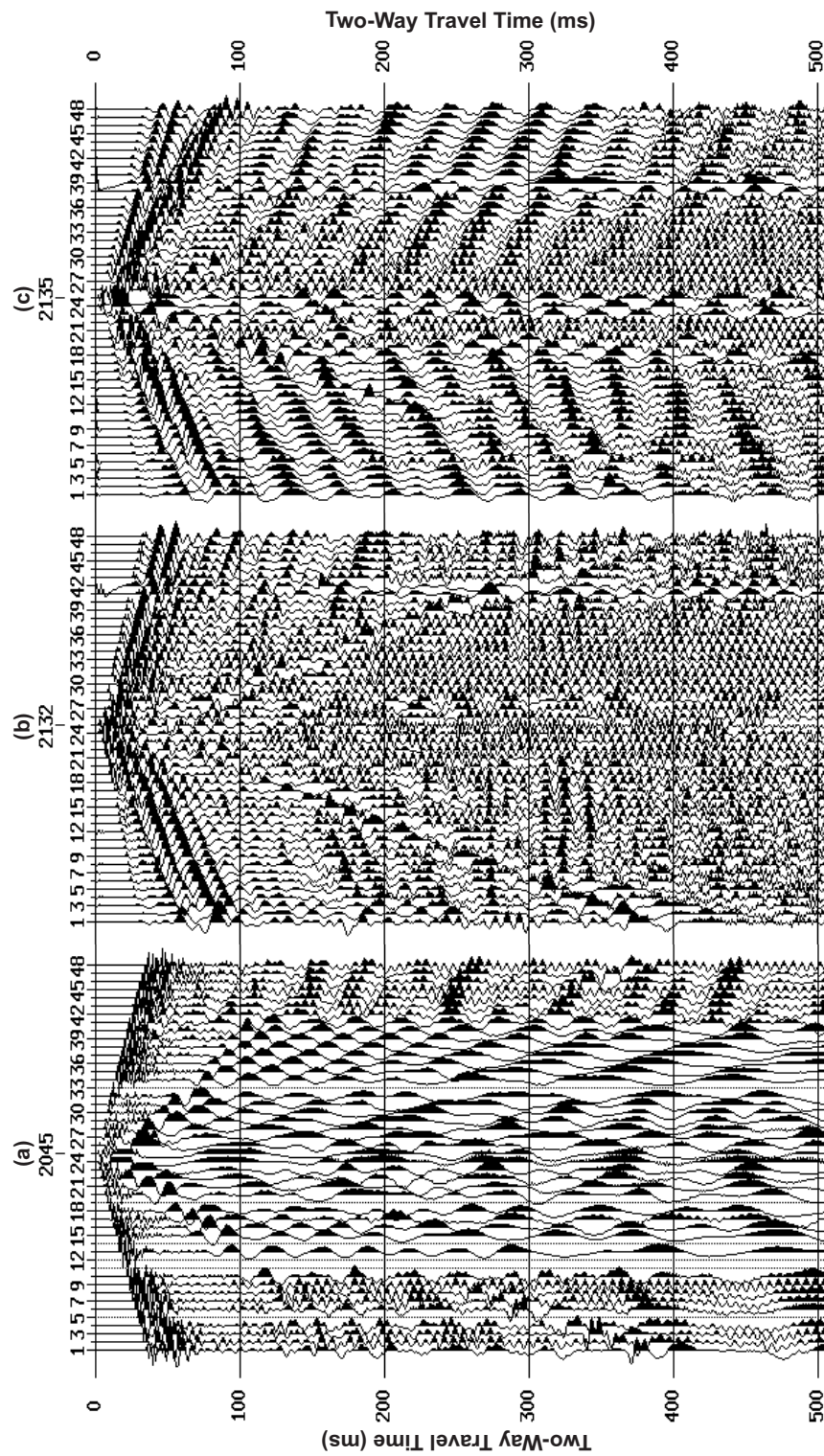


Figure 4.5: Shot gathers 2045, 2132 and 2135 from Seismic Line 2 showing, respectively: (a) a narrow, low frequency dominated region, (b) good reflection visibility, (c) poor reflection visibility. Dead traces were removed prior to including the survey geometry.

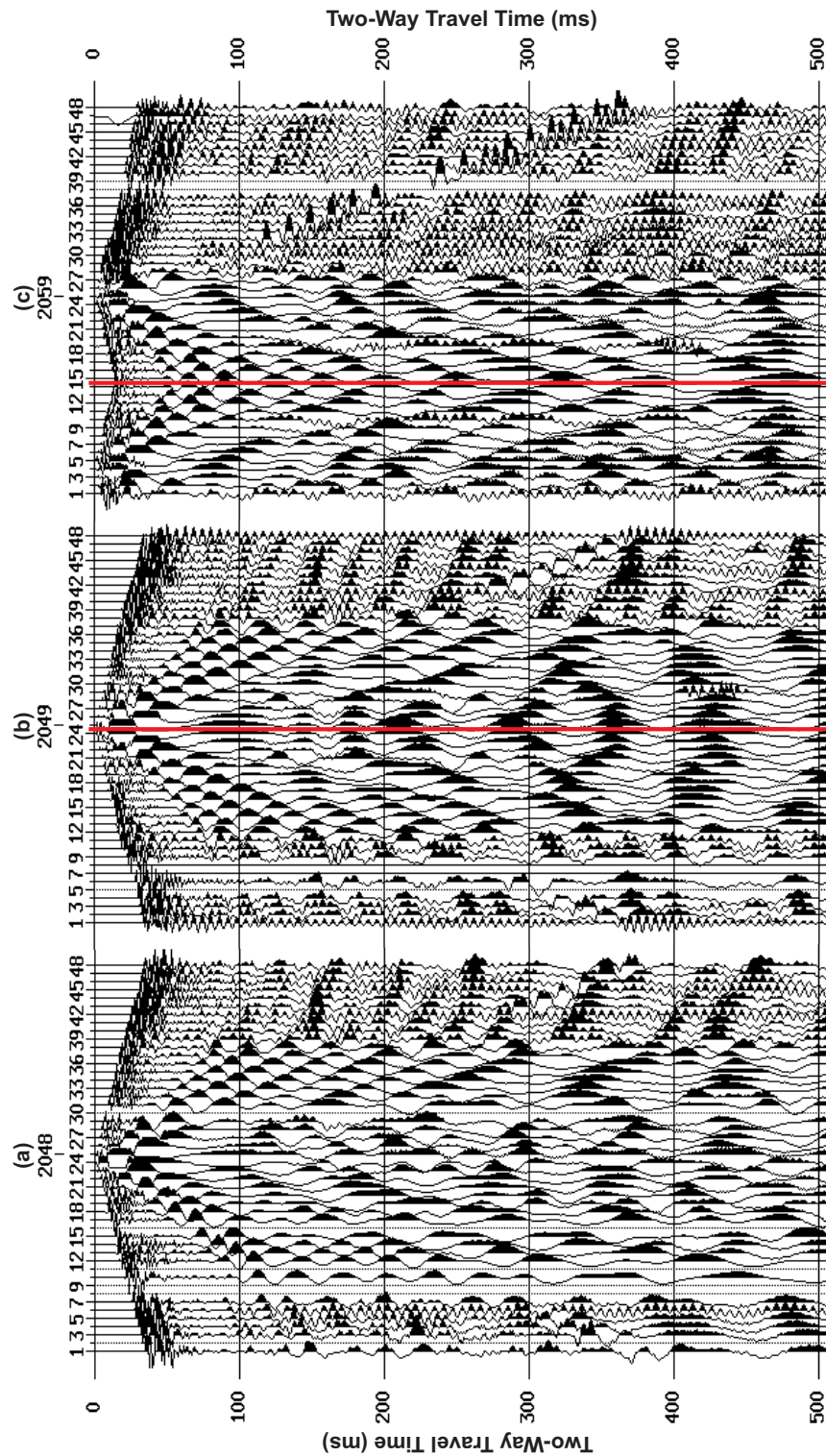


Figure 4.6: The mirroring anomaly in SL-2. Traces equidistant from the mirroring point appear to be identical. (a) Shot gather 2048; one shot prior to mirroring anomaly. (b) Shot gather 2049; mirroring point between traces 24 and 25. (c) Shot gather 2059; mirroring point between traces 14 and 15. The vertical red line on plots (b) and (c) represent the mirroring point; all traces left of this point are a copy of the traces on the right. Dead traces were removed prior to including the survey geometry.

however it may simply have been caused by incorrect wiring or a switch set incorrectly during the survey. Each trace that is the mirror image of another in all 24 shot gathers was deleted before the data were stacked.

#### 4.2.2 Stacked Images

The stacked seismic images for SL-2 include all 312 shot gathers, generating 1672.5 m-wide images consisting of 670 CDPs. The processing sequence for SL-2 is the same as for SL-1 (see Section 3.1.1).

A brute stack of SL-2 is shown in Figure 4.7 and was generated by applying survey geometry and a guessed initial velocity model for NMO correction to the data prior to stacking. The results from the application of pre-stack and post-stack processing steps are described later. A brute stack was again generated to ensure the data are where they should be and to get a general idea of where any major features (reflections) exist within the section.

The main observations made from the brute stack for SL-2 are that there appears to be a low frequency dominated region between CDPs 180 and 250, and that there is a vague horizontal reflection at  $\sim 250$  ms across most of the section. The level of random noise across the section is comparable to that of the SL-1 brute stack.

Pre-stack processing steps, as mentioned in Section 4.1.2 for SL-1 and described in Section 3.1.1, were applied to SL-2. The intermediate stack of SL-2 is shown in Figure 4.8.

The same horizontal reflection seen near 200 ms in the intermediate stack of SL-1 (see Figure 4.3) is present in Figure 4.8, and is continuous across the entire section, barring CDPs 180 to 250. Discontinuous reflections, similar to those found in SL-1, are found between 250 ms and 300 ms.

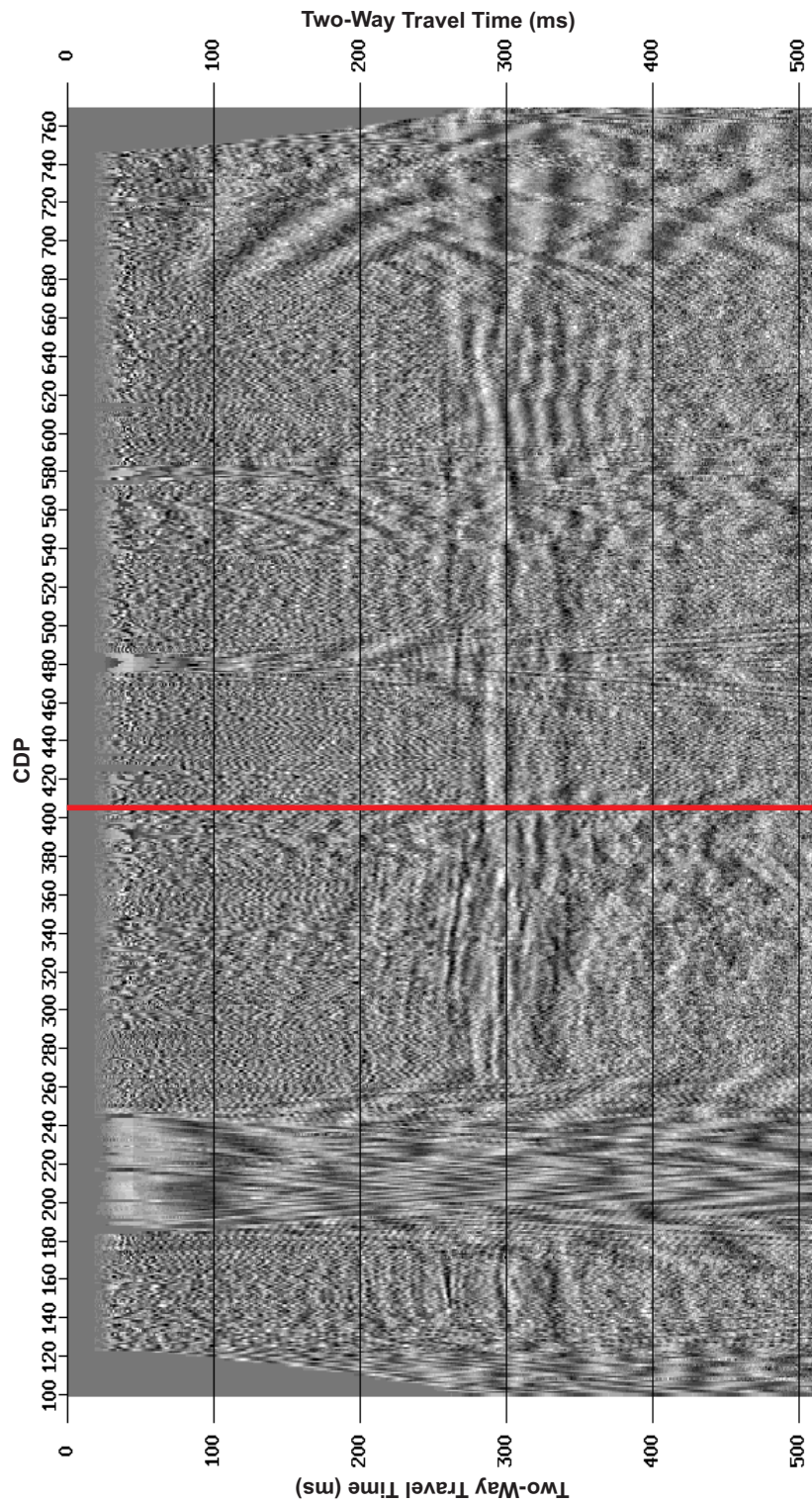


Figure 4.7: A brute stack of observed data for SL-2. Data were stacked without applying any refraction or residual statics, or pre- and post-stack processing and used a guessed NMO correction. Low frequency noise dominates CDPs between 180 and 250. The red line shows the location of the intersection with SL-1.

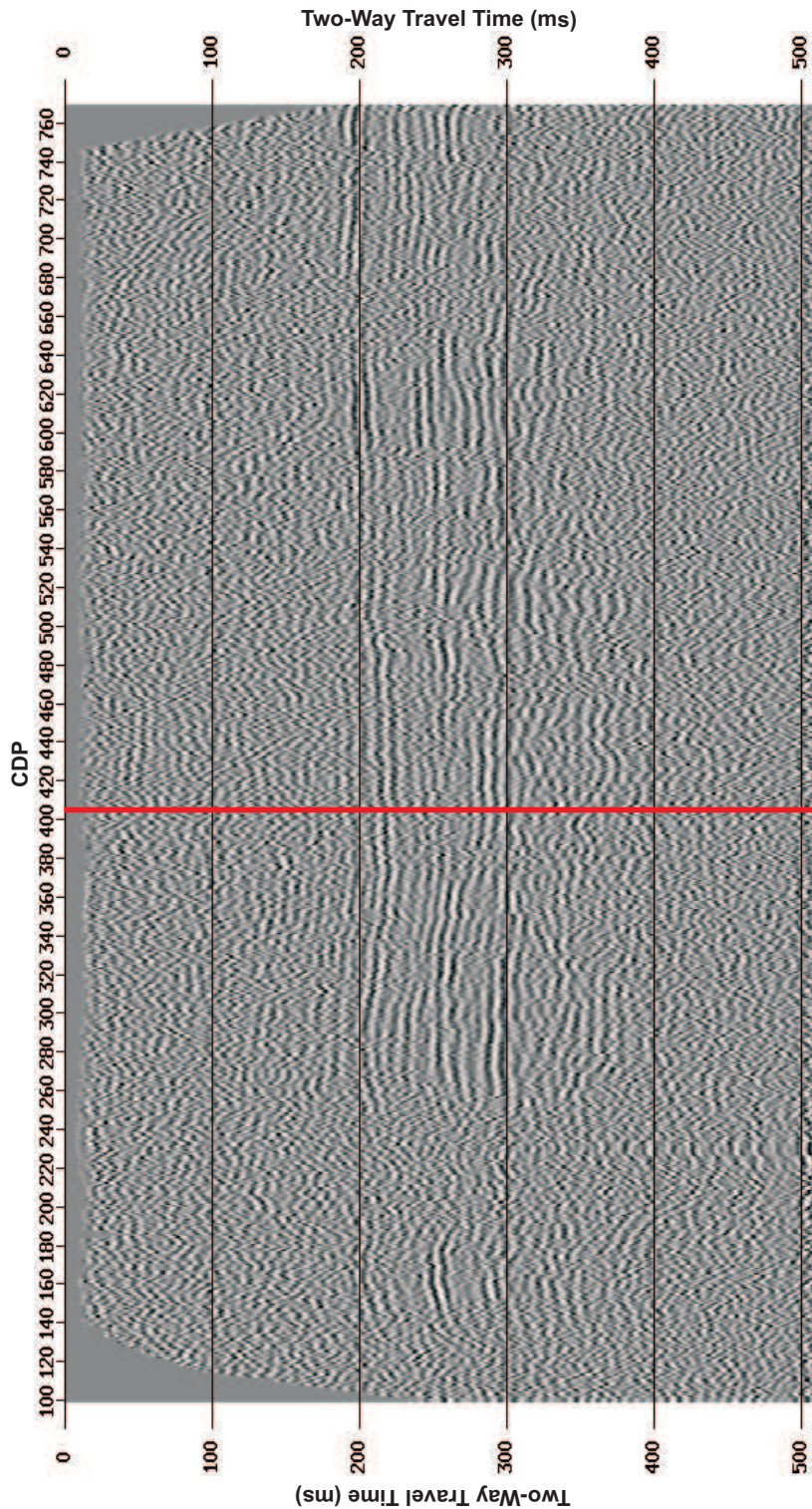


Figure 4.8: An intermediate stack of observed data for SL-2. Data are stacked after the application of refraction statics and all pre-stack processing steps. The NMO correction has been refined by a velocity analysis. The dominance of low frequency noise has been greatly reduced and the main reflections are enhanced. CDPs between 180 and 250 remain unclear. The red line shows the location of the intersection with SL-1.

Post-stack processing for SL-2 involved residual statics and  $f$ - $x$  deconvolution. As with SL-1, these steps significantly improved the lateral continuity and removed random noise throughout the stacked image. The final stacked image is the result after these processing steps were applied, and is presented in Figure 4.9. The plot above the stacked section is the upper 55 m of the velocity model generated by the refraction statics analysis.

The post-stack processing applied to SL-2 improved the lateral continuity and increased the signal-to-noise ratio of the stacked image, shown in Figure 4.9, over the intermediate stack, shown in Figure 4.8. Reflections between 200 ms and 300 ms are clear across the image, with some short reflections visible to 350 ms. CDPs 180 to 250 remain somewhat obscured by noise features that we were not able to remove. The continuous reflection near 200 ms, also visible in SL-1, is estimated to have an average depth of  $\sim 440$  m, indicating an undulating, horizontal reflection extending throughout Area 1915.

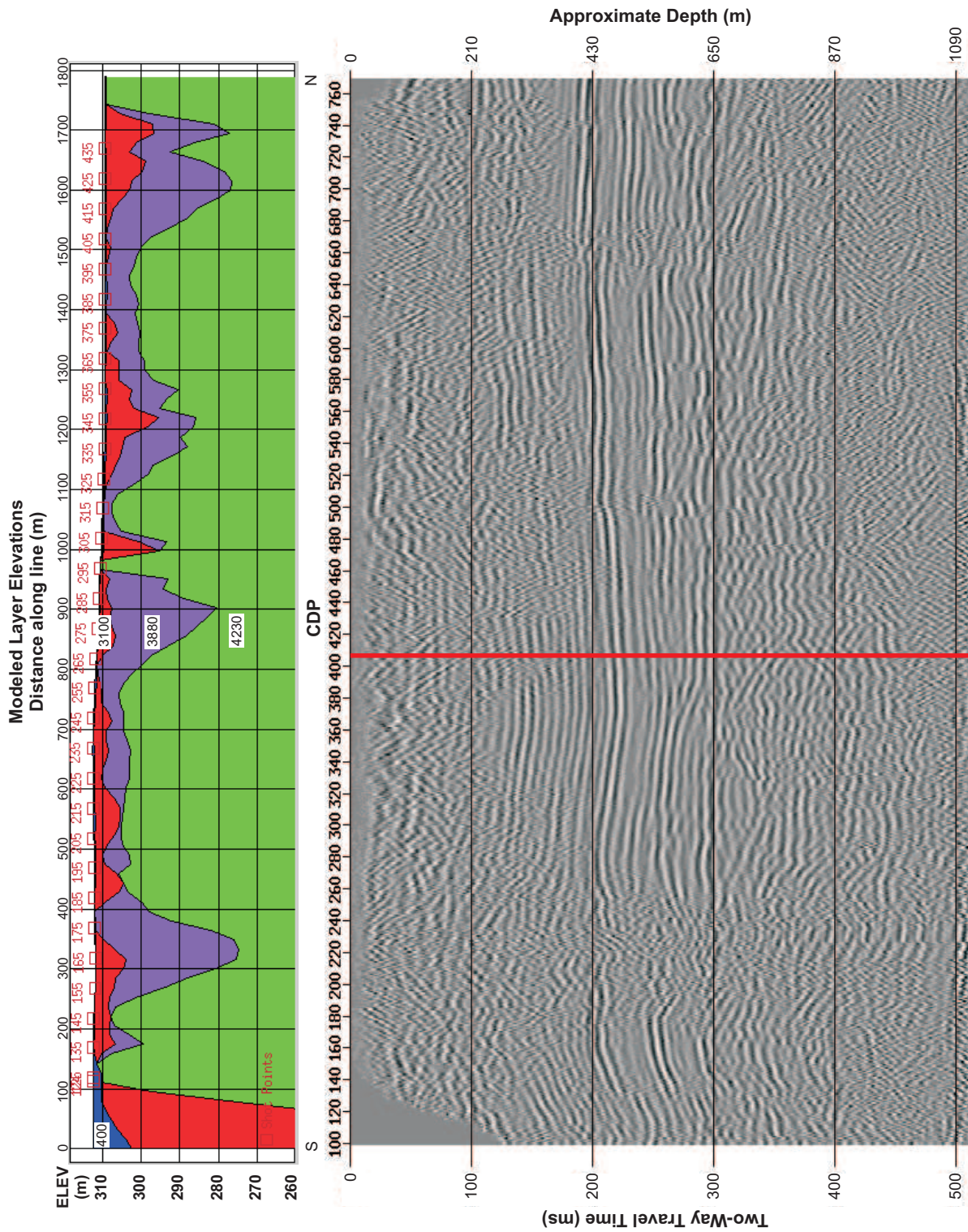


Figure 4.9: The final stack for SL-2. Post-stack processing included residual statics and  $f-x$  deconvolution. The red line shows the location of the intersection with SL-1. Above the main stack is a plot of the refraction statics final velocity model of the upper 55 m. The model includes a thin low velocity layer at the surface, underlain by three layers of increasing velocity. Average velocities for each layer are shown.

## Chapter 5

### TRANSIENT ELECTROMAGNETIC RESULTS

The main objective of the transient electromagnetic (TEM) portion of this study was two-fold: to attempt to better image the subsurface given the same observed data as Frontier Geosciences Inc. by using a different inversion algorithm; and to test the robustness of the EM1DTM inversion code when applied to a real data set. The observed TEM data were supplied by Diamondex Resources Ltd. for the Lena West property near Lac des Bois. During this project the data were inverted using EM1DTM to generate 1-D images of recovered resistivity.

The data from each TEM line underwent the same general processing/inversion sequence. First, the four necessary input files were created using the information available from the raw data and some correspondence with Frontier Geosciences. Next, the data were inverted using EM1DTM to generate a panel of 1-D recovered resistivity models. The 1-D models for each line were then imported into MATLAB and smoothed using a built-in linear interpolation scheme to create a 2-D resistivity-depth section.

The results generated by EM1DTM are in the form of several 1-D resistivity models presented side-by-side using a logarithmic resistivity scale. The interpreted result assumes each 1-D model is valid directly below the centre of the transmitter loop and linearly interpolates between the 1-D models of an individual line, creating a pseudo-2-D resistivity section with a logarithmic resistivity scale. This pseudo-2-D resistivity section is a more realistic image of the subsurface in terms of lateral continuity, as strata typically exhibit smooth lateral continuity without sharp lateral discontinuities at regular intervals. However, this general statement would not apply in areas of significant deformation. Both the 1-D models and the 2-D sections

are presented for each TEM line. Interpretations and comparisons with the previous results are made in Chapter 6.

### 5.1 Transient Electromagnetic Line 0300S

The first set of TEM data to which the EM1DTM algorithm was applied was Line 0300S because the data were already well organized. The data consisted of one base frequency (i.e., one-sweep data) at 30 Hz, with measurements taken in both the x- and z-orientations with the receiver located within and outside each transmitter loop, resulting in four lines of data per sounding. Two inversions were run for this line to determine whether lateral subsurface variations have a significant impact on the results when using a 1-D inversion algorithm. The first inversion used three of the four lines of data for each sounding, the second inversion used only one line of data per sounding. The first three lines of data represent the inner z-orientation, outer z-orientation and outer x-orientation receivers, and offer the most information for each transmitter location. The single receiver in the second inversion is the inner z-orientation receiver, essentially offering information directly below the transmitter. The inner x-orientation receiver is omitted during all inversions because there is no x-component of the electrical field present at the centre of the transmitter when dealing with a 1-D subsurface. The rationale for making this comparison is that if the subsurface truly is 1-D, then the resulting two models should be very similar. If the two models are significantly different, in-line lateral variations are the likely cause of the discrepancy.

The direct output for the two previously described inversions using EM1DTM are shown in Figures 5.1 and 5.2. The results from each sounding are in the form of a 1-D 85-layer resistivity model. As far as EM1DTM is concerned, the final 1-D models have no lateral physical significance. However, the centres of each loop are 200 m apart. All six soundings are presented next to one another, creating a 1200 metre-wide pseudo-2-D resistivity profile.

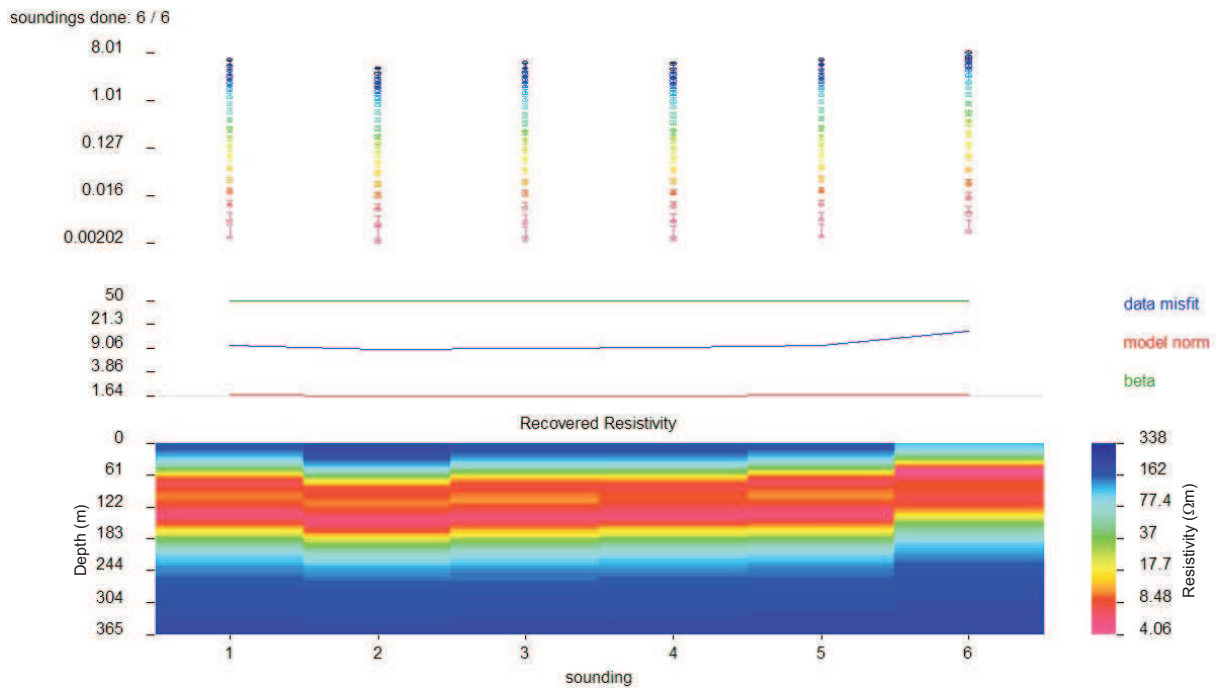


Figure 5.1: Recovered resistivity output from EM1DTM for one-receiver data of TEM Line 0300S in Area 1915 using a homogeneous half-space reference model of 0.005 S/m (200  $\Omega\text{m}$ ). All six soundings converged to generate six 1-D models. Each model is displayed as 200 m wide and the total line length is 1200 m (lower panel). Final values for  $\phi_d$ ,  $\phi_m$  and  $\beta$  are shown above the model as blue, red and green lines, respectively. In the upper panel, error bars represent the observed data and their associated error, while the circles represent the predicted data. All data are in units of  $\mu\text{V}/\text{Am}^2$

The resistivity models corresponding with the inner z-orientation receiver data (Figure 5.1) consistently show a structure of higher resistivity for the upper 30 m to 60 m, overlying a  $\sim 100$  m thick low resistivity layer. Below this appears to be another higher resistivity region. Resistivity values range between 4.06  $\Omega\text{m}$  and 338  $\Omega\text{m}$  within the six models. All soundings have a final  $\phi_d$  approximately equal to or less than the number of data (20).

The resistivity models corresponding to the inversion of the data using three receivers per sounding are shown in Figure 5.2. The structure of the models is inconsistent along the line with the exception of the higher resistivity layer between the surface and 30 m to 60 m depth. The resistivity values vary between 0.0457  $\Omega\text{m}$  and 947  $\Omega\text{m}$  within the six models, a much larger

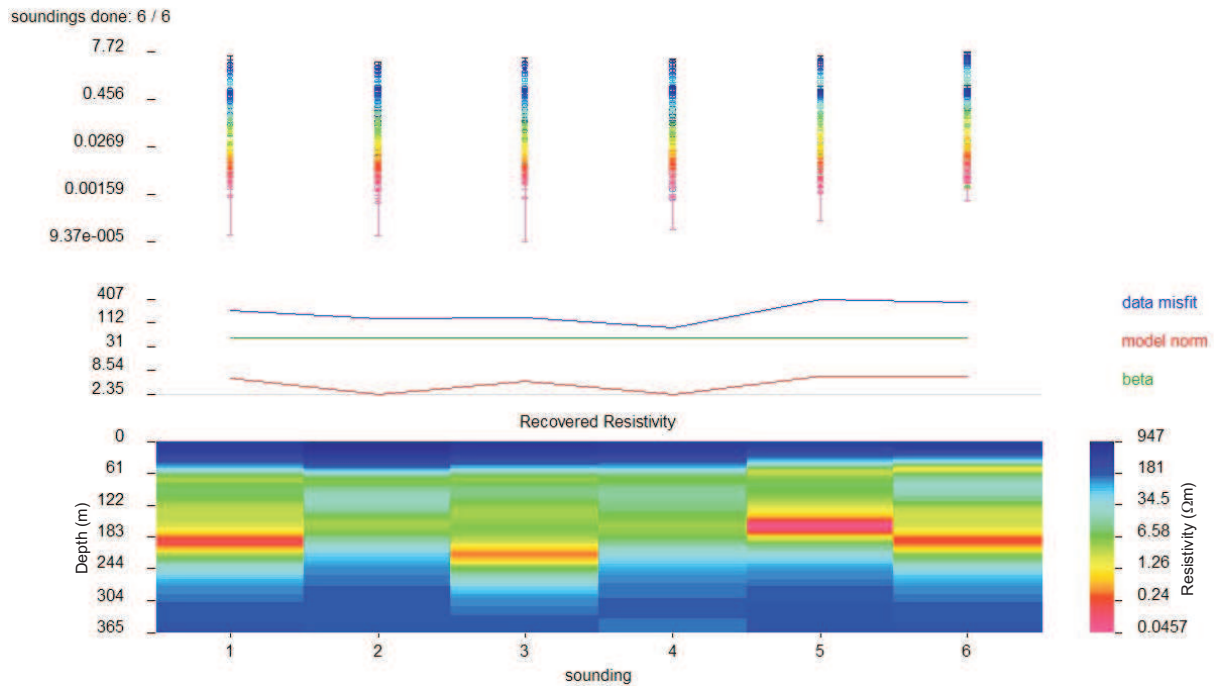


Figure 5.2: Recovered resistivity output from EM1DTM for three-receiver data of TEM Line 0300S in Area 1915 using a homogeneous half-space reference model of 0.005 S/m ( $200 \Omega\text{m}$ ). All six soundings converged to generate six 1-D models. Each model is displayed as 200 m wide and the total line length is 1200 m (lower panel). Final values for  $\phi_d$ ,  $\phi_m$  and  $\beta$  are shown above the model as blue, red and green lines, respectively. In the upper panel, error bars represent the observed data and their associated error, while the circles represent the predicted data. All data are in units of  $\mu\text{V}/\text{Am}^2$

range than observed in the previous models (Figure 5.1). Final  $\phi_d$  values for the soundings of this inversion are roughly two orders of magnitude higher than those of the previous models, indicating a high data misfit (middle panel, Figure 5.2). The cause of this high data misfit is likely due to the disagreement during inversion between the data from the different receivers, as the data represent a 3-D subsurface, and the algorithm is trying to solve for a 1-D model. This indicates that lateral variations in resistivity structure along the line are present on the scale of the transmitter loop. The wide range in resistivity values, along with the lateral inconsistency between adjacent models and the high data misfit indicate a poor inversion result due to 3-D

subsurface structure. To generate the most realistic 1-D resistivity models and avoid the effects of 3-D subsurface variations on the 1-D inversion procedure, subsequent inversions will only include data from the inner z-orientation receiver and ignore data from the outer z- and x-orientation receivers.

In the previous two figures, a high resistivity ( $\sim 200 \Omega\text{m}$ ) region appears to underlie the low resistivity layer to the bottom of the model. However, when inverting the data using a homogeneous half-space reference model of  $0.2 \text{ S/m}$  ( $5 \Omega\text{m}$ ) instead of  $0.005 \text{ S/m}$  ( $200 \Omega\text{m}$ ), the high resistivity region near the bottom of the models does not appear; instead, the low resistivity ( $\sim 5 \Omega\text{m}$ ) layer extends to depth. This alternative result is shown in Figure 5.3. As the upper  $\sim 150 \text{ m}$  of the section is similar to that in Figure 5.1, it is likely that this resistivity structure is a reasonable representation of the subsurface. However, as the inversion result is defaulting to the reference model below  $\sim 150 \text{ m}$ , the inversion is not “seeing” below this depth and a true thickness of the low resistivity layer cannot be determined from the given data. The reader should be aware that the inversion results for the other lines in Area 1915 are presented using a reference model of  $0.005 \text{ S/m}$ , and that resistivity contrasts below  $\sim 150 \text{ m}$  are not assumed to be reliable.

Using the previously mentioned linear interpolation scheme within MATLAB, the 1-D models were smoothed together to create a 2-D resistivity section, shown in Figure 5.4(b). Plot (a) in Figure 5.4 is the 1-D model output from EM1DTM, while plots (c) and (d) present the details of soundings 6 and 2, respectively, including the observed (with error bars) and predicted (circles) data, the final values for  $\phi_d$ ,  $\phi_m$  and  $\beta$ , the number of data and the sounding location. Soundings 6 and 2 represent the highest and lowest data misfit of the 1-D models for Line 0300S, respectively. Because the colour scale for the smooth model is slightly different than that for the EM1DTM output, areas of low resistivity ( $\leq 7 \Omega\text{m}$ ) appear slightly brighter in the smooth model. Both plots highlight the same resistivity structure: high resistivity material overlying a low resistivity layer, with the depth-to-interface being shallower at the ends of the line. The

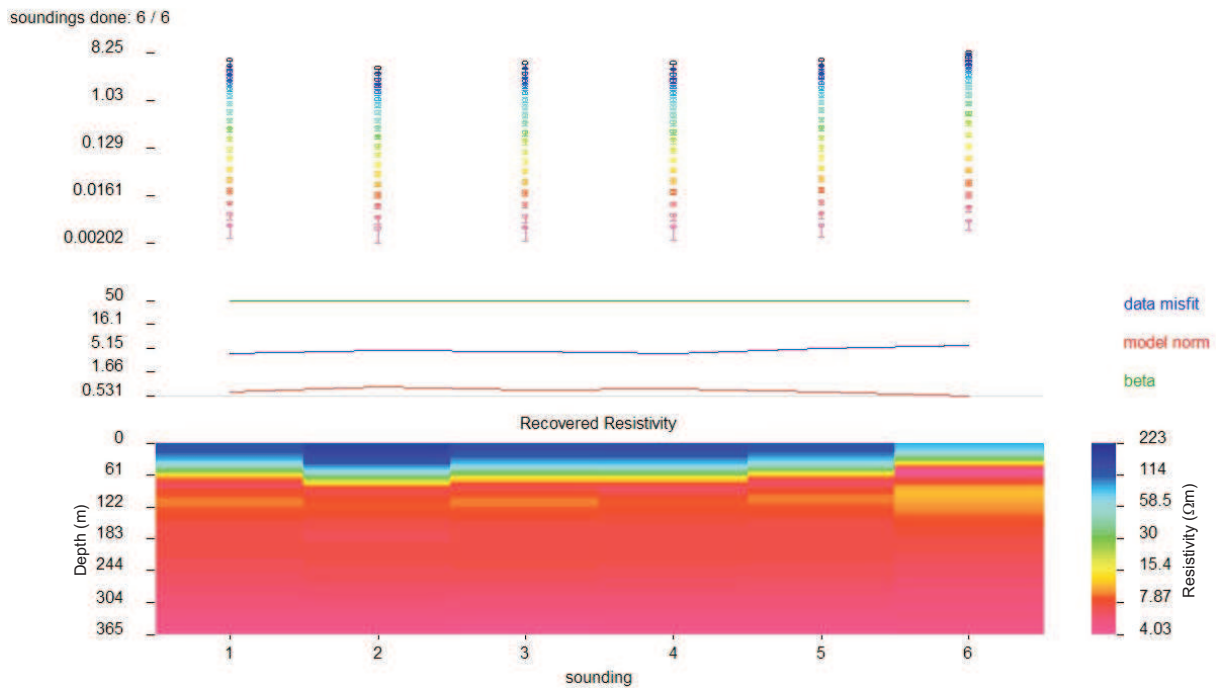


Figure 5.3: Recovered resistivity output from EM1DTM for one-receiver data of TEM Line 0300S in Area 1915 using a homogeneous half-space reference model of 0.2 S/m ( $5 \Omega\text{m}$ ). All six soundings converged to generate six 1-D models. Each model is displayed as 200 m wide and the total line length is 1200 m (lower panel). Final values for  $\phi_d$ ,  $\phi_m$  and  $\beta$  are shown above the model as blue, red and green lines, respectively. In the upper panel, error bars represent the observed data and their associated error, while the circles represent the predicted data. All data are in units of  $\mu\text{V}/\text{Am}^2$

low resistivity layer appears to contain two peaks of low resistivity split by a slightly higher resistivity trough (Figure 5.4(c) and (d)). The plot of observed and predicted data for soundings 6 and 2 show that the final models adequately reproduce the data, while the maximum data misfit is indicated to be sufficiently small.

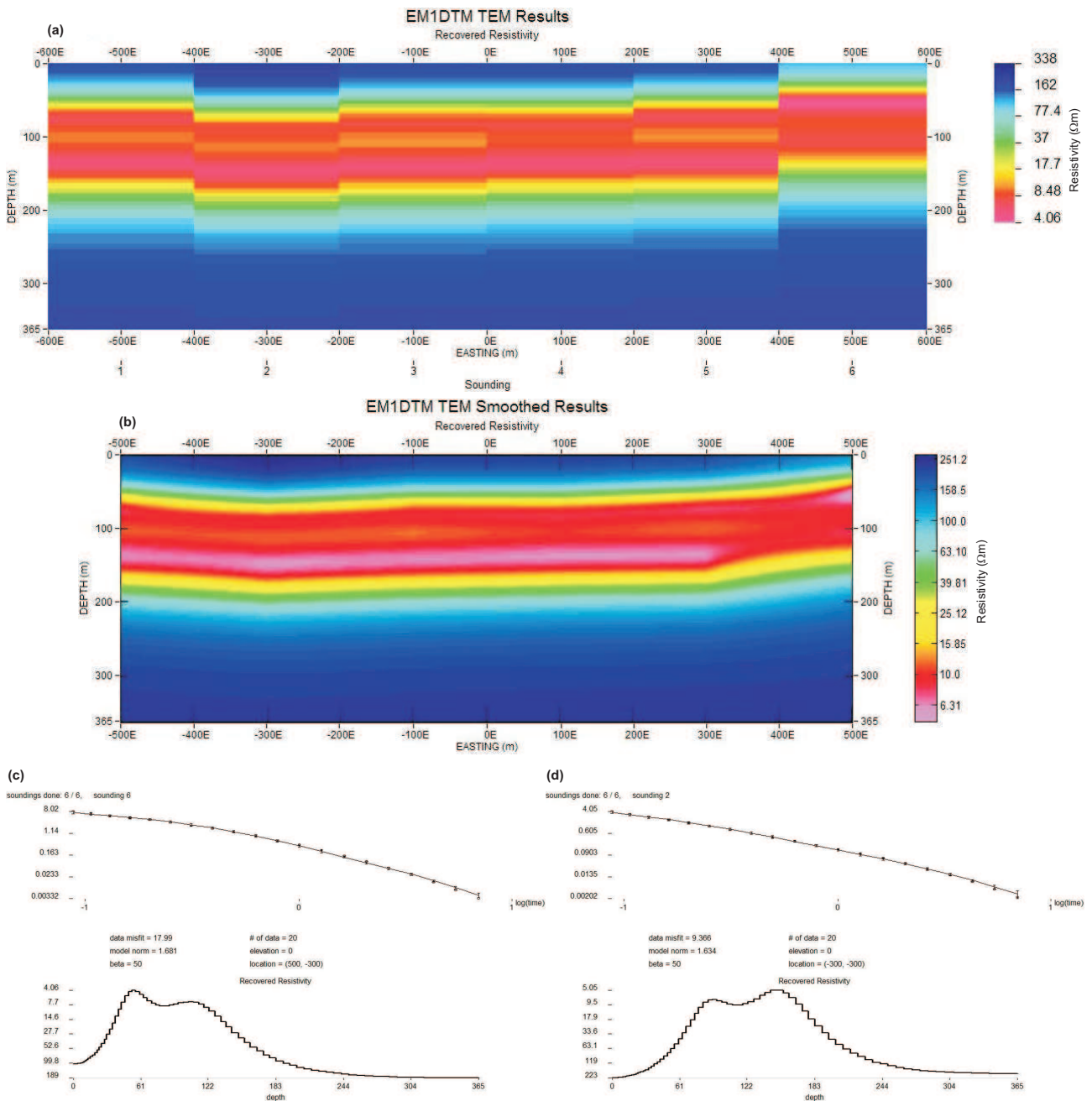


Figure 5.4: TEM inversion results from Line 0300S in Area 1915. (a) EM1DTM results; (b) smoothed EM1DTM results from MATLAB; (c) and (d) present the observed (with error bars) and predicted data (circles) plotted as  $\mu\text{V}/\text{Am}^2$  vs  $\log(\text{time})$  in the upper panel, final values for  $\phi_d$ ,  $\phi_m$ ,  $\beta$ , the number of data, elevation and location in the centre, and the resistivity variation with depth in the lower panel for the individual soundings with the highest and lowest data misfits for Line 0300S, soundings 6 and 2, respectively.

## 5.2 Transient Electromagnetic Line 0100S

Line 0100S consists of the most data collected for a single line in Area 1915. Data were collected at five base frequencies; however, to be consistent with the adjacent two lines, only those data collected at the 30 Hz base frequency were used. As previously mentioned, to create the most realistic 1-D resistivity models the only data inverted were those collected from the inner z-orientation receiver.

The EM1DTM output for Line 0100S is shown in Figure 5.5. The loops for Line 0100S are 200 m apart. All seven 1-D soundings are presented next to one another, creating a 1400 metre-wide pseudo-2-D resistivity profile.

The resistivity models corresponding with the inner z-orientation receiver data (Figure 5.5) show a structure of higher resistivity for the upper 30 m to 80 m, overlying a  $\sim 100$  m thick low resistivity layer. Below this appears to be another higher resistivity region; a result of the inversion defaulting to the reference model. Lateral variation is more apparent in this line than in Line 0300S. The thickness of the resistive upper layer appears to undulate across the line, with a maximum thickness of  $\sim 80$  m at -500E and a minimum thickness of  $\sim 30$  m at 500E. Resistivity values range between  $4.06 \Omega\text{m}$  and  $338 \Omega\text{m}$  within the seven models. All soundings have a final  $\phi_d$  approximately equal to or less than the number of data (20).

Using MATLAB, the 1-D models were smoothed together to create a 2-D resistivity section, shown in Figure 5.6(b). Plot (a) in Figure 5.6 is the 1-D model output from EM1DTM, while plots (c) and (d) present the details of soundings 5 and 3, respectively, including the observed (with error bars) and predicted (circles) data, the final values for  $\phi_d$ ,  $\phi_m$  and  $\beta$ , the number of data and the sounding location. Soundings 5 and 3 represent the highest and lowest data misfit of the 1-D models for Line 0100S, respectively. Plots (a) and (b) highlight the same resistivity structure: high resistivity material overlying a low resistivity layer, with the depth-to-interface

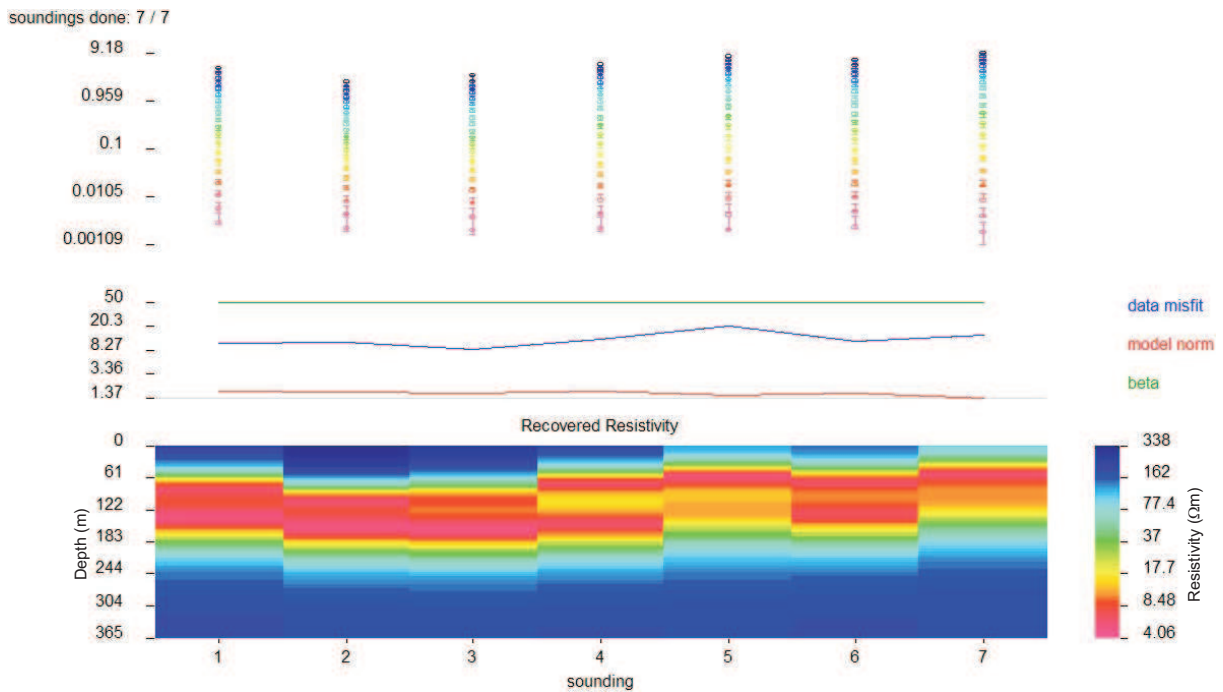


Figure 5.5: Recovered resistivity output from EM1DTM for one-receiver data of TEM Line 0100S in Area 1915 using a homogeneous half-space reference model of 0.005 S/m (200  $\Omega$ m). All seven soundings converged to generate seven 1-D models. Each model is displayed as 200 m wide and the total line length is 1400 m (lower panel). Final values for  $\phi_d$ ,  $\phi_m$  and  $\beta$  are shown above the model as blue, red and green lines, respectively. In the upper panel, error bars represent the observed data and their associated error, while the circles represent the predicted data. All data are in units of  $\mu\text{V}/\text{Am}^2$

being shallower at the eastern end of the line and some undulation along the line. The low resistivity layer appears to contain two peaks of low resistivity split by a slightly higher resistivity trough (Figure 5.6(c) and (d)). The plot of observed and predicted data for soundings 5 and 3 show that the final models adequately reproduce the data, while the maximum data misfit is indicated to be sufficiently small.

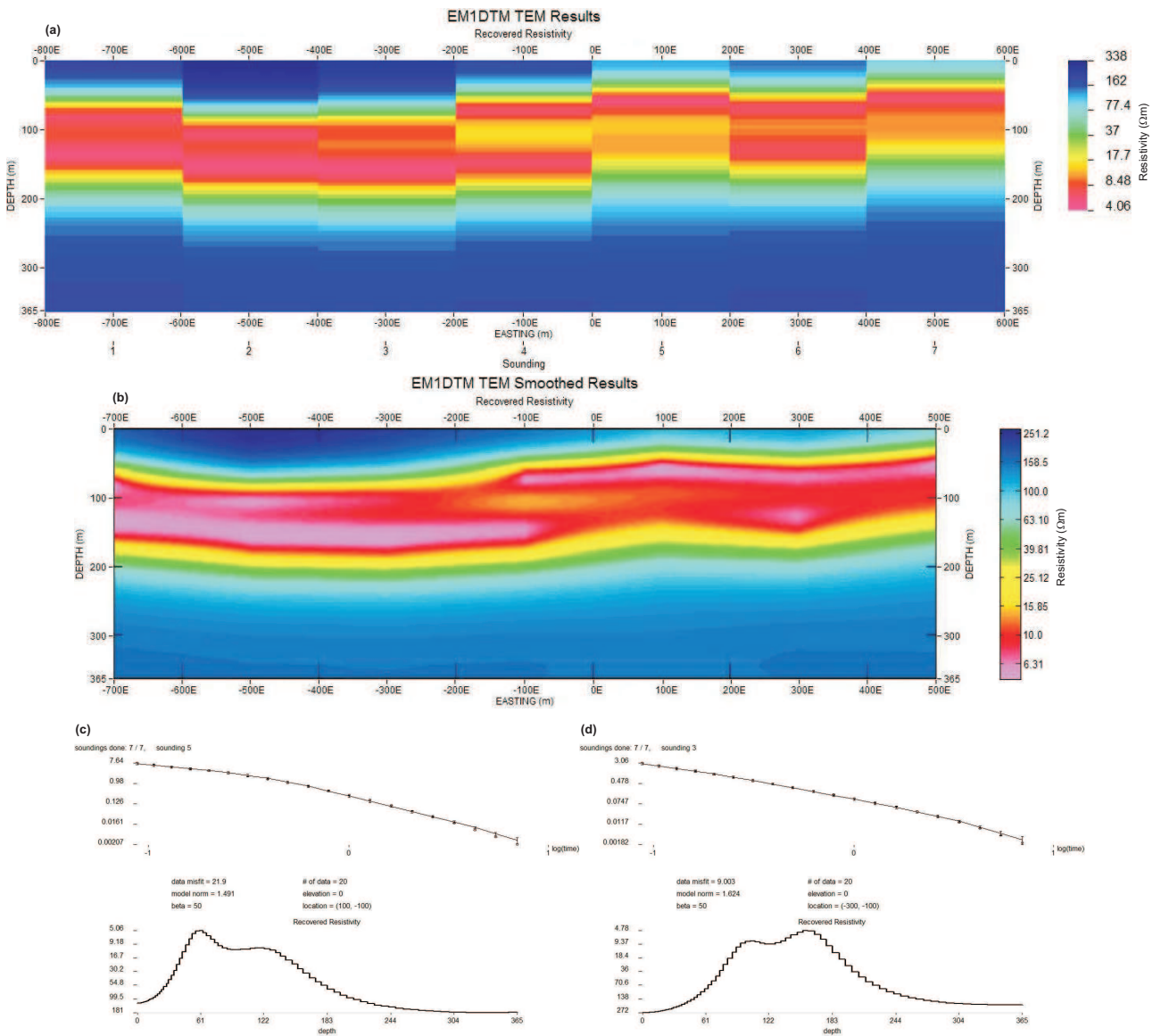


Figure 5.6: TEM inversion results from Line 0100S in Area 1915. (a) EM1DTM results; (b) smoothed EM1DTM results from MATLAB; (c) and (d) present the observed (with error bars) and predicted data (circles) plotted as  $\mu\text{V}/\text{Am}^2$  vs  $\log(\text{time})$  in the upper panel, final values for  $\phi_d$ ,  $\phi_m$ ,  $\beta$ , the number of data, elevation and location in the centre, and the resistivity variation with depth in the lower panel for the individual soundings with the highest and lowest data misfits for Line 0100S, soundings 5 and 3, respectively.

### 5.3 Transient Electromagnetic Line 0100N

As with Line 0300S, data were collected at two receiver locations and two receiver orientations at a base frequency of 30 Hz. However, because the data collected using the outer receivers represent a 3-D subsurface, and the inner x-orientation receiver offers no information due to the survey geometry, only the data from the inner z-orientation receiver were used.

The EM1DTM output for Line 0100N is shown in Figure 5.7. The transmitter loop spacing for Line 0100N is 200 m. All six 1-D soundings are presented next to one another, creating a 1200 metre-wide pseudo-2-D resistivity profile.

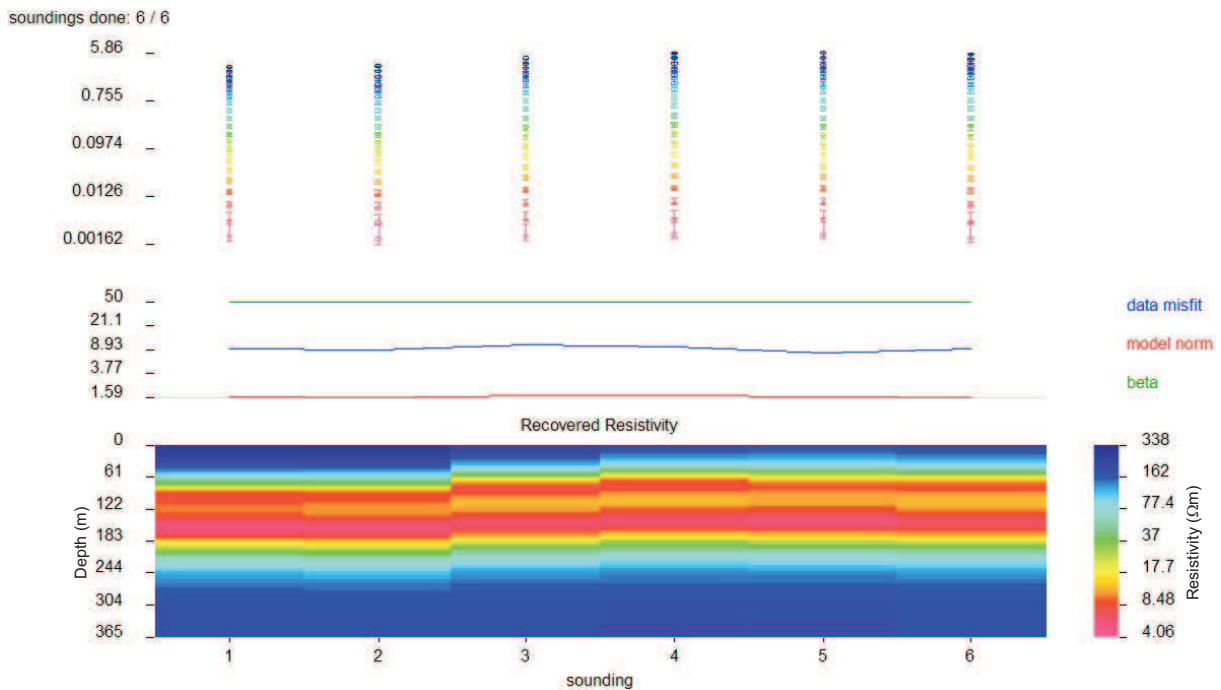


Figure 5.7: Recovered resistivity output from EM1DTM for one-receiver data of TEM Line 0100N in Area 1915 using a homogeneous half-space reference model of 0.005 S/m (200 Ωm). All six soundings converged to generate six 1-D models. Each model is displayed as 200 m wide and the total line length is 1200 m (lower panel). Final values for  $\phi_d$ ,  $\phi_m$  and  $\beta$  are shown above the model as blue, red and green lines, respectively. In the upper panel, error bars represent the observed data and their associated error, while the circles represent the predicted data. All data are in units of  $\mu\text{V}/\text{Am}^2$

The resistivity models corresponding with the inner z-orientation receiver data (Figure 5.7) show a structure of higher resistivity for the upper 50 m to 70 m, overlying a  $\sim 100$  m thick low resistivity layer. Below this low resistivity layer appears to be a region of higher resistivity; a result of the inversion defaulting to the reference model. Lateral variation is minimal in Line 0100N, with the thickness of the resistive upper layer being only  $\sim 20$  m thinner at 100E than at -300E where it is thickest. Resistivity values range between  $4.06 \Omega\text{m}$  and  $338 \Omega\text{m}$  within the six models. All soundings have a final  $\phi_d$  approximately equal to or less than the number of data (20).

A linearly interpolated smooth 2-D resistivity section of the 1-D models in Figure 5.7 was generated using MATLAB and is shown in Figure 5.8(b). Plot (a) in Figure 5.8 is the 1-D model output from EM1DTM, while plots (c) and (d) present the details of soundings 3 and 5, respectively, including the observed (with error bars) and predicted (circles) data, the final values for  $\phi_d$ ,  $\phi_m$  and  $\beta$ , the number of data and the sounding location. Soundings 3 and 5 represent the highest and lowest data misfit of the 1-D models for Line 0100N, respectively. Plots (a) and (b) highlight the same resistivity structure: high resistivity material overlying a low resistivity layer, with the depth-to-interface being slightly shallower east of -100E than the western third of the line. The low resistivity layer appears to contain two peaks of low resistivity split by a slightly higher resistivity trough (Figure 5.8(c) and (d)). The plot of observed and predicted data for soundings 3 and 5 show that the final models adequately reproduce the data, while the maximum data misfit is indicated to be sufficiently small.

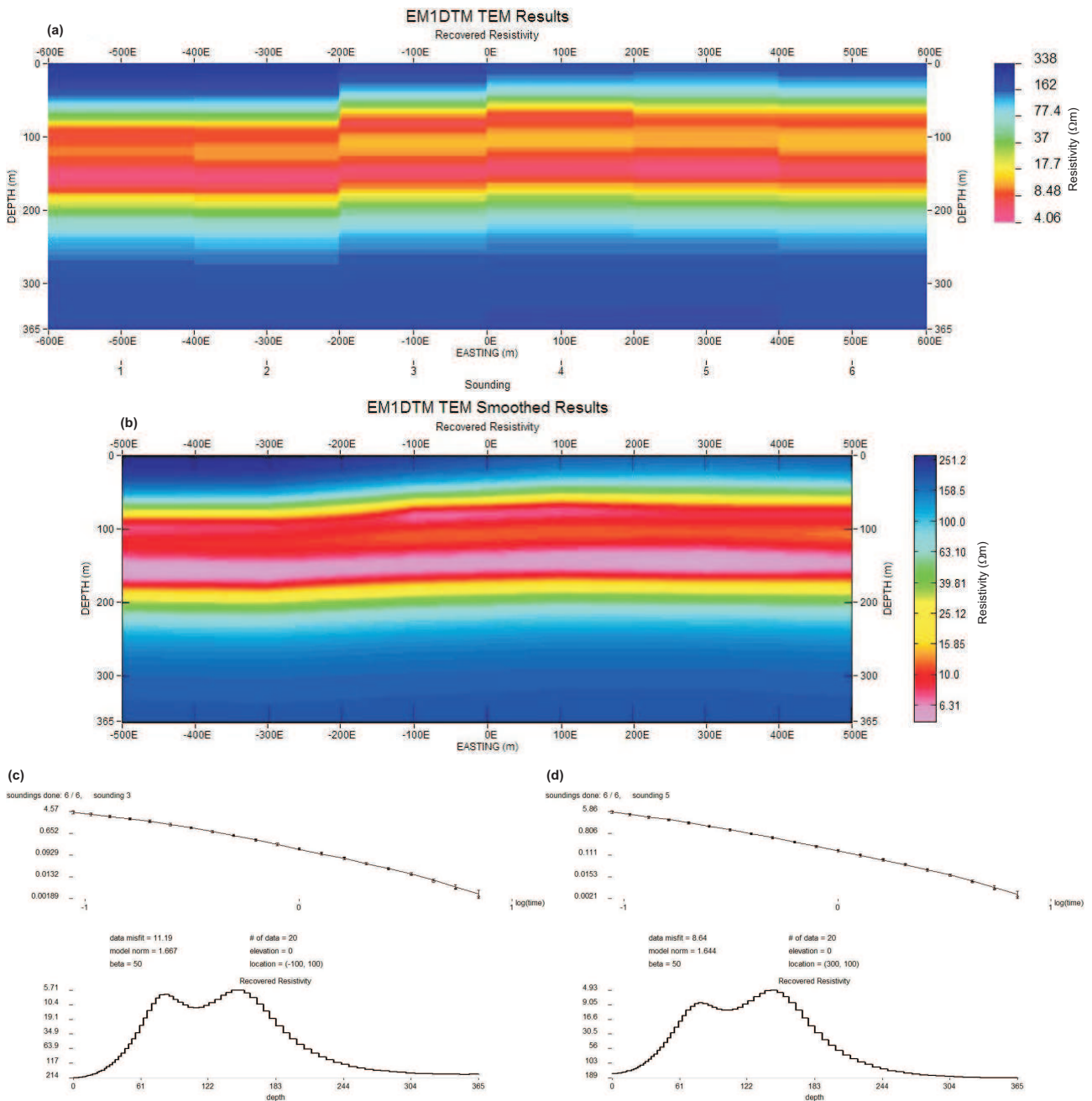


Figure 5.8: TEM inversion results from Line 0100N in Area 1915. (a) EM1DTM results; (b) smoothed EM1DTM results from MATLAB; (c) and (d) present the observed (with error bars) and predicted data (circles) plotted as  $\mu\text{V}/\text{Am}^2$  vs  $\log(\text{time})$  in the upper panel, final values for  $\phi_d$ ,  $\phi_m$ ,  $\beta$ , the number of data, elevation and location in the centre, and the resistivity variation with depth in the lower panel for the individual soundings with the highest and lowest data misfits for Line 0100N, soundings 3 and 5, respectively.

## Chapter 6

### DISCUSSION

During this study of Area 1915 of the Lena West property near Lac des Bois, the seismic reflection and transient electromagnetic (TEM) data were processed and inverted using GLOBE *Claritas* and EM1DTM, respectively. The results from processing both seismic lines indicate a continuous undulating layer  $\sim 440$  m below the surface with broken reflections below. The TEM results each exhibit similar conductivity-depth structure to one another with an 80 m to 150 m thick high conductivity layer existing approximately 100 m to 130 m below the surface.

#### 6.1 Seismic Reflection Results

##### 6.1.1 Comparison with Frontier Geosciences' Results

The final stacked images for SL-1 and SL-2 generated by Frontier Geosciences Inc. show some similarities to the results of this study; however several main differences are noticeable (see Figures 6.1 and 6.2). The most noticeable difference is the amount of random noise throughout the final stacked sections. Although high frequencies are included in Frontier Geosciences' results, reflections are obscured by low frequency and "chatter" noise. Using a different band-pass filter than that applied by Frontier Geosciences, much of the low frequency noise was removed, making the frequency content of the final results from this study appear higher. Similarly, any visible reflections in Frontier Geosciences' results appear ringy and largely discontinuous, whereas with the removal of the low frequency and "chatter" noise through bandpass filtering and  $f$ - $x$  deconvolution those same reflections appear significantly more continuous.

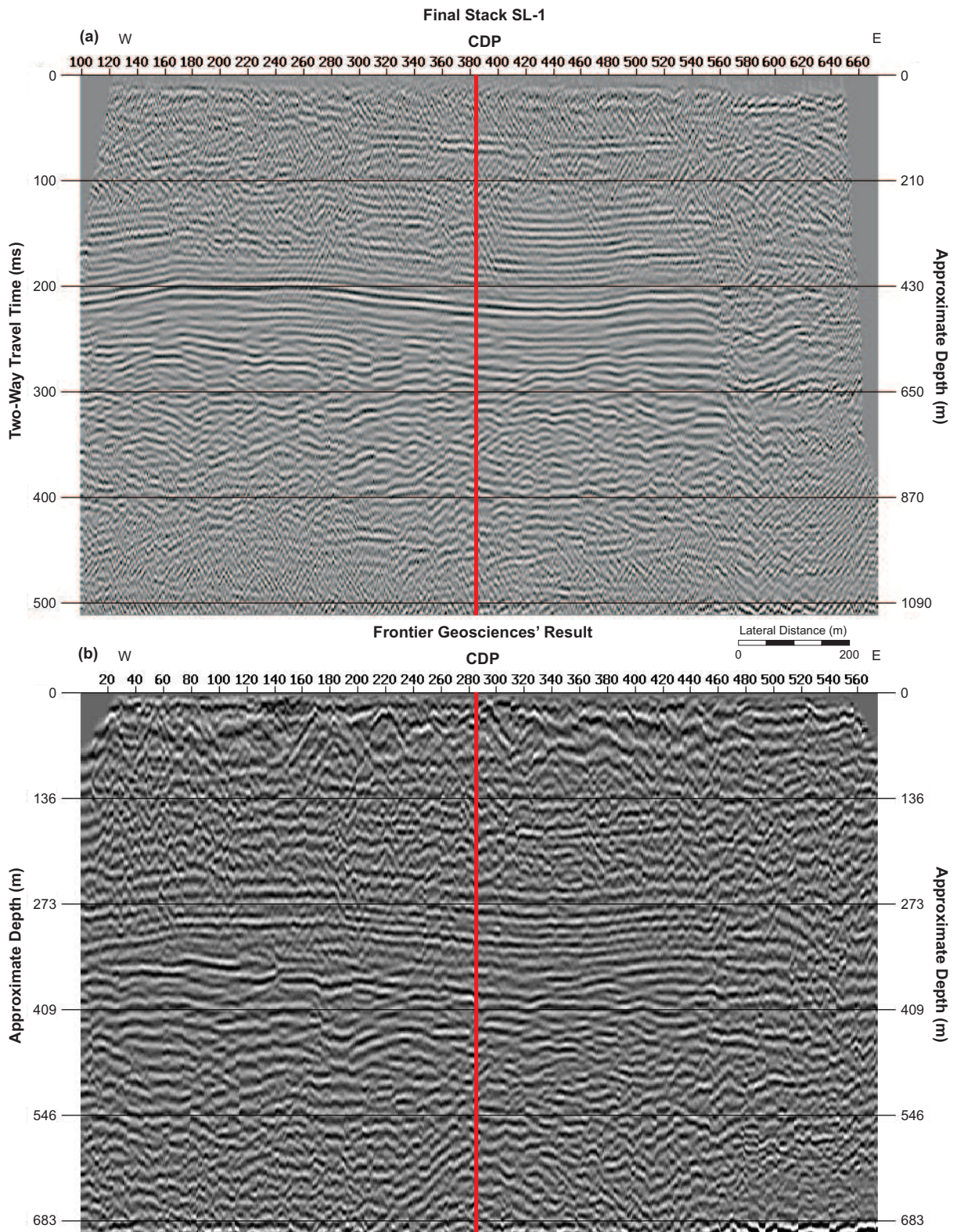


Figure 6.1: SL-1 processing results from: (a) this study, using GLOBE *Claritas*, (b) Frontier Geosciences, using WinSeis. Both seismic sections are plotted as variable density.

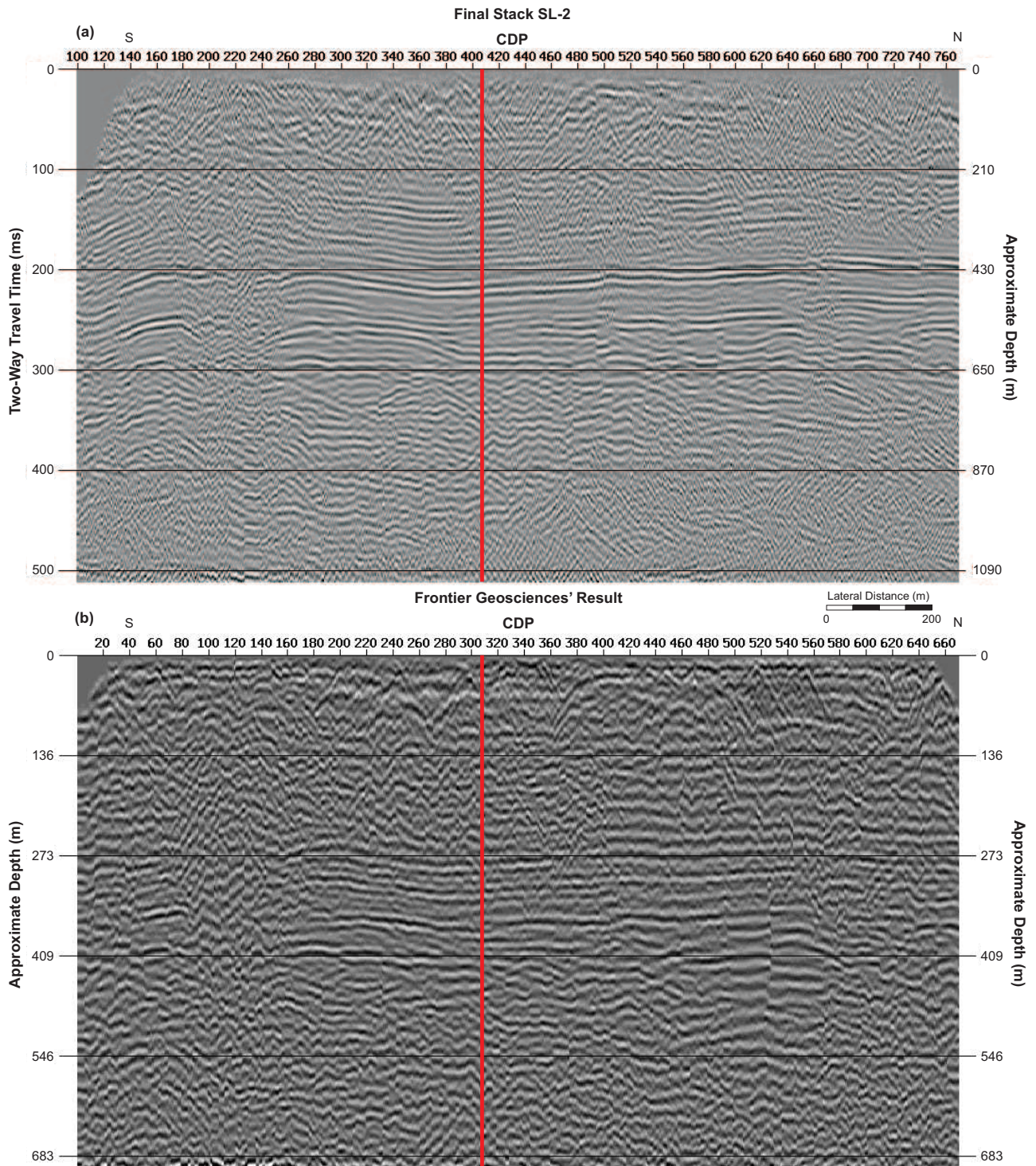


Figure 6.2: SL-2 processing results from: (a) this study, using GLOBE *Claritas*, (b) Frontier Geosciences, using WinSeis. Both seismic sections are plotted as variable density.

Refracted arrivals are commonly removed because they are a source of extraneous noise, despite the loss of information in the upper portion of the stacked section. If refracted arrivals were included during this study, the stacked section would begin just below 0 m depth; however, they also would have added extraneous information beyond 150 ms, potentially leading to an incorrect interpretation. To include only the most credible data in this project, muting the refracted arrivals resulted in the upper  $\sim 30$  m of SL-1 and SL-2 being removed.

Based on the GLI-3D refraction analysis results of this study and velocity data generated from laboratory measurements on borehole samples in the MacKenzie Delta (Ji et al., 2002), the velocity models shown in Table 6.1, which assume a constant compressional velocity,  $v_p$ , of 4400 m/s below 12-14 m, yield a maximum depth of 1114 m for both sections. This is a significant contrast to the depth-conversion conducted by Frontier Geosciences, which assumed a constant  $v_p$  of 2800 m/s, making the maximum depth  $\sim 700$  m. This depth seems unrealistic, given that the compressional velocity used (2800 m/s) disagrees with the compressional wave velocity analyses shown above both stacked sections (3000 to 4000 m/s) in Figure 2.4.

SL-1			SL-2		
Thickness (m)	Depth (m)	Velocity (m/s)	Thickness (m)	Depth (m)	Velocity (m/s)
1	1	400	1	1	400
1	2	2848	1	2	3099
5.5	7.5	3995	4.25	6.25	3877
6.5	14	4384	6	12.25	4229
1100	1114	4400	1101.75	1114	4400

Table 6.1: Depth-conversion velocity model from results of GLI-3D refraction analyses for SL-1 and SL-2.

Neither the results from this study, nor those generated by Frontier Geosciences show a clear interpretation of the easternmost  $\sim 250$  m of SL-1 or the  $\sim 170$  m-wide portion near the south end of SL-2 between CDPs 180 and 250. Also, neither set of results show strong or continuous reflections present in the lower third of the stacked sections.

Frontier Geosciences' seismic results are roughly comparable with the intermediate results of this study, in terms of processing applied. In addition to the pre-stack processing steps taken by Frontier Geosciences, this study included pre-stack spherical divergence, spectral balancing, deconvolution and  $f-k$  filtering. Residual statics and  $f-x$  deconvolution filtering for removal of incoherent noise were applied as post-stack steps in this study, but were not carried out by Frontier Geoscience. Thus the final stacked images from this study show significant improvements on those from Frontier Geosciences (Figures 6.1 and 6.2).

### 6.1.2 Seismic Interpretation

As described in Section 3.1.1, the complete processing sequence was applied to both seismic lines 1 and 2 (SL-1 and SL-2). The most noticeable event in the final stacked images from SL-1 (Figure 6.1a) and SL-2 (Figure 6.2a) is a strong, slightly undulating horizontal reflection near 200 ms, which is estimated to be at a depth of  $\sim 440$  m. Other reflections of various strength and continuity are visible throughout both images.

Interpretations of the final stacked sections for SL-1 and SL-2 are shown in Figures 6.3 and 6.4. Three reflection events (A-C) showing varying levels of reflection continuity have been highlighted with coloured lines within both sections. Two more lines (D1 and D2) represent the range within which reflections appear strongest and are the most continuous.

Reflector A (orange) is visible at  $\sim 130$  m depth between CDPs 305 and 530 (563 m) in SL-1, with a 20 CDP (50 m) gap where reflector A is inferred. This reflection is shorter in SL-2, less visible at similar depths, and between CDPs 300 and 460 (400 m). On SL-1, its termination at either end may be associated with near-surface faulting. On SL-2, the termination of reflector A may be associated with near surface faulting at its northern end. Reflector B (green) is not continuous across either section, but is observed in four places in SL-1, covering most of the

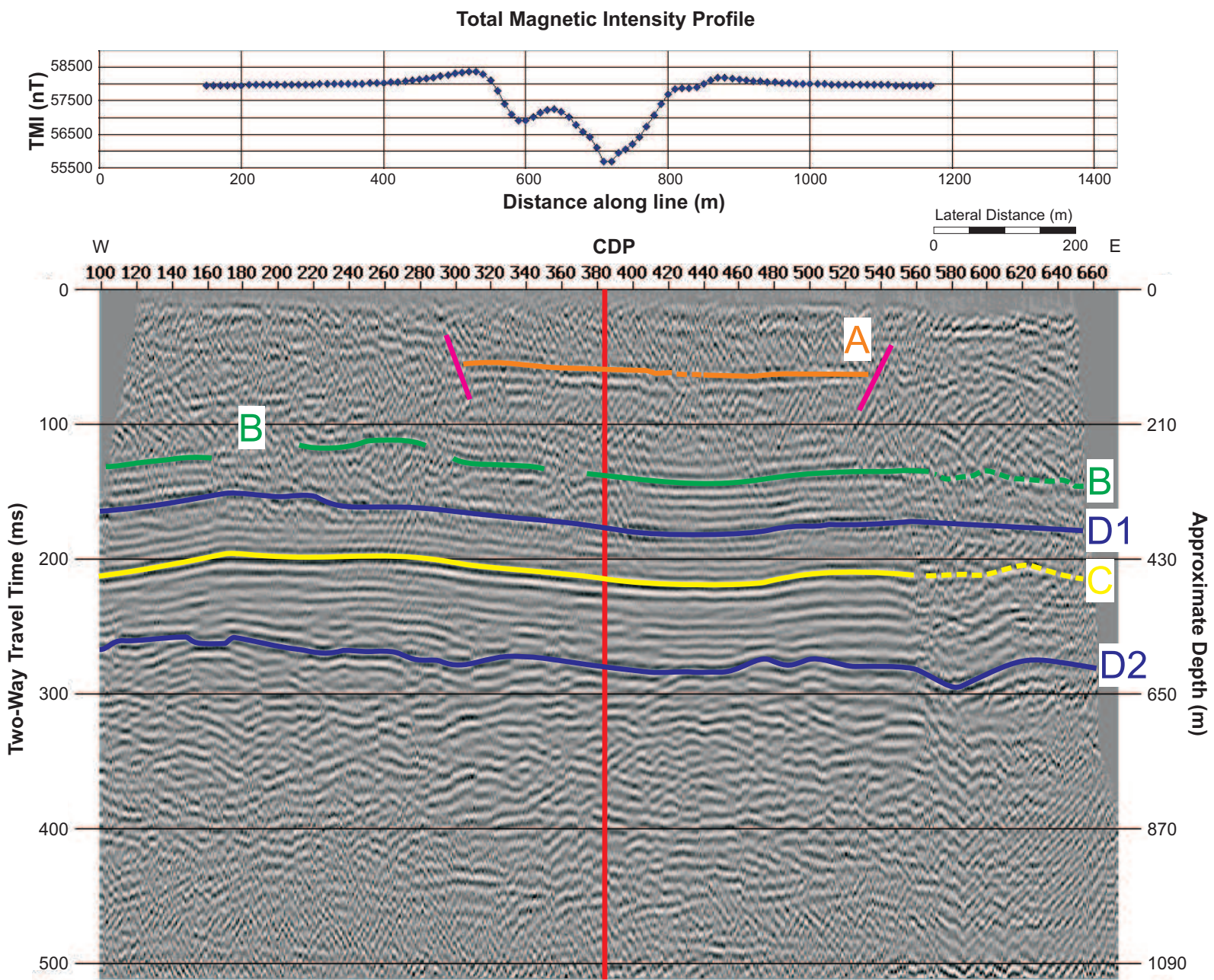


Figure 6.3: Interpretation of seismic reflection processing results from SL-1. The top plot is the total magnetic intensity profile along SL-1 (from Diamondex Resources).

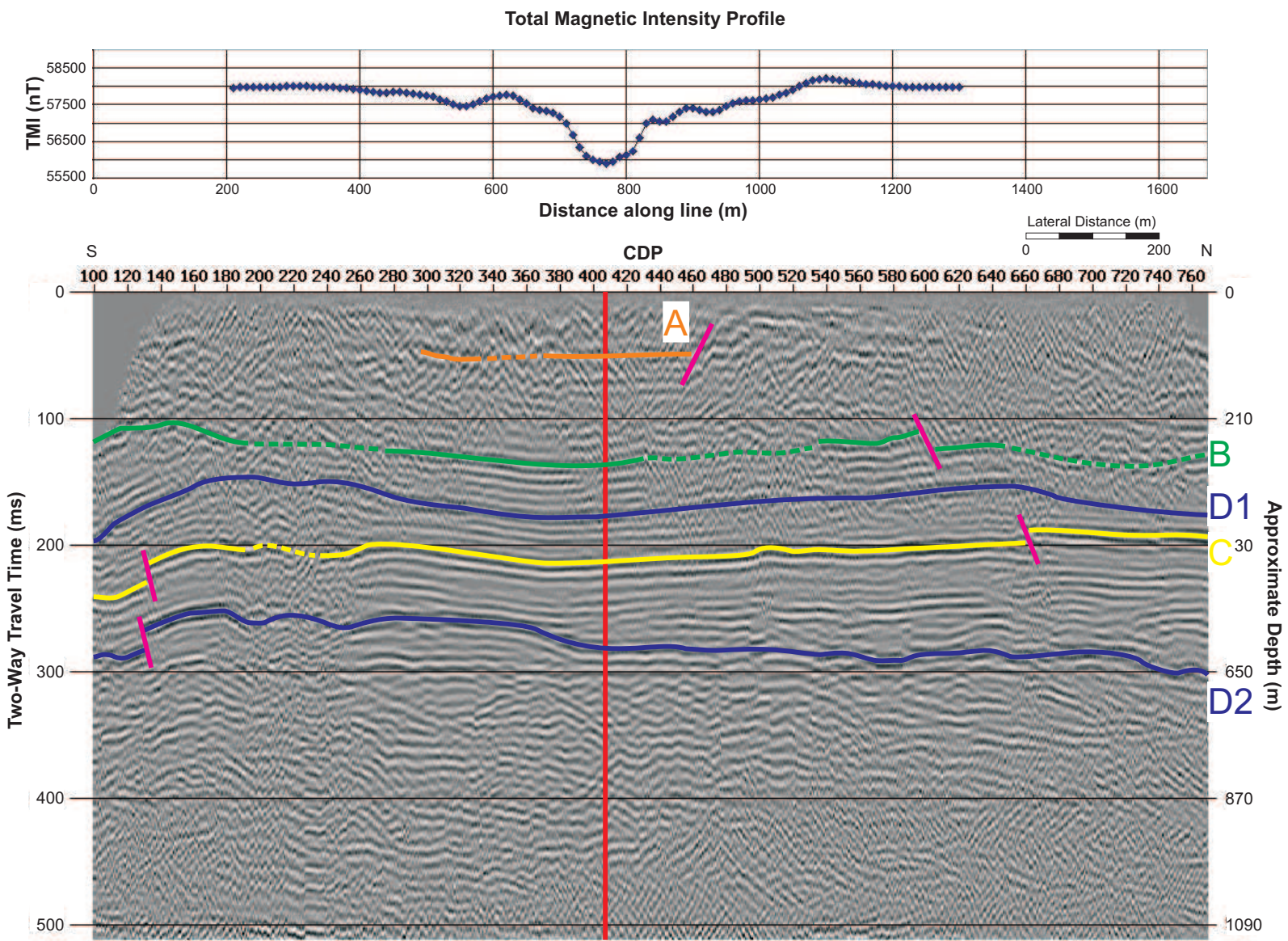


Figure 6.4: Interpretation of seismic reflection processing results from SL-2. The top plot is the total magnetic intensity profile along SL-2 (from Diamondex Resources).

section. At the eastern end of SL-1, it is inferred beyond CDP 570. In SL-2, reflector B is visible in three places, with inferred lines connecting them. At CDP 600 there is a break, where reflector B shifts down slightly, indicative of a possible fault. Reflector C (yellow) is the aforementioned prominent event easily observed in SL-1 and SL-2. This reflector undulates across the final section for SL-1 and is clearly observed between CDPs 100 to 560, beyond which it is extrapolated on the poorer quality data. On SL-2, reflector C is continuous from CDP 100 to 190, with an interpreted upward offset at CDP 130. Between CDPs 190 and 240 reflector C is inferred, beyond which the reflector undulates slightly and is continuous until CDP 770. At CDP 660, reflector C is offset upward slightly, perhaps due to a minor fault, then dips gently toward the north end of the section.

The main zone within which reflections are clearest and most continuous is defined by the upper limit, D1, and the lower limit, D2 (both blue). D1 horizons interpreted in both sections show only small variations from the profile of reflector C. At the east end of SL-1, D1 tends to dip slightly downward whereas reflector C rises slightly with a small bump around CDP 620. In SL-2, D1 is nearly parallel to reflector C from CDP 100 to 180. Between CDPs 180 and 260 the time interval between D1 and reflector C decreases, after which it remains constant until CDP 660. Beyond CDP 660, D1 dips downward toward the north, while the depth of reflector C remains about the same, shrinking the interval between the two lines. Above D1, reflections tend to exhibit a similar shape to reflector C; however, reflections above D1 are less laterally continuous than those between D1 and D2.

The lower limits in both final sections appear more rough, as reflections are less laterally continuous. D2 follows many of these short reflections as though they were one. This is more notable in SL-1, as individual reflections across the entire section appear short and somewhat discontinuous. In SL-2, D2 joins reflections that have greater lateral continuity than those in SL-1 in the southern half of the section. In the northern half of SL-2, D2 follows many short

reflections similar to those of SL-1. Between D1 and D2, lateral continuity is strong and reflections are clear; however, reflectivity below D2 appears broken, discontinuous and disorganized. One explanation for this is that D2, at a depth of  $\sim 600$  m, roughly represents the bottom of the sedimentary layers and the top of the basement rocks.

## 6.2 Transient Electromagnetic Results

### 6.2.1 Comparison with Frontier Geosciences' Results

The TEM inversion results from EM1DTM yield a similar general result to those generated by Frontier Geosciences. Although several similarities exist between the results of this study and the previous results, some new conclusions can be stated.

The main difference between the TEM results generated by Frontier Geosciences and those of this study is that the high resistivity region at the surface is thinner in the results of this study. The depth at which the resistivity decreases to  $\sim 30 \Omega\text{m}$  varies between approximately 70 m and 110 m in Frontier Geosciences' results, while the results of this study indicate a depth ranging between 30 m and 80 m. Figures 6.5 through 6.7 show total magnetic intensity (TMI) profiles, results from EM1DTM, smoothed results from EM1DTM and Frontier Geosciences' TEMIXGL results for Lines 0100N through 0300S, respectively.

Based on the colour scale used to represent the resistivity values of Frontier Geosciences' results, it is difficult to discern variations between  $0 \Omega\text{m}$  and  $30 \Omega\text{m}$ ; however, it is clear that the values are all less than  $30 \Omega\text{m}$ . The low resistivity layer visible in the results of this study (see plot (b) in Figures 6.5 through 6.7) vary between  $4 \Omega\text{m}$  and  $15 \Omega\text{m}$ , agreeing well with the range of resistivity values determined by Frontier Geosciences.

During the testing phase of this study, a model consisting of a low resistivity body beginning between 40 and 80 m and extending to depth was proven to adequately reproduce the data as well as one with a depth limited low resistivity layer (Section 5.1). From this analysis, it is clear

that neither a thickness to the low resistivity layer nor any other resistivity structure below  $\sim 150$  m can be assigned.

Frontier Geosciences' results offer a general subsurface resistivity structure that adequately reproduces the observed data. However, the results from this study indicate that, based on the observed data, one cannot reliably make conclusions about how the resistivity structure varies below  $\sim 150$  m as the results default to the reference model below this depth. Considering this limitation, the resistivity structure in the upper  $\sim 150$  m of both sets of results are similar, the only difference being the depth at which the high-to-low resistivity contrast appears.

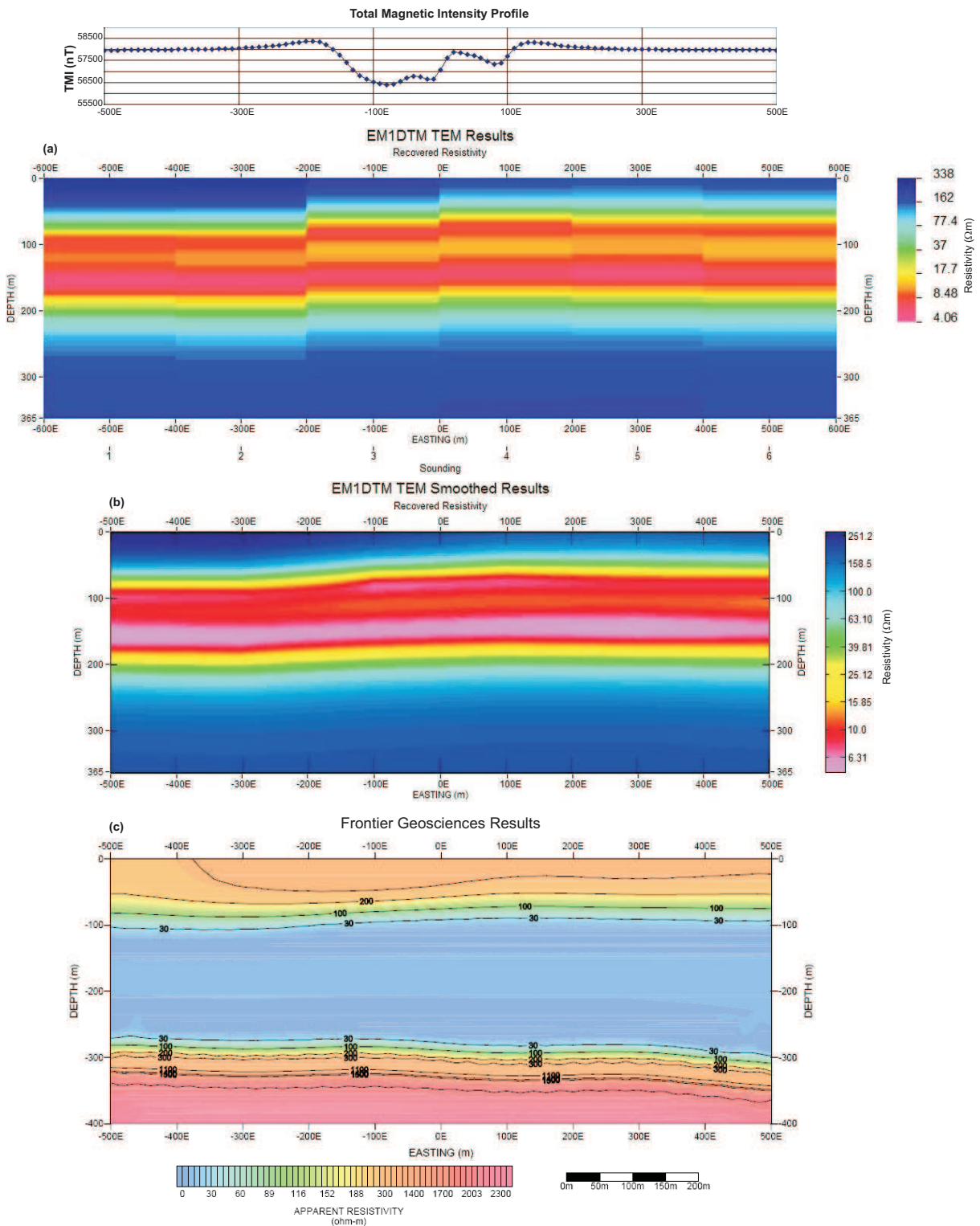


Figure 6.5: TEM Line 0100N comparison of results. (a) EM1DTM results; (b) EM1DTM smoothed results; (c) Frontier Geosciences' results from TEMIXGL (extracted from Payne and Candy, 2005). The top plot is the total magnetic intensity profile along SL-1 (from Diamondex Resources).

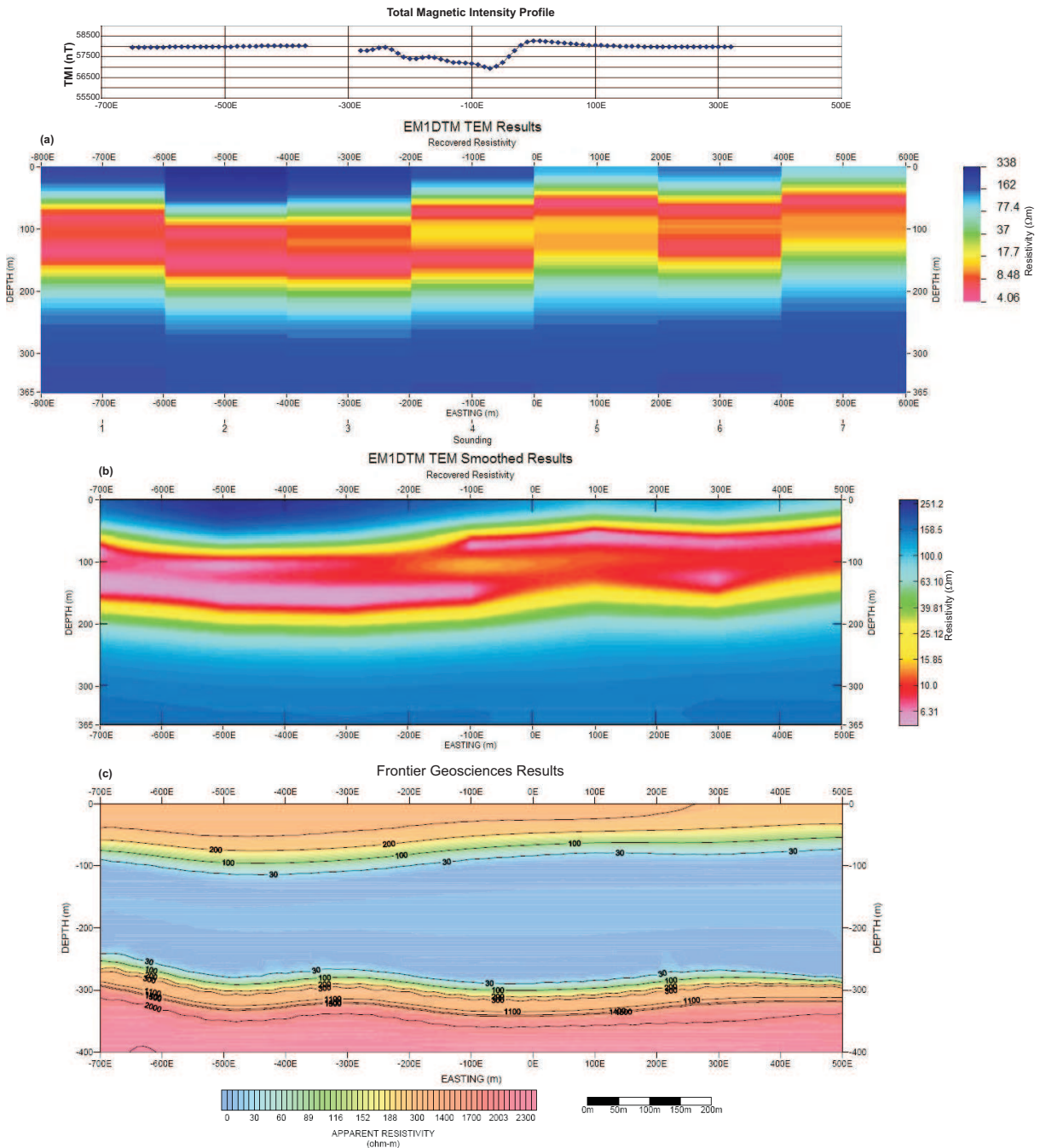


Figure 6.6: TEM Line 0100S comparison of results. (a) EM1DTM results; (b) EM1DTM smoothed results; (c) Frontier Geosciences' results from TEMIXGL (extracted from Payne and Candy, 2005). The top plot is the total magnetic intensity profile along SL-1 (from Diamondex Resources).

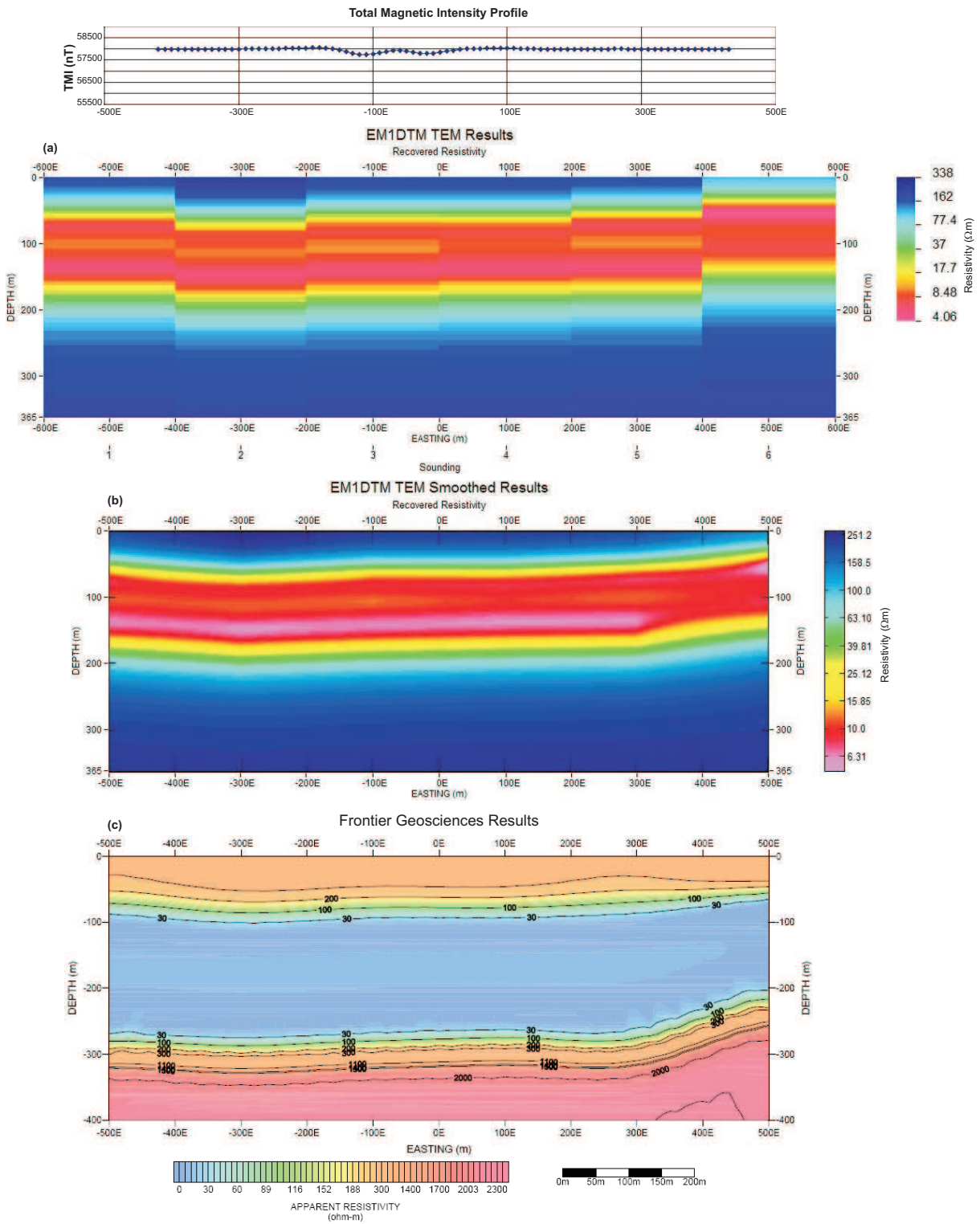


Figure 6.7: TEM Line 0300S comparison of results. (a) EM1DTM results; (b) EM1DTM smoothed results; (c) Frontier Geosciences' results from TEMIXGL (extracted from Payne and Candy, 2005). The top plot is the total magnetic intensity profile along SL-1 (from Diamond Resources).

### 6.2.2 TEM Interpretation

The results from inverting all three TEM lines indicate a similar general subsurface structure throughout Area 1915 to a depth of 365 m (Figure 6.8). The general structure consists of a high resistivity layer at the surface extending to between 30 m and 80 m, where the low resistivity layer begins. The low resistivity layer appears underlain by another layer of high resistivity extending to 365 m; however this lower interface and all resistivity structure below  $\sim 150$  m is unreliable as the inversion is not actually “seeing” beyond this depth.

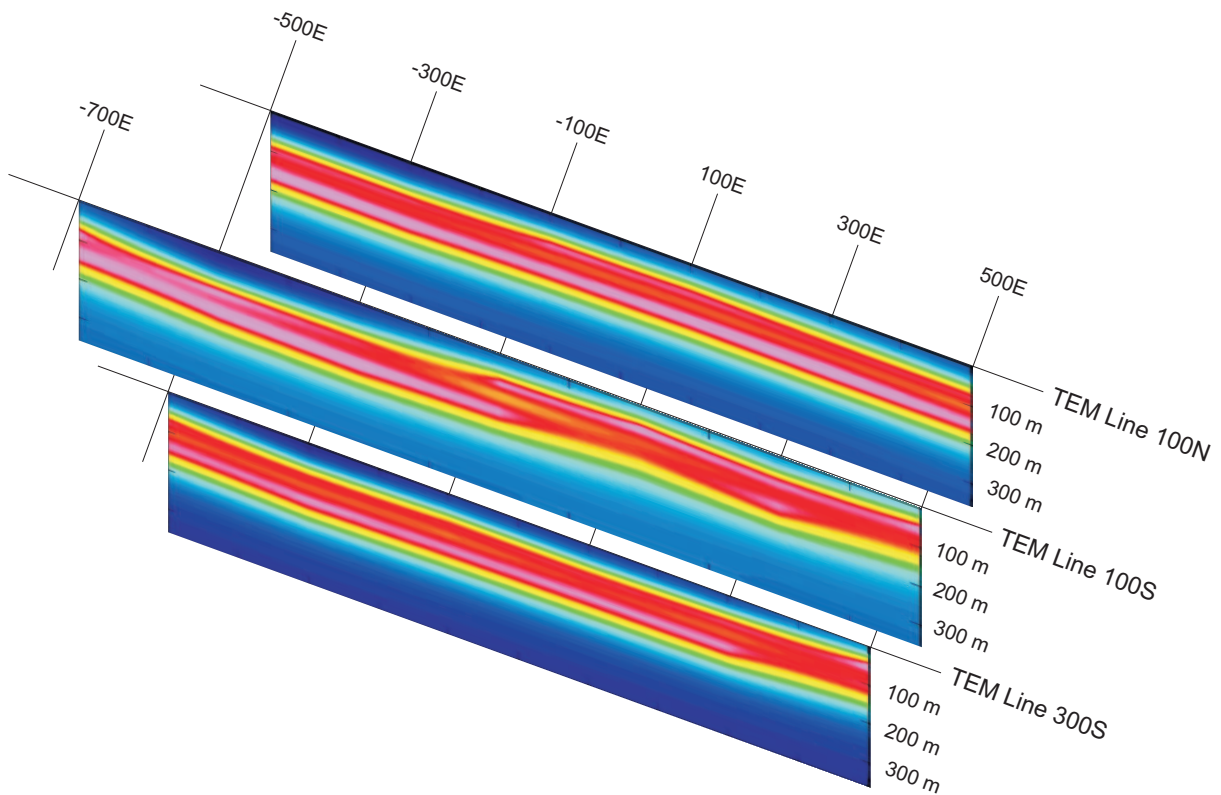


Figure 6.8: A 2.5-D plot of TEM profiles set within the Area 1915 TEM survey grid. The grid-line intersections represent the centre of a given loop.

The causes of the TMI anomalies noted for Lines 0100N, 0100S and 0300S are not reflected in the TEM results, as there is no evidence to suggest a resistivity anomaly with similar lateral

extent to that of the TMI anomaly exists below the respective TEM lines. Based on the half-width of each magnetic anomaly, the depth at which a magnetic body should be discovered is less than 200 m. The low resistivity/high conductivity layer is shallower at some points along each line; however, none of the shallower points correspond with the lateral location of the observed magnetic anomaly. Because the data were collected using 200 m loops, the EM1DTM final model only supplies six columns of data within each entire 1000 m-wide section. Thus, the lateral resolution of the TEM method for identification of the feature causing the resistivity anomaly is severely limited with the given data.

### **6.3 Interpretation**

Comparing results from different techniques is a useful method to increase confidence in or dispel a particular interpretation of geophysical data. For this type of analysis to be effective, the physical property information given by the results needs to be indicative of the same type of subsurface variation, and of the same physical survey volume. Given that the exploration goal for this property is to find kimberlitic material, both seismic reflection and TEM surveys offer insightful information. Kimberlites often exhibit a vertical pipe structure that disrupts otherwise laterally continuous layers. They usually have lower seismic impedances than the host rocks and show electrical conductivity anomalies, although the extent and even sign of these anomalies can be highly variable. These traits make kimberlites a potential target for both seismic reflection and TEM surveys.

Prior to conducting the seismic reflection and TEM surveys in the Lena West property, Diamonex Resources examined maps of TMI across the property. A strong magnetic anomaly, shown as a circular variation in the TMI, which are commonly caused by vertical kimberlite pipes, was visible in Area 1915 (see Figure 1.3). Based on the strength of the magnetic anomaly, it was expected that if a kimberlite pipe was the cause, it would be relatively near the surface

(within a few hundred metres). This information led to a TEM survey being carried out to determine electrical conductivity structure in the upper subsurface, and a seismic reflection survey being conducted to determine the base of any overlying sedimentary layers and if any otherwise continuous layers were disrupted. Finally, information from three boreholes was made available for this study, supplying direct information about the subsurface materials.

Figure 6.9 shows five vertical logs plotted together using a common depth scale. The two columns on the left are 20 CDPs (50 m) from the final stacked images of SL-2 and SL-1, both representing the intersection with the other line. Events A, B, C, D1 and D2, described in Section 6.1.2, are identified on both seismic columns. The next two columns are 50 m-wide sections about the 0E lateral distance on the smoothed pseudo-2-D conductivity depth sections from TEM Lines 0100N and 0100S, which are parallel to SL-1. These columns are 100 m in opposite directions along SL-2 from the intersection with SL-1. The rightmost column represents borehole LW04-001, which offers some insight into the subsurface material beneath Area 1915. Borehole LW04-001 is located at the intersection of SL-1 and SL-2. The simplified version of borehole LW04-001, shown in Figure 6.9 for comparison purposes, consists of  $\sim 33$  m of overburden, underlain by  $\sim 10$  m of mixed material consisting of thin, interbedded layers of limestone/dolomite, shale and mudstone, followed by  $\sim 169$  m of mudstone to 212 m.

The two columns from SL-1 and SL-2 (Figure 6.9) correspond well with one another. This is expected, given that both lines approximately represent the same subsurface. The three main reflection features and two boundaries within which reflections are most coherent and continuous, previously discussed in Section 6.1.2, are visible in the columns for SL-1 and SL-2. Reflector A is visible at  $\sim 130$  m in both columns, but only strongly so in SL-1. At  $\sim 290$  m reflector B is faintly visible in both seismic columns. Reflector C, visible across both stacked sections, is clear at a depth of  $\sim 475$  m in the two seismic columns of Figure 6.9. Between D1 and D2 there is good agreement between the two seismic columns. Although some reflections appear visible below D2 (i.e.,  $\sim 860$  m in SL-1 column), nothing below  $\sim 650$  m exhibits any lateral continuity

across the full stacked sections (Figures 6.3 and 6.4).

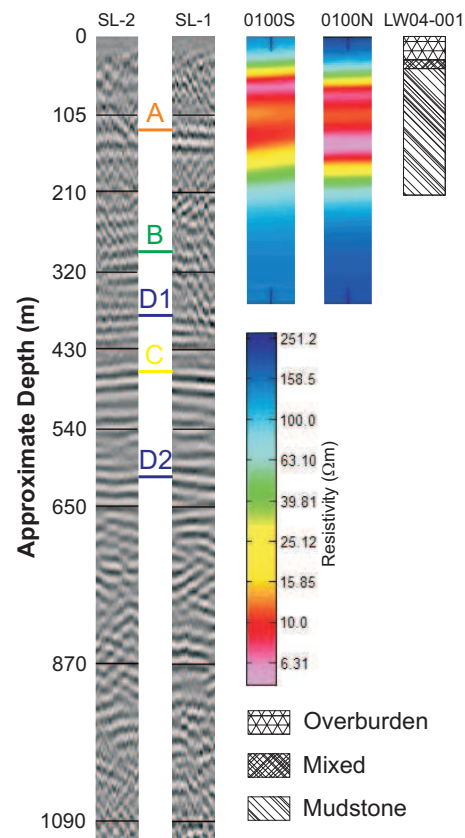


Figure 6.9: A vertical log comparison of results from SL-1, SL-2, TEM Line 0100S, TEM Line 0100N and LW04-001. SL-1 and SL-2 are both 20 CDPs (50 m) wide, while the column from TEM Line 0100S and Line 0100N also represents 50 m on either side of the intersection of SL-1 and SL-2. A simplified version of LW04-001 is presented for comparative purposes. LW04-001 is located at the intersection of SL-1 and SL-2, and represents no lateral variation.

Both TEM columns in Figure 6.9 show the high conductivity (low resistivity) layer beginning between 40 m and 50 m depth, roughly corresponding with the mixed-mudstone interface in LW04-001. The depth, or even existence, of the lower boundary of the high conductivity layer is not known because the inversion is not able to accurately determine the conductivity structure at this depth when such a highly conductive layer is present. The high conductivity layer consistently shows two more highly conductive regions within the overall layer. The

deeper of these two regions appears to correspond with reflector A in the two seismic columns; however, there is no corresponding feature present in borehole log LW04-001. Therefore, the existence of such a feature is suspect.

The contacts shown in the borehole log of Figure 6.9 seem to have little correlation with any features in the seismic columns. The only possible connection is to the high-to-low resistivity contact at  $\sim 50$  m in the TEM columns, as previously mentioned. Subsurface information below 212 m would certainly be an asset in confirming major contacts observed in the seismic columns (i.e., the undulating reflection at  $\sim 440$  m). As the TEM results are restricted by the skin depth, which depends on the resistivity of the subsurface, results below  $\sim 150$  m are not plausible for this data set.

Results from the TEM survey and inversion indicate a high conductivity layer starting between 30 m and 80 m below the surface. The upper boundary to this high conductivity layer seems to coincide with the mixed-mudstone interface in borehole LW04-001. None of the events visible in the seismic logs correspond with the borehole log or with the TEM logs; however, the borehole log was depth-limited to 212 m, while the TEM results were limited to  $\sim 150$  m. As a result, there is not much opportunity for cross-comparison between the different exploration techniques used on this site. Regardless of whether or not a layer boundary is present at  $\sim 130$  m, the borehole did not indicate the presence of any bedrock or kimberlite. Based on the strongly continuous undulating reflection visible in both final stacked seismic sections, a borehole is not likely to encounter either bedrock or kimberlitic material before reaching a depth of at least 500 m.

## **Chapter 7**

### **CONCLUSION**

This study included the processing of two seismic reflection lines and the inversion of three transient electromagnetic (TEM) lines within Area 1915 of the Lac des Bois property, owned by Diamondex Resources Ltd. The main technical objective was to process the seismic data and invert the TEM data to improve upon the previous processing and inversion results, yielding a more comprehensive interpretation of the subsurface. Scientifically, the objectives were to compare the new processing and inversion results with the previous results to detect complementary or contradictory information, and to test the robustness of the EM1DTM inversion algorithm when applied to real data.

#### **7.1 Conclusions**

##### **7.1.1 Seismic Reflection**

Kimberlite pipes are typically vertical in nature, and tend to disrupt otherwise continuous horizontal layers. When a surface total magnetic intensity (TMI) survey is conducted above a kimberlite pipe, the expected result is a near-circular magnetic anomaly. The two seismic lines in Area 1915 of the Lena West property intersect above the centre of the observed magnetic anomaly.

This study found that both seismic sections illustrate strong horizontal reflectivity across their entirety between depths of 300 m and 600 m. Except where poor data exist, a strong undulating reflection is visible across both seismic sections at ~440 m. Any reflections below ~600

m (D2 on Figures 6.3 and 6.4) appear discontinuous or rough, possibly indicating that event D2 is the base of the overlying sediments. Several reflections visible in the results of this study are visible within the results generated by Frontier Geosciences; however, the reflections in the results of this study appear significantly stronger. This correlation of results increases confidence in the previous conclusion that the sedimentary layers have not been laterally disturbed. The overall structure within the final stacked sections is similar to Frontier Geosciences' results, but the depths at which reflections occur are interpreted to be quite different, with those of this study being interpreted as significantly deeper. The results from this study have achieved a notable improvement over those generated by Frontier Geosciences, mostly due to the removal of more extraneous noise. However, no clear lateral disruption in either seismic section correlates with the TMI anomaly.

### **7.1.2 Transient Electromagnetic**

Three TEM lines were surveyed in Area 1915 to determine the subsurface conductivity structure below the TMI anomaly. If a kimberlite pipe were to exist below the magnetic anomaly, it would likely exhibit a different conductivity structure than the surrounding material.

The general structure of the TEM results from this study consists of a low conductivity layer in the upper 30 m to 80 m, underlain by a high conductivity layer of undeterminable thickness. The main differences between the results of this study and those generated by Frontier Geosciences include: the high conductivity layer being interpreted as shallower in all three TEM lines, and proof that neither the thickness of the high conductivity layer nor reliable values of resistivity below  $\sim 150$  m can be determined. Given the 200 m loop spacing used, the lateral resolution of this survey is limited such that a 200 m-wide anomaly may only influence one sounding. However, no strong lateral variations that correspond with the TMI anomaly are visible in any

of the TEM sections. The upper boundary of the high conductivity layer corresponds with reflector A in both seismic sections (Figure 6.9). No reflections clearly correspond with the TEM results.

The inversion results generated using EM1DTM both adequately reproduce the observed data and match the general conductivity structure of Frontier Geosciences' results, generated using TEMIXGL. EM1DTM was not able to consistently invert data collected both inside and outside the transmitter loop together to the same level of data misfit as observed when inverting only the data collected inside the transmitter loop. However, this is likely due to the data representing a 3-D subsurface and the algorithm trying to invert the data for a 1-D model.

## 7.2 Future Work

From a scientific viewpoint, the collection of as much relevant data as possible is preferred. However, this is not an economically practical ideology, and exploration companies must compromise between acquiring the necessary data and keeping costs down. The recommendations given here are presented as though cost is not a concern because scientifically Area 1915 would be a good testing site for future work.

Further geophysical exploration of this area would include a more dense 1-D TEM survey, or alternatively, a 3-D TEM survey. Adding far-offset seismic reflection shots along SL-1 and SL-2 would allow for a more comprehensive refraction analysis, and hence more velocity information.

Apart from geophysics, several boreholes drilled to  $\sim 1000$  m would offer a true glimpse into the subsurface by offering direct material-at-depth information. Also, samples from the boreholes could be tested to determine material properties such as density, porosity, bulk modulus, shear modulus, permeability, magnetic susceptibility and electrical conductivity. Finally,

conducting borehole geophysical surveys would offer maximum information regarding the sub-surface. These data could then be used as *a priori* information in further analyses of the seismic and TEM data.

## References

- Atkinson, E., and Pryde, R., 2006, Seismic investigation of selected kimberlite pipes in the Buffalo Head Hills kimberlite field, north-central Alberta, Alberta Energy and Utilities Board, EUB/AGS Special Report 079, 1 p.
- Farquharson, C., 2005, Manual for Program EM1DTM, version 1.0, Unpublished manual available from the Geophysical Inversion Facility of the Department of Earth and Ocean Sciences, University of British Columbia.
- Farquharson, C., 2006, Background for Program EM1DTM, version 1.0, Unpublished manual available from the Geophysical Inversion Facility of the Department of Earth and Ocean Sciences, University of British Columbia.
- Hajnal, Z., Lewry, J., White, D., Ashton, K., Clowes, R., Stauffer, M., Györfi, I., and Takacs, E., 2005, The Sask craton and Hearne province margin: Seismic reflection studies in the western Trans-Hudson orogen: *Canadian Journal of Earth Sciences*, **42**, 403–419.
- Hammer, P. T. C., Clowes, R. M., and Ramachandran, K., 2004a, High-resolution seismic reflection imaging of a thin, diamondiferous kimberlite dyke: *Geophysics*, **69**, 1143–1154.
- Hammer, P. T. C., Clowes, R. M., and Ramachandran, K. 2004b, Seismic reflection imaging of thin, kimberlite dykes and sills; exploration and deposit characterization of the Snap Lake dyke: *Lithos*, **76**, 359–367.
- Ji, S., Wang, Q., and Xia, B., 2002, Handbook of seismic properties of minerals, rocks and ores: École Polytechnique de Montréal, Montréal, Canada.

- LeCheminant, A. N., and Kjarsgaard, B. A., 1996, Part 1: Geology, petrology, and geotectonic controls - introduction: Searching for Diamonds in Canada, **Open File 3228**, 5–9.
- McLean, R. C., and Clarke, D. B., 2005, A report on the 2004 geophysical surveys, diamond drilling, auger sampling and fluvial sampling on the Lena West property, Private report prepared for Diamondex Resources Ltd., 21 p plus appendices.
- Payne, K., and Candy, C., 2005, Report on a seismic reflection and transient electromagnetic investigation, Lena West project, Lac des Bois, NT, Contractor report prepared for Diamondex Resources Ltd., 11 p plus 26 figs.
- Pell, J. A., 1997, Kimberlites in the Slave craton, Northwest Territories, Canada: *Geoscience Canada*, **24**, 77–90.
- Yilmaz, O., 1987, *Seismic data processing*: Society of Exploration Geophysicists, Tulsa, OK.

## Appendix A

### A Sample Input File

The main file that controls the EM1DTM inversion is the `em1dtm.in` input file. In the example below, each parameter has a general description to the right. For those descriptions which appear cryptic, a further description is given here. Line seven defines the parameters for the Huber and Eklblom measures. The eighth line defines the relative importance of the terms corresponding to the “smallest” and “flattest” components of the model norm (discussed in Section 3.2.1). Line 9 defines the type of inversion; “1” represents a user-supplied cooling schedule for the regularization ( $\beta$ ), the parameters for which are defined on line 10. A complete description for an `em1dtm.in` file can be found in Farquharson (2005).

The following is the `em1dtm.in` file from Area 1915 Line 0100N:

```
1915_0100N          ! 1.  root name
1915_0100N.obs      ! 2.  observations file
start.layers        ! 3.  starting conductivity model
5.00E-03            ! 4.  reference conductivity model (small)
5.00E-03            ! 5.  reference conductivity model (flat)
NONE                ! 6.  weights
1000 2 0.0001 2 0.0001 ! 7.  hc, eps,ees, epz,eez
0.001 1             ! 8.  0.001 - acs, 1 - acz
1                   ! 9.  inversion type
50 50 0             ! 10. final beta, starting beta, factor
20                  ! 11. max # of iterations
0.0001              ! 12. convergence test
DEFAULT             ! 13. Hankel kernel evaluations
DEFAULT             ! 14. Fourier kernel evaluations
2                   ! 15. amount of output
```

## Appendix B

### A Sample Starting Model

The starting model is defined in a start.layers file, which begins with a single numerical value indicating the number of layers within the starting model. Subsequent lines contain each layer's thickness and starting conductivity value, beginning at the surface. The thickness of the final layer is set to zero because it represents an infinite half-space, but a non-zero conductivity value is supplied for the half-space.

The following is an abbreviated version of the start.layers file used to represent a 200  $\Omega\text{m}$  half-space starting model for this study:

```
85
  0.1000    0.0050
  0.2000    0.0050
  0.3000    0.0050
  0.4000    0.0050
  0.5000    0.0050
  0.6000    0.0050
  0.7000    0.0050
  0.8000    0.0050
  0.9000    0.0050
  1.0000    0.0050
  1.1000    0.0050
  ...      ...
  7.7000    0.0050
  7.8000    0.0050
  7.9000    0.0050
  8.0000    0.0050
  8.1000    0.0050
  8.2000    0.0050
  8.3000    0.0050
  8.4000    0.0050
    0        0.0050
```

## Appendix C

### A Sample Observation File

Data for each TEM line are entered into a specific format within an observation (\*.obs) file. The first three values of the first line define the centre of the transmitter loop in local coordinates (x, y, z), while any remaining values are notes for the user. The first value on the second line indicates the number of vertices of the transmitter loop, and each subsequent pair of numbers represents the distance of each vertex relative to the centre of the transmitter loop (as x- and y-distances in m). The final value on the second line is the transmitter loop elevation. Line 3 contains the name of the transmitter current waveform file (tcw). Line four specifies the number of receivers and a flag defining the units of the measurement times for the specific sounding. The first value on line 5 is the dipole moment of the receiver for the specific sounding; in EM1DTM, the dipole moment acts as a scaling factor. The two values following the dipole moment are the receiver x- and y- centre coordinates relative to the transmitter loop centre, respectively, and the third is the absolute elevation, with 0 being at the ground surface. The fifth entry on line 5 indicates the receiver orientation, while the sixth entry is the number of measurement times for that sounding, and the final value represents the units of observation for that receiver. Each subsequent line consists of the following: a time, the sweep number, the observed data, a flag for the form of uncertainty and the amount of uncertainty (in this case, values representing 10% of the data to a minimum error of 1.0E-03). The data for the next receiver is then given, starting with the line containing the dipole moment. Once the data for all relevant receivers have been entered, the next sounding begins starting with the transmitter loop centre location. A complete description of the syntax and parameter flag definitions for an observation file is

given in Farquharson (2005).

The following is an example taken from the 1915\_0100N\_all.obs file. Note that the general layout is illustrated with much of the data removed.

```
-500.00 100.00 0.00 notes
4 -100.00 -100.00 -100.00 100.00 100.00 100.00 100.00 -100.00 0.0000
tcw.txt
3 2
1.0000 0.0000 0.0000 0.0000 z 20 1
 0.88100E-01 1 2.9188 v 0.29188
 0.10690 1 2.4129 v 0.24129
 0.13130 1 1.9514 v 0.19514
 0.16190 1 1.5578 v 0.15578
...
 3.3730 1 0.15460E-01 v 0.15460E-02
 4.2970 1 0.92455E-02 v 0.10000E-02
 5.4750 1 0.52634E-02 v 0.10000E-02
 6.9780 1 0.28209E-02 v 0.10000E-02
1.0000 200.00 0.0000 0.0000 z 20 1
 0.88100E-01 1 -0.98363E-01 v 0.98363E-02
 0.10690 1 -0.45600E-01 v 0.45600E-02
 0.13130 1 -0.23841E-02 v 0.10000E-02
 0.16190 1 0.24502E-01 v 0.24502E-02
...
 3.3730 1 0.96628E-02 v 0.10000E-02
 4.2970 1 0.63803E-02 v 0.10000E-02
 5.4750 1 0.39508E-02 v 0.10000E-02
 6.9780 1 0.22645E-02 v 0.10000E-02
-1.0000 200.00 0.0000 0.0000 x 20 1
 0.88100E-01 1 0.80234 v 0.80234E-01
 0.10690 1 0.69415 v 0.69415E-01
 0.13130 1 0.58560 v 0.58560E-01
 0.16190 1 0.48406 v 0.48406E-01
...
 3.3730 1 0.66388E-02 v 0.10000E-02
 4.2970 1 0.37735E-02 v 0.10000E-02
 5.4750 1 0.19174E-02 v 0.10000E-02
 6.9780 1 0.94671E-03 v 0.10000E-02
-300.00 100.00 0.00
4 -100.00 -100.00 -100.00 100.00 100.00 100.00 100.00 -100.00 0.0000
tcw.txt
3 2
1.0000 0.0000 0.0000 0.0000 z 20 1
 0.88100E-01 1 2.9723 v 0.29723
 0.10690 1 2.4702 v 0.24702
 0.13130 1 1.9975 v 0.19975
 0.16190 1 1.5949 v 0.15949
...
```